HCCI Modeling and Control Strategies Utilizing Water Injection

by

David Carl Gordon

A thesis submitted in partial fulfillment of the requirements for the degree of

Master of Science

Department of Mechanical Engineering
University of Alberta

Abstract

Homogeneous Charge Compression Ignition (HCCI) has the potential to significantly reduce oxides of nitrogen (NO_x) emissions, while maintaining a high fuel efficiency compared to existing lean-burn spark ignition engines. HCCI is characterized by compression induced autoignition of a lean homogeneous air-fuel mixture. The challenge with HCCI combustion is the high cyclic variation due to the lack of direct ignition control leading to cycles with high emissions. Combustion timing is highly dependent on the in-cylinder state including pressure, temperature and trapped mass. To control HCCI combustion it is necessary to have an accurate representation of the gas exchange process. Currently, microprocessor based engine control units require that the gas exchange process is simplified to meet very limited calculation time allowances. However, using a Field Programmable Gate Array (FPGA) a detailed simulation of the physical gas exchange process can be implemented in real-time. This thesis outlines the process of converting physical governing equations to an online real-time capable FPGA based model. This development process is described and the online model is experimentally validated using a single cylinder research engine with electromagnetic valves. The real-time FPGA gas exchange results are recorded and compared to the offline reference. The FPGA model is able to accurately calculate the cylinder temperature, air mass, fuel mass and heat released at 0.1° crank angle (CA) intervals during the gas exchange process for a range of negative valve overlap, boost pressures and engine speed making the model useful for real-time control applications. An operating region variation is performed on the engine to determine the effect of the negative valve overlap on the HCCI combustion process. The impact of direct water injection on HCCI is also investigated by varying water injection timing and quantity. Using the results of the water injection testing, a feed-forward direct water injection controller is developed and experimentally validated. The low latency

and rapid calculation rate of the FPGA is utilized to calculate the gas exchange process and the required control interaction within 0.1°CA. The maximum cylinder pressure during negative valve overlap, heat released during combustion and residual fuel mass are the three control inputs which are tested with the feedforward controller. This controller prevents early rapid combustion following a late combustion cycle by using direct water injection to cool the cylinder charge and counter the additional thermal energy from any residual fuel that is transferred between cycles. By cooling the trapped cylinder mass the upcoming combustion phasing can be delayed to the desired setpoint. The controller was tested at several operating points and showed an improvement in the combustion stability as shown by a reduction in the standard deviation of both combustion phasing and indicated mean effective pressure.

Preface

All results presented in this thesis are original work by David Gordon. The research for this thesis was performed as part of an international collaboration with Dr.-Ing. Stefan Pischinger from RWTH Aachen University. Some sections of this thesis have been published or are in the review process for publication. Specifically, Chapter 4 has been published as:

1. D. Gordon, C. Wouters, M. Wick, F. Xia, B. Lehrheuer, J. Andert, C. R. Koch, and S. Pischinger, "Development and experimental validation of a real-time capable FPGA based gas-exchange model for negative valve overlap," International Journal of Engine Research, 2018.

I have presented sections of the work presented in Chapter 6 which has been presented at the international Symposium for Combustion Control (SCC) in Aachen, Germany.

1. D. Gordon, C. Wouters, M. Wick, B. Lehrheuer, J. Andert, C. R. Koch, and S. Pischinger, "Development and experimental validation of an FPGA based in-cycle control strategy for HCCI combustion stability," Proceedings of the Symposium for Combustion Control, 2018.

Additionally, the work presented in Chapter 6 has been split into two manuscripts which are currently submitted for review:

1. M. Wick, D. Gordon, J. Bedei, C. Wouters, E. Nuss, B. Lehrheuer, J. Andert, and C. R. Koch, "In-cycle control for stabilization of HCCI using direct water injection," Applied Energy, Submitted October 1, 2018 (Submission ID: APEN-D-18-09617).
2. D. Gordon, C. Wouters, M. Wick, B. Lehrheuer, J. Andert, C. R. Koch, and S. Pischinger, "Development and experimental validation of an FPGA based in-cycle control strategy for HCCI combustion stability," International Journal of Engine Research, Submitted October 31, 2018 (Submission ID: IJER-18-0240).

Acknowledgements

First and foremost, I would like to express my sincere gratitude to my supervisor Dr. Charles Robert (Bob) Koch for his support and constructive feedback during the completion of my M.Sc. Not only is his academic support greatly appreciated but so are all the opportunities he has presented to me. His exceptional mentorship has allowed me to grow both professionally and personally.

Similarly, I would like to thank Dipl.Ing. Bastian Lehrheuer and Dr.Ing. Jakob Andert for allowing me to perform the research for my thesis at RWTH Aachen. Their academic knowledge and experimental experience were very much appreciated, as was their support and friendship outside the lab.

I would also like to acknowledge my fellow colleagues in my research group at the University of Alberta (Khashayar, Masoud, Robert, Giffin, and Brad) your support and encouragement are greatly appreciated. Also to my colleagues at VKA in Aachen (Frederik, Maximilian, Julian, and Raphael) your friendship and support made my time in Germany very enjoyable. I would also like to provide a special thank you to Christian Wouters for not only spending long nights in the engine lab with me and helping to solve what seemed like never-ending problems with my model but for also acting as my translator, tour guide, and friend. All of my colleagues provided both academic support and a needed distraction from my work when I needed a break.

Finally, I would like to thank my parents (Laurie and Kathy) and sister (Danielle) for their continued support and encouragement. Without their love and support I would not have been able to complete my graduate studies.

Table of Contents

List of Tables

List of Figures

Nomenclature

Acronyms

ACU	Angle Calculation Unit
AFR	Air Fuel Ratio
ASCI	Application Specific Integrated Circuit
ATAC	Active Thermo-Atmosphere Combustion
aTDC	after Top Dead Center
BDC	Bottom Dead Center
bTDC	Before Top Dead Center
CA	Crank Angle
CA_{10-90}	Burn duration for 10 - 90% fuel mass
CA10	Crank Angle of 10% mass burned
CA50	Crank Angle of 50% mass burned
CA90	Crank Angle of 90% mass burned
CAD	Crank Angle Degree
CAS	Combustion Analysis System
CI	Compression Ignition
CO	Carbon Monoxide
CO_2	Carbon Dioxide
CPI	Calculated Pressure Indication
Cyl	Cylinder

DOI	Duration of Injection
ECU	Engine Control Unit
EGR	Exhaust Gas Recirculation
EMVT	Electro-Magnetic Valve Train
EOC	End of Combustion
EVC	Exhaust Valve Closing
EVO	Exhaust Valve Opening
FEV	FEV Europe GmbH
FPGA	Field Programmable Gate Array
GE	Gas Exchange
HC	unburnt HydroCarbons
HCCI	Homogeneous Charge Compression Ignition
ILC	Iterative Learning Controller
IMEP	Indicated Mean Effective Pressure
IVC	Intake Valve Closing
IVO	Intake Valve Opening
LHV	Low Heating Value
LHV	Lower Heating Value
LUT	Lookup Table
MABX	dSPACE MicroAutoBox II
MPC	Model Predictive Control
NO_x	Oxides of Nitrogen
NVO	Negative Valve Overlap
O_2	Oxygen

PC	Personal Computer
RAM	Random Access Memory
RON	Research Octane Number
RPM	Revolutions Per Minute
SI	Spark Ignition
SOC	Start of Combustion
SOI	Start of Injection
TDC	Top Dead Center
TDM	Time Division Multiplexing
VKA	nstitute for Combustion Engines
VVT	Variable Valve Timing
XSG	Xilinx System Generator

Symbols

α	Convective heat transfer coefficent
Δ	Change in
κ	Ratio of specific heats
λ	Air–fuel Equivalence Ratio
ρ	Density
σ_X	Standard deviation of X
φ	Crank Angle
A	Area
c_p	Specific heat at constant pressure
c_v	Specific heat at constant volume
dX	Change in X
h	Enthalpy
L	Length
m	Mass
p	Pressure
Q	Thermal energy
R	Ideal gas constant
r_{fr}	Fresh air ratio
T	Temperature
u	Internal energy
V	Volume
V_d	Displaced volume
v_{pis}	Piston speed
x_{ex}	Exhaust gas fraction
z^{-n}	Delay of n units

Subscripts

270	Injection timing at 270 ° CA
580	Injection timing at 580 ° CA
a	Air
b	Burnt
con	Connecting rod
crk	Crankshaft
cyl	Cylinder
eff	Effective
$evap$	Evaporation
EVC	Exhaust Valve Closing
EVO	Exhaust Valve Opening
ex	Exhaust
f	Fuel
g	Gas
h_2O	Water
inj	Injector
IVC	Intake Valve Closing
IVO	Intake Valve Opening
l	Liquid
$main$	Main combustion period
mix	Mixture
NVO	Negative valve overlap period
$stoic$	Stoichiometric
th	Throttle
w	Wall

Chapter 1

Introduction

1.1 Motivation

With governments around the world introducing evermore stringent environmental legislation, automobile manufactures have turned to new combustion methods in an attempt to meet these targets. Currently, the G-20 countries account for 90 % of the global vehicle sales and 17 of these countries follow the European emissions legislation which has recently been updated to Euro 6 in 2015 [1]. The Euro 6 environmental legislation sets to introduce tighter regulations in regards to nitrogen oxide (NO_X) emissions which have been reduced from 0.18 to 0.08 g/km over the previous Euro 5 regulations [2]. These new regulations are challenging to meet using current engines and require expensive exhaust gas aftertreatment systems such as selective catalytic reduction, lean NO_X traps and others [1, 3]. Meeting these tough emissions targets using exhaust aftertreatment systems have negative fuel efficiency implications which seems to have led companies to use specialized engine code to only meet these regulations under emission testing conditions but not while under normal operating conditions [4].

Over the last few decades automotive manufactures have been researching new low temperature methods to improve the engine out emission levels while also improving

engine fuel efficiency [5]. Homogeneous Charge Compression Ignition (HCCI) is a combustion method which utilizes a premixed homogeneous charge of fuel and air which is auto-ignited from the rising temperature and pressure during compression [6]. HCCI has shown promising engine out emissions reductions, however, the lack of a direct timing control is a major control and modeling challenge [7]. The speed of the combustion process also restricts the type of control strategies which can be tested due to time constraints of current microprocessors.

1.2 Problem Statement

The objective of the research presented in this thesis is to improve the stability of HCCI combustion through the use of direct water injection control based on a real-time model of the current in-cylinder state.

1.3 Thesis Organization

This thesis is organized into the following chapters:

Chapter 2 contains the relevant background information needed throughout this work. This chapter explores the advantages and disadvantages of HCCI along with an overview and uses of FPGAs. Previous control strategies for HCCI are also presented in this chapter.

Chapter 3 provides information on the experimental engine used for this work along with all relevant data collection systems and sensors.

Chapter 4 describes the process of creating an FPGA based real-time model of the gas exchange process for an HCCI engine along with experimental validation of this model.

Chapter 5 explores the operating range and limits of the experimental test engine operating in HCCI mode. This chapter also investigates the impact of direct water

injection on steady state and cyclic operation.

Chapter 6 examines the development and experimental results of various direct water injection controllers and there ability to improve the stability of HCCI combustion.

Chapter 7 summarizes and draws conclusions from the results found in this thesis and concludes with a discussion on the possible future work.

1.4 Contributions

The major contributions of this work are:

- Development and experimental validation of a real-time capable FGPA based gas exchange model.
- Characterization of the impact of steady state and cyclic water injection on HCCI combustion.
- Development and experimental testing of three feed-forward water injection controllers leading to the selection of a residual fuel mass based controller for the improvement of HCCI combustion stability.

Chapter 2

Background

2.1 Homogeneous Charge Compression Ignition

Homogeneous Charge Compression Ignition (HCCI) was first introduced in 1979 under the name Active Thermo-Atmosphere Combustion (ATAC) [8]. This combustion method has an emission reduction potential which is desired due to new more stringent environmental regulations. HCCI is a combustion method that combines characteristics of Spark Ignition (SI) and Compression Ignition (CI) engines. Similar to SI engines, the air and fuel mixture is homogeneous at the the point of ignition. However, instead of utilizing an electrical spark to initiate combustion, an HCCI engine relies on the compression of the fuel and air mixture to increase the cylinder temperature and pressure above the auto-ignition point of the fuel. As the mixture is homogeneous, the combustion process begins at many points in the combustion chamber leading to a heat release that is much faster than both SI and CI engines [9]. This rapid heat release and the high compression ratios used allow for combustion that is closer to the ideal Otto cycle and therefore offer thermodynamic efficiency benefits [10]. As HCCI combustion offers many advantages including engine out emission reductions, fuel flexibility, and a thermal efficiency increase, there are also drawbacks including ignition timing challenges, increased unburnt hydrocarbon and

carbon monoxide emissions, as well as a limited operating range [6].

2.1.1 Combustion Metrics

There are various combustion metrics that are useful in describing the combustion process. These metrics will be used throughout this thesis and will be defined in this section.

The indicated mean effective pressure (IMEP) is used to describe the average pressure in the combustion cylinder during a cycle and is used to describe the load output of the engine. The variation in the IMEP, σ_{IMEP}, is used to describe the stability of the combustion where a low variation in IMEP is a smooth running engine that is producing the same power output every cycle. The IMEP of an engine can be calculated using [11]:

$$imep = \frac{work\ output\ per\ cylinder\ per\ mechanical\ cycle}{swept\ volume\ per\ cylinder} = \frac{1}{V_d}\int p_{cyl}dV \qquad (2.1)$$

Where V_d is the swept cylinder volume and dV is the change is cylinder volume. The indicated work can be calculated using the enclosed area of a pressure vs volume (p-V) trace, which can easily be calculated from the measured cylinder pressure and engine position. IMEP is independent of the number of cylinders or cylinder volume making it a good comparison between different engines, however, it does not consider the frictional losses of the engine. Then by defining the limits of integration around both the main and NVO combustion the IMEP of each combustion can be determined using:

$$imep_{main} = \frac{1}{V_d}\int_{IVC}^{EVO} p_{cyl}dV \qquad (2.2)$$

$$imep_{NVO} = \frac{1}{V_d} \int_{EVC}^{IVO} p_{cyl} dV \tag{2.3}$$

The pressure rise rate, $dp/d\varphi$, of an engine gives a description of how quickly the cylinder pressure is changing. At high pressure rise rates engine damage can occur and prolonged operation can lead to engine failure [12]. The pressure rise rate continually changes throughout the combustion event, however, its maximum value is used to represent the worst condition for that cycle and is given by:

$$dp/d\varphi = max \left| \frac{P_{cyl}(i)}{P_{cyl}(i-1)} \right| \tag{2.4}$$

Where $P_{cyl}(i)$ and $P_{cyl}(i-1)$ are the current and previous cylinder pressure, respectively.

The air-to-fuel ratio (AFR) is an important combustion metric that is used describe the mass of air, m_a, that is brought into the cylinder in relation to the mass of injected fuel, m_f, and is given by:

$$AFR = \frac{m_a}{m_f} \tag{2.5}$$

For a given fuel chemistry it is possible to calculate the exact amount of fuel required for a given amount of air for complete combustion, this is called the stoichiometric AFR. By relating the current AFR, AFR_{actual}, to the stoichiometric AFR, AFR_{stoic}, we can define the equivalence air-fuel ratio, ϕ and lambda, λ, which is given by:

$$\lambda = \frac{1}{\phi} = \frac{AFR_{actual}}{AFR_{stoic}} \tag{2.6}$$

Where a value of lambda less than 1 which is rich operation where there is excess fuel for the amount of oxygen. Or a value of lambda greater than 1 is lean engine

operation where more oxygen is present for the given fuel amount. This lean operation is where HCCI engines are operated.

To describe the timing and length of combustion the crank angle for 50% fuel mass burnt, CA_{50}, and the burn duration, CA_{10-90}, is used. CA_{50} is defined as the crank angle of 50% fuel burned or 50% of the heat released as shown in Figure 2.1. It is useful in describing the timing of the combustion process and it is often used as a controlled variable as often a specific CA_{50} is desired for maximum power and efficiency. Similar to IMEP, the variation in CA_{50} is useful in describing the cyclic variability of the combustion process. Not only is the the combustion timing important but the length of the combustion event is also valuable and is given by the burn duration. For this work it is defined as the time in crank angle degrees for the combustion to consume between 10% and 90% fuel mass, CA_{10-90} as depicted in Figure 2.1.

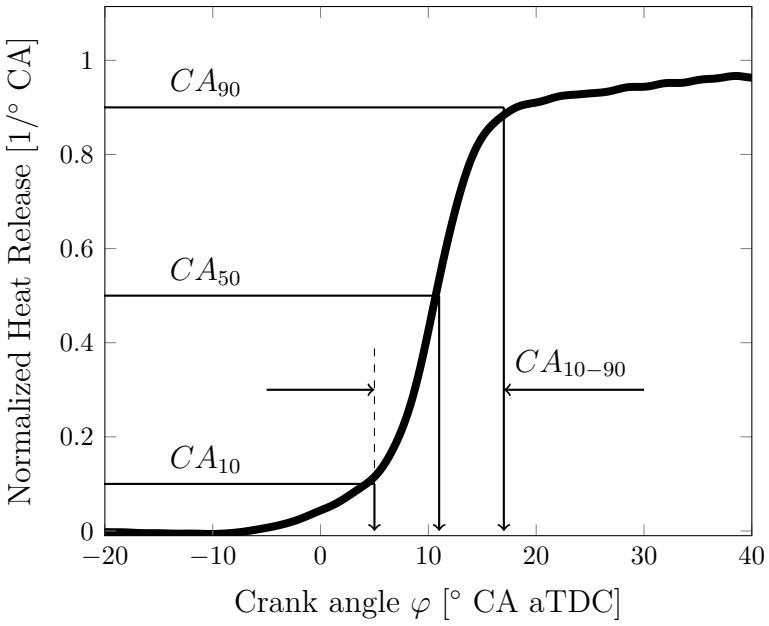

Figure 2.1: Normalized heat release showing CA_{10-90} and CA_{50}.

2.1.2 Exhaust Gas Recirculation

To provide enough thermal energy for the HCCI auto-ignition process it is often necessary to retain some exhaust gas to increase the temperature of the trapped air. This can be accomplished either through external or internal exhaust gas recirculation (EGR). External EGR involves roughing the exhaust from the exhaust manifold back into the intake manifold this causes the exhaust gas to cool before it is brought back into the combustion chamber. There is also no ability to change the amount of EGR on a cyclic basis when using an external EGR system.

Internal EGR is when the exhaust gas remains in the combustion chamber or only leaves the cylinder briefly into one of the manifolds before being brought back into the combustion chamber. Intake port and exhaust port EGR is when the exhaust is pushed into the intake / exhaust port and then drawn back into the cylinder. This method allows changes in EGR on a cyclic basis, however, it requires that one of the valves remains open as the piston passes top dead center (TDC). To accommodate this valve strategy it is necessary to have deep valve pockets in the piston to prevent a collision with the valves, this limits the piston shape to designs which provide inefficient in-cylinder mixing. This type of internal EGR also leads to increased thermal losses to the valves and manifolds. There is also increased pumping losses as the air must be pushed out of the cylinder and drawn back in past the valves which act as a flow restriction.

Combustion chamber recirculation is where the exhaust valve closes before the piston reaches TDC and the intake valve opens late (after gas exchange TDC) called negative valve overlap (NVO). This keeps the exhaust gas in the cylinder leading to reduced pumping losses compared to the other EGR strategies. To keep the cylinder pressure constant the valve timings are varied symmetrically around TDC. By increasing the NVO duration the amount of exhaust gas that is trapped in the cylinder

is increased as shown in Figure 2.2.

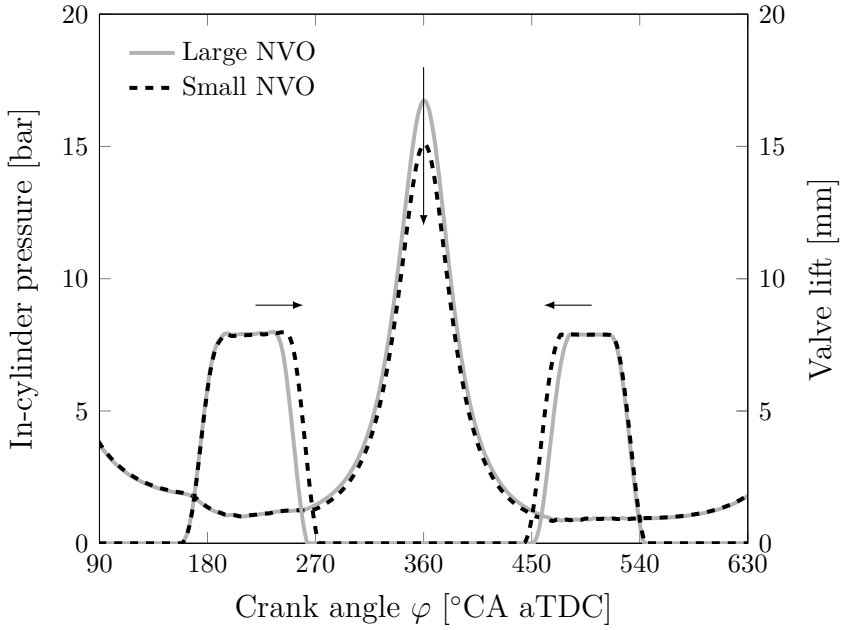

Figure 2.2: Effect of varying NVO duration on cylinder pressure.

2.1.3 Combustion Stability

Unlike SI or CI engines where combustion is controlled directly through an electrical spark or fuel injection HCCI relies on the conditions in the cylinder and chemical kinetics of the fuel to dictate when combustion begins. Therefore, there is no direct method to control combustion timing which leads to a limited operating range. At low loads misfire limits HCCI operation and high pressure rise rates and peak cylinder pressures restrict high loads [9, 13].

The lack of direct ignition control also leads to large cyclic variations leading to poor combustion stability [14]. Experimentally measured cyclic pressure signals of three consecutive cycles are shown in Figure 2.3. Here cycle 1 is a good representation of a standard cycle with a normal combustion phasing of 12° crank angle (CA) after top dead center (aTDC), it is then followed by cycle 2 which can be considered a partial misfire with a very late combustion phasing. Then, due to the incomplete

combustion residual fuel is transferred to the next cycle through internal EGR. As the combustion phasing is very late, the in-cylinder temperature increases which increases the temperature of the exhaust gas transferred to cycle 3. There is also the possibility that during the negative valve overlap (NVO) recompression a portion of the residual fuel ignites (as seen in cycle 3) and leads to a further temperature increase of the residual exhaust gas. The result is an increase in the temperature of the fresh air charge and the temperature after compression. This leads to an early combustion phasing with a high pressure rise rate. These results are consistent with other researchers [15][16, 17].

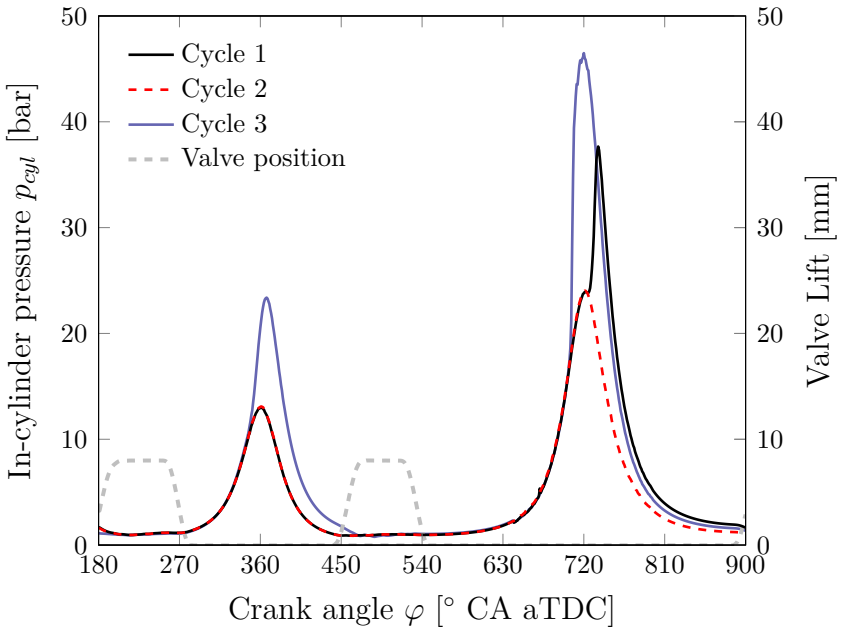

Figure 2.3: Distinct cyclic variation in the in-cylinder pressure p_{cyl} trace at $n = 1500$ 1/min, IMEP = 4.0 bar.

Figure 2.4 shows the return map for the combustion phasing, CA_{50}. A return map is used to show the relationship between the combustion phasing of the current cycle, $CA_{50}(i)$, and of the following one, $CA_{50}(i+1)$. When the two consecutive cycles are not correlated, the return map shows a stocastic scatter of data points around the center of the return map. The spread of the data points can be used to represent the

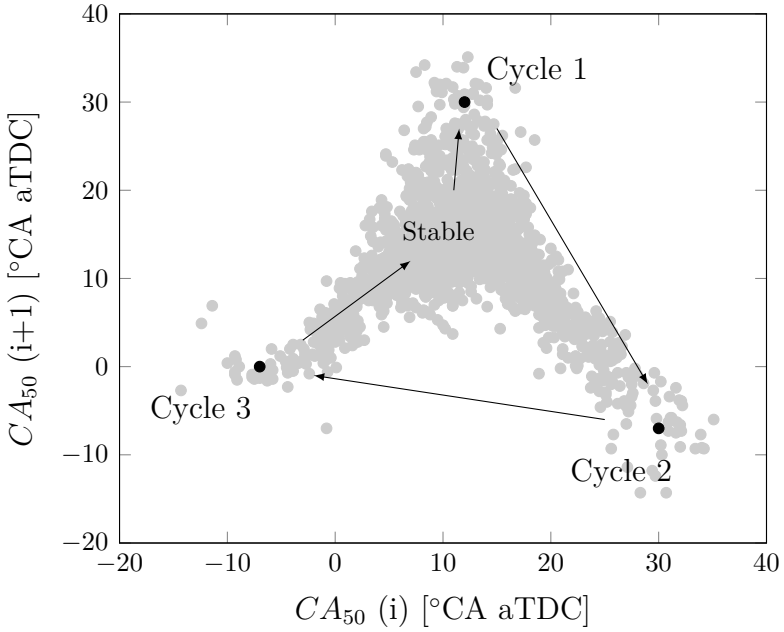

Figure 2.4: Distinct cyclic variation in combustion phasing CA_{50} return map at $n =$ 1500 1/min, IMEP = 4.0 bar.

stochastic variation from cycle to cycle [18]. When a distinct pattern or branching can be seen on the return map as is the case in Figure 2.4, a direct coupling between cycles exists [19]. To effectively stabilize combustion the spread of the data points and distinct 'V' should be reduced. Return maps are often used in application where a short prediction horizon is desired as it only provides correlation information to the next cycle.

The cyclic variation between individual HCCI cycles can also easily be seen from the normalized heat release arte as shown in Figure 2.5. Very early and fast cycles (similar to cycle 3 in Figure 2.3) can be seen on the left side of the figure while very slow long burning cycles (similar to cycle 2 in Figure 2.3) can be seen on the right. This cyclic variation is highly undesired as an early combustion phasing results in high pressure rise rates leading to increased combustion noise and possible engine damage [20, 21]. Overall, high cyclic variation of combustion also tends to reduce thermal efficiency and increase exhaust emissions [22]. Specifically, the cycles with

a very late combustion phasing (partial combustion) lead to an increase in HC and CO emissions due to the unburnt fuel and low combustion temperatures. The very early and rapid combustion cycles have increased combustion temperatures leading to increase NOx emissions from these cycles. Therefore, the combustion stability of an HCCI engine has a significant impact on its emission levels.

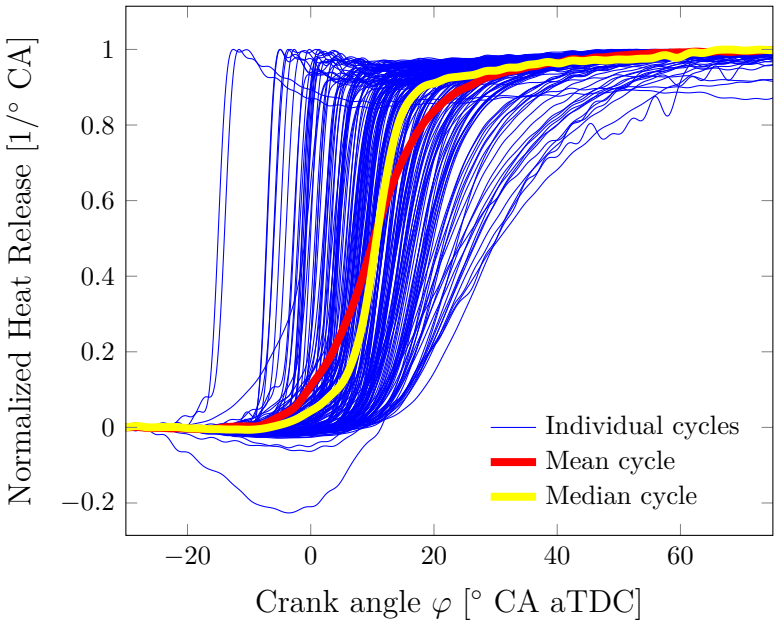

Figure 2.5: Large variability in heat release during HCCI combustion.

2.1.4 Control Strategies and Operating Range

To stabilize HCCI combustion various control strategies have been experimentally tested with varying success. Table 2.1 shows several control actuators that have been developed and tested for HCCI combustion. Each method has its advantages and disadvantages.

Intake air heating has been successful for achiving HCCI combustion but the response time of the heater makes it unsuitable for cycle by cycle control [9]. External exhaust gas recircultaion (EGR) is generally too slow to change the cylinder conditions on a cycle-by-cycle basis and introduces another source of thermal energy loss,

Table 2.1: HCCI Control Actuators (adapted from [23])

Control Variable	Actuator
Intake temperature	Electric heating
	Exhaust gas heat exchanger
Exhaust gas recirculation	External EGR
	Variable valve timing
	Exhaust rebreathing
	Exhaust throttling
Compression ratio	Mechanical variable compression ratio
Mixture composition	Dual fuel
	Pilot injection
	NVO recompression injection
Temperature	Water injection
Spark assist	Spark plug

however, it can be used in combination with other control strategies [24, 25]. Internal EGR in the form of NVO through Variable Valve Timing (VVT) is a promising control method for both cycle-by-cycle and in-cycle control methods [26–28]. The useage of VVT also offers reduced throttling losses as power output can be regulated by diluting the incoming air charge with high EGR rates [27]. Variable compression ratio systems have shown they have the ability to change the compression ratio of the cylinder on a cycle-by-cycle basis [29]. Using two fuels with different ignition properties has shown potential for HCCI operation, however, this method requires two fuel sources and two separate injection systems [30–32]. Various fuel injection strategies have shown increased combustion timing control as well as reduced emissions [33]. Water injection had been shown to decrease the pressure rise rate and delay combustion by reducing cylinder temperature, however, like the dual fuel approach two injection systems are required and often large amounts of water are used [34]. Spark assist is the utilization of an electrical spark to begin combustion which helps to increase the cylinder temperature and pressure to auto-ignite the remaining fuel air mixture. This control strategy has shown useful is extending the upper operating

limit of HCCI but at the cost of increased NO_x emissions [25].

2.1.5 Emissions

HCCI offers engine out emission benefits compared to SI and CI combustion engines. The rapid combustion or short burn duration of HCCI helps keeps the cylinder temperature low during the combustion process which helps to avoid the NO_x formation temperature [11]. As HCCI combustion is a lean homogeneous combustion there are no fuel rich areas which greatly reduces the production of soot emissions. Figure 2.6 shows how HCCI combustion avoids the NO_x and soot production regions common to SI and CI (diesel) engines. However, this lean low temperature combustion increases the amount of unburned hydrocarbon (HC) and carbon monoxide (CO) emissions, especially at low engine loads [35]. The increased HC are due to the low combustion temperature and flame extinction at the cold cylinder walls [23]. The oxidation of CO to CO_2 is a slow process and the reaction rate decreases with lower temperatures, which are found in HCCI combustion [23]. Both of these emissions, however, can be easily handled by an oxidation catalyst [11, 35].

2.1.6 Fuel Flexibility and Biofuels

HCCI combustion allows for the use of any fuel that can be vaporized in air and auto-ignited using the cylinder compression. This opens the possibility to use non-standard fuels instead of gasoline or diesel fuel. Therefore, various standard biofuels including methanol and ethanol [31, 36] along with some newer biofuels including rapeseed methyl ester [37], isopentanol [38], dimethyl carbonate [39], butanol isomers [40] and others can be effectively burned in an HCCI engine. There is also the possibilty to burn fuels containing water such as wet-ethanol, which is ethanol that has not been completely distilled to save processing energy [41].

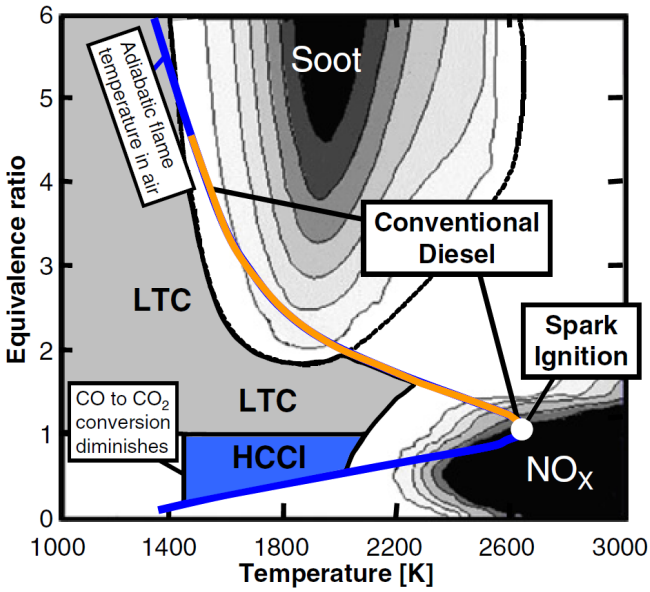

Figure 2.6: NO_x and soot production regions [35].

2.2 Field Programmable Gate Arrays

Calculations can be performed by general purpose processors or by specialized hardware. General purpose processors use software to run programs while programs can also be directly implemented on hardware using specialized hardware. Each system has its own benefits and drawbacks. The standard general purpose processor is common in a personal computer (PC). This system has a microprocessor that can handle a variety of tasks simply by changing the software. This allows for video and image processing, text editing, floating-point calculations and various other tasks to be run on the same processor. These tasks are run in serial, meaning the current task must finish before the next begins [42]. As processor speeds are continually increasing, the power, cost and heat generation of these components also increase [42].

Application Specific Integrated Circuit (ASCI) are the other computing option that utilize hardware for all calculations. They are able to perform parallel calculations and are highly optimized for a specific task allowing for orders of magnitude reduction in calculation time [43]. ASCI's are therefore highly valuable for time criti-

cal sensitive tasks as they can not be interrupted by other tasks that are trying to run [43]. As they are highly specific, ASCI's also have excellent silicon area efficiency, and reduced power consumption when compared to microprocessors [44]. The downside to ASCI's are that they are designed for a specific calculation and can only complete that calculation. They also take years to develop and have very high design cost [44]. Due to their fast calculation time and power savings they are often desired for projects, however, the cost of production and the lack computational flexibility mean that ASCI's are only practical for use in high volume production runs.

Field Programmable Gate Arrays (FPGA) are devices that combine the benefits of hardware and software computing. They are reconfigurable ASCI's which allow for calculations to be performed on hardware connections but can be reprogrammed for other tasks [45]. This removes the large time and monetary cost associated with ASCI design and allows for the computational time and energy benefits of hardware calculations. FPGA's can be reprogrammed numerous times for either small updates to the existing calculation or for an entirely new calculation. Even though FPGA's are several orders of magnitude faster and more power efficient than microprocessors they are still 5 to 25 times slower than custom built ASCI's with respect to processing speed [44].

Figure 2.7 shows a simplified overview of the internal structure of an FPGA board containing gate arrays which are interconnected with a general routing fabric. The gate arrays include various logic blocks that can be used for simple combination logic in the form of truth tables or lookup tables (LUT) or the logic blocks may also be flip-flops which allow for sequential logic [44]. Also included on the FPGA board are random access memory blocks distributed between the logic blocks that provide a efficient method for data storage.

All of these blocks are connected with a general routing fabric that contains switch points or routing blocks between the gate arrays. These connections deter-

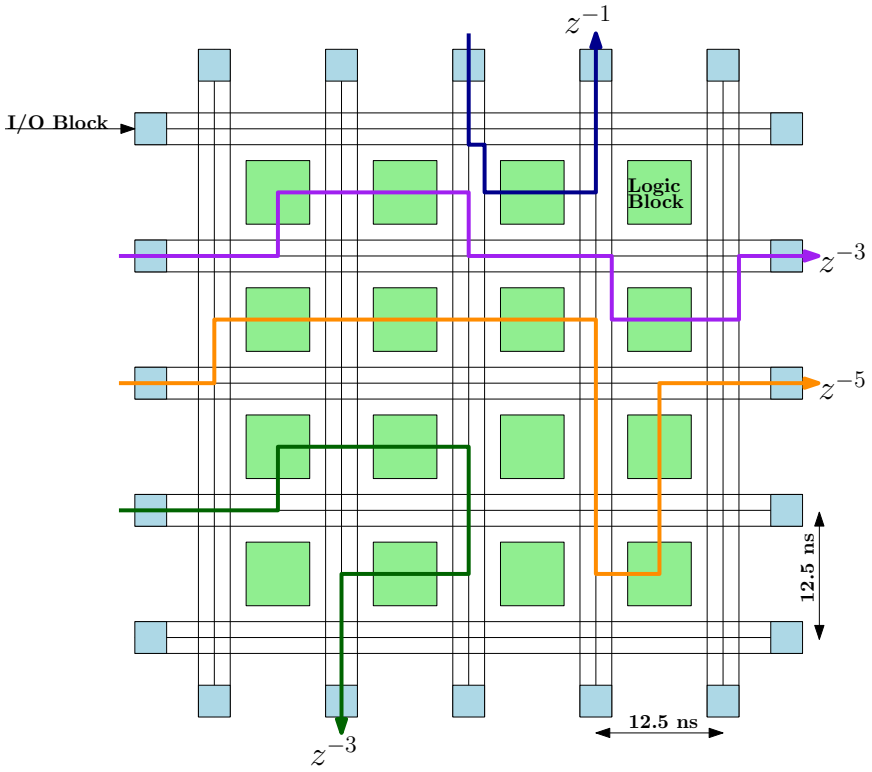

Figure 2.7: Systematic overview of Field Programmable Gate Array internal structure.

mine which routing paths are connected to the logic blocks or are passed on to the next switch block. These switch points can utilize static random access memory (SRAM), erasable programmable read-only memory (EPROM), electrically erasable programmable read-only memory (EEPROM), Fuse, Anti-fuse, and Flash technologies to determine if the switch is to be connected or disconnected [46]. The most common technology used for storing the switch configuration is static RAM or SRAM, which is a volatile memory that is fast and easy to reconfigure. To program the switch points a single bit of data is needed for each switch and is stored in a bit-stream file that contains all of the switch positions for a specific FPGA configuration. Therefore, reprogramming the FPGA is as simple as generating a new bit-stream file which connects the logic blocks in a new configuration.

A major difference between FPGA's and microprocessors is the ability to perform

many parallel calculations on an FPGA. Often microprocessors have a higher clock speed than FPGA's, however, are limited to sequential calculations. When various calculations can be run together the parallel computation ability allows for faster calculations on an FPGA. Figure 2.7 shows various colored lines connecting various logic blocks via the routing fabric. Each of these lines is a simplified example showing 5 possible calculation paths. The figure shows that all 5 of these calculations can take place simultaneously.

One challenge with using an FPGA is the individual delays caused by each FPGA logic block. Each logic block takes a fixed amount of time for the calculation to take place. Most calculations take multiple calculation steps and thus multiple logic blocks are connected. This leads to an accumulated delay equal to the number of logic blocks connected times the base sample rate. This can be seen in Figure 2.7 as the z^{-n} where n is the total delay. However, as FPGA's support parallel calculations and these calculations can take differing amounts of time the signals can become desynchronized. In order for the calculation to be time synchronized the total delay of the calculation path must be accounted for.

2.3 Real-time Engine Control

This section will provide an overview of previous research regarding real-time engine control. As discussed in the previous section both microprocessor and FPGA's can be used for engine control calculations and this section will highlight the current uses of each.

2.3.1 Processor Implementation

Various HCCI control strategies have been implemented on traditional microprocessor based engine control units (ECU) [47]. These controllers are generally cycle-by-cycle

controllers which consider the previous cycle for control interaction in the subsequent cycle. Using a prediction of the upcoming combustion phasing the cyclic variation present in HCCI can be reduced. These controllers are often used to track load and speed changes within the HCCI operating range and have been successfully used for this purpose [28].

Various control strategy have been implemented and simulated and experimentally tested which include feedforward and feedback control [48], model predictive controllers (MPC)[49–51], model based controllers [52], and iterative learning controllers (ILC) [31]. All of these control strategies provide controllability of the HCCI process and each have there own advantages and disadvantages.

Currently, important characteristics of the in-cylinder state such as the residual gas fraction require at at least three seconds to be calculated using microprocessor based controllers [53]. Furthermore, the calculation can be simplified using black box modeling and a large data approach with an autoregresive process for the various HCCI combustion parameters which can be estimated [54]. For example, the calculation of residual gas fraction can also use look-up tables, which must be created in advance, for real-time controller implementation [55].

All of these control strategy utilize traditional microprocessor based ECU's which are readily available and in use in current vehicles. However, these restrict the calculation speed down to where cycle-to-cycle HCCI control is the norm. To reduce cyclic fluctuation the implementation of in-cycle control strategies is desired which requires shorter calculations times.

2.3.2 FPGA Implementation

Using the low latency and parallel computing advantages of FPGA hardware has increased their use in demanding real-time control applications where calculation time is limited. In [56], FPGA hardware is used to provide closed loop control for the posi-

tion of pneumatic valves. The control is successfully implemented and experimentally tested showing that the valve control is stable and able to provide a variety of valve strategies.

For internal combustion engine control, FPGA hardware has shown advantageous in the calculation of heat release in real time (calculation time of less than 0.02 CAD at 1200 rpm) which can be then used for HCCI combustion control [45]. They have also been used for a wide range of cylinder pressure based calculations including wall heat losses and IMEP among others [57].

In [58], an FPGA controller is used to control the amount of injected fuel to prevent an overshoot of IMEP resulting from unburnt fuel transfered from the previous cycle. The author suggests that a real-time calculation of exhaust gas fraction would improve the accuracy of the residual fuel mass calculaiton and allow for a better prediction of the fuel transferred from one cycle to the next. In [59], an FPGA is used to calculate the real-time combustion metrics, CA50 and IMEP, which are then used for closed-loop control. The real-time calculated values were compared to offline post-processing results and showed acceptable results.

2.3.3 In-Cycle Control Timing Constraint

When considering all the various HCCI control strategies that are possible, it is important to consider the calculation time that is available for possible control strategies. Often the majority of engine control is performed cycle-by-cycle and not within a single cycle as used for in-cycle control. Figure 2.8 shows some possible in-cycle control interactions that can be used to control HCCI combustion as described in Section 2.1.4. By taking the in-cylinder state at Exhaust Valve Closing (EVC) and an engine speed of 1500 rpm the available calculation time before control intervention is needed is 45.0 ms for post fuel injection and 34.4 ms until the start of main water injection. When using efficient controllers these time restrictions can be met using state of the

art processor based ECU's. However, when considering a control interaction of either fuel or water shortly after EVC a very short calculation time is available of around 0.22 ms. This timing constraint is extremely difficult to meet using a traditional microprocessor based ECU but can be easily achieved when using a FPGA based ECU. This fast calculation time of the FPGA makes it desirable for use as an in-cycle engine controller.

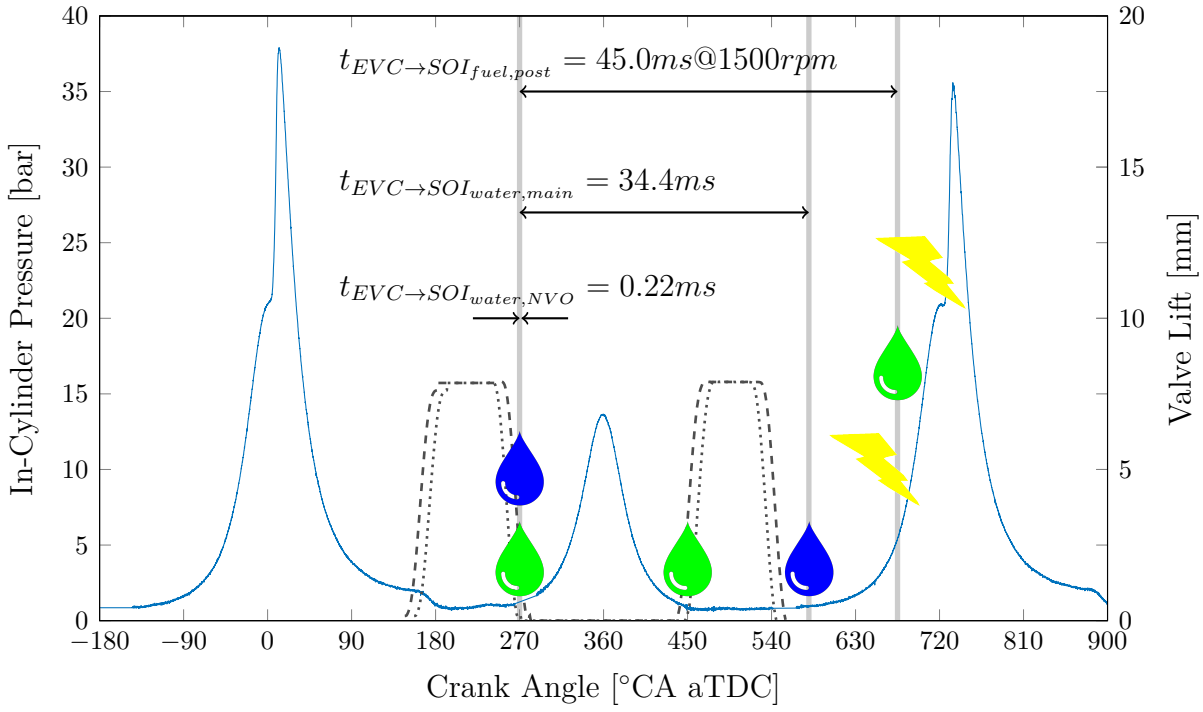

Figure 2.8: HCCI control variables and available calculation time from EVC.

2.4 Impact of Direct Water Injection

Direct water injection has been investigated for use in both traditional spark ignition [60] and compression ignition [61] engines along with HCCI engines [34]. Often water injection is used to cool the cyclinder charge increasing the air density and thus the amount of fuel which can be added for increased power output [62]. The cooling of the cylinder charge also leads to NO_x emission reductions [63]. The use

of water injection in engines has various commercial interests as it provides engine power improvements while also allowing for emission reductions which can be seen by the numerous patents in the area [64–67].

Although there are great advantages when using water injection for expanding the load range and reducing the emissions levels there are also challenges including high water quality requirements, large injected water-to-fuel quantities, and corrosion challenges [34].

The total heat absorbed by the injected water, Q_{H_2O}, is the amount of energy required to heat the water, its evaporation and superheating of the gaseous water, assuming the pressure inside the combustion chamber does not change during the injection, can be calculated using the following equation:

$$Q_{H_2O} = \Big[\big(c_{p,H_2O,l} + c_{p,H_2O,g}\big)dT_{cyl} + q_{evap}\Big]m_{H_2O} \tag{2.7}$$

In which $c_{p,H_2O,l}$ and $c_{p,H_2O,g}$ are the specific heat capacity of water as a liquid and a gas at a constant pressure. dT_{cyl} is the temperature change of the cylinder contents, q_{evap} is the evaporation energy of water and m_{H_2O} is the mass of injected water.

As the evaporation energy is several orders of magnitude larger than the other components, all components except the evaporation enthalpy are neglected. The equation is therefore simplified to:

$$Q_{H_2O} = q_{evap}m_{H_2O} \tag{2.8}$$

Then using equation 2.8, the energy absorbed by the water can be calculated and the cooling of the cylinder charge can be calculated. This reduction in temperature is a valuable control variable as HCCI is highly dependent on the cylinder state to determine the start of combustion. Currently, water injection is primarily used for

expanding the load range and reducing emissions of the internal combustion engine. This area is currently well researched both in previous and current projects, however, this thesis focuses on using water injection only on cycles which require it to improve the combustion stability of HCCI. Therefore, relatively small amounts of water are required as water is only injected in selected cycles.

Chapter 3

Experimental Setup

3.1 Engine Assembly

All experimental results reported in this thesis are performed on a Single Cylinder Research Engine (SCRE) located at Lehrstuhl für Verbrennungskraftmaschinen (VKA) (Institute for Combustion Engines) located in Aachen, Germany. The SCRE is outfitted with a fully variable Electromagnetic Valve Train (EMVT). This engine has been specifically designed to operate with the EMVT system and provide optical access to the combustion chamber. Therefore, there are two engine setups, one with an cylinder head designed with optical access and a piston with a glass window. The second setup is a thermodynamic setup where the optical access is removed in favor of a more robust metal cylinder head.

Due to manufacturing delays with the thermodynamic cylinder head, the optical cylinder head was used for some experiments in this thesis, however, no optical measurements were made. The problem with the optical setup is the sealing between the head and cylinder sleeve causes higher blow-by than the thermodynamic setup. The cylinder head being used will be noted in future sections.

To protect the valves against a possible collision, the piston pictured in Figure 3.1 has been manufactured with deep valve pockets to allow space between the open

valves and the piston face at Top Dead Center (TDC) thus making the engine free running. Both the thermodynamic and optical setup pistons are the same shape therefore in addition to deep valve pockets there is a large flat spot in the center of the piston where glass can be added to provide optical access. This lowers the cylinder compression ratio to 12:1.

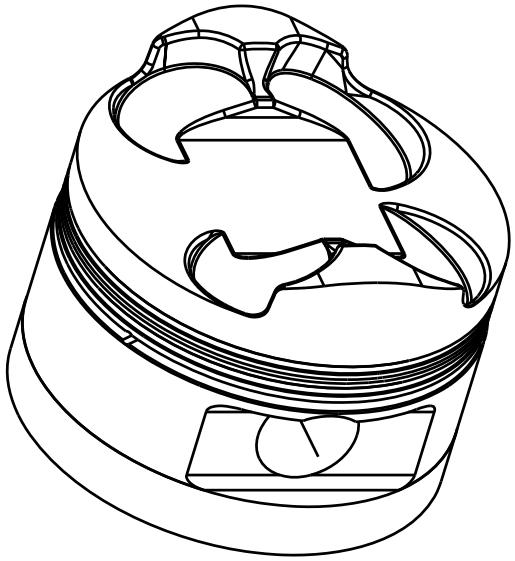

Figure 3.1: Schematic of the piston used.

The engine is pictured in Figure 3.2 with the engine specifications and testing conditions defined in Table 3.1.

3.1.1 Electro-magnetic valve train

The flexibility of the valve timing allows for any desired valve timing to be implemented and changed on a cyclic basis if desired. Engine operation with combustion chamber exhaust gas re-circulation through NVO is useful for HCCI combustion and can be easily achieved with this setup. This allows for a wide operating range of HCCI combustion timings to be implemented. The FEV Europe GmbH (FEV) designed EMVT system is depicted in Figure 3.3 [68, 69]. This figure shows an armature

Figure 3.2: Photograph of single cylinder research engine with electromagnetic valve train.

which is located between two electromagnetic coils, one to provide opening force and one to close the valve. Two valve springs provided the restoring force to return the valve to its resting position of half open. The position of the electromagnetic valves are measured using FEV conductive lift measurement sensors. The position of the valve is used for closed-loop control of the valve position, which will be discussed later.

3.1.2 Engine torque and speed

The dynamometer controller is set to hold speed constant despite changing engine torque for all experiments is this work. The engine speed is regulated to a set value

Table 3.1: Single cylinder research engine parameters

Parameter	Value
Displacement volume	0.499 L
Stroke	90 mm
Bore	84 mm
Compression ratio	12:1
No. of valves (In/Ex)	2/2
Valve train	EMVT
Max. valve lift (In/Ex)	8 mm/8 mm
Valve angle (In/Ex)	22.5°/22.5°
Valve diameter (In/Ex)	32 mm/26 mm
Intake air pressure	1013 mbar
Exhaust pressure	1013 mbar
Oil and coolant temperature	90 °C
Engine speed	1500 rpm
Fuel rail pressure	100 bar
Intake temperature	50 °C

and the torque produced by the engine is measured using a HBM U2A 0.1 load cell. The angular position of the engine is measured using a Heidenhain ROD 430 encoder which has a 0.1 degree angular resolution.

3.1.3 Pressure sensors

The in-cylinder pressure is measured using a using a Kistler A6061B piezoelectric pressure transducer that is mounted between the intake and exhaust valves. The intake and exhaust manifold pressures are measured using Kistler 4045-A5 piezoresistive pressure transducers. To convert the output from the three pressure sensors to a voltage, three Kistler charge amplifiers are used. Each charge amplifier and pressure transducer are calibrated as a pair to reduce the amount of measurement error.

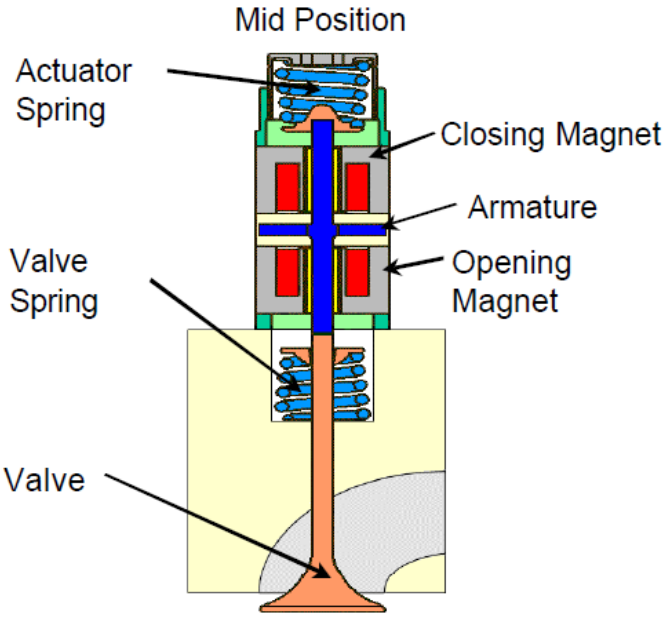

Figure 3.3: Electromagnetic valve schematic from [70].

3.1.4 Fuel system

The fuel used for all testing in this work is conventional European Research Octane Number (RON) 96 gasoline containing 10% ethanol. The fuel is pressurized first using a low pressure fuel pump up to 6 bar and then up to 100 bar using a high pressure pump before injection directly into the combustion chamber. The fuel pressure is measured using a rail pressure transducer. The amount of fuel injected is measured using a FEV Seppeler fuel measurement system. This system can only be used for steady state fueling measurements, as is requires multiple cycles to record the time to inject a known volume of fuel. However, it can also be used to calibrate an injector function to determine the fuel injected for a known injection duration for in-cycle measurements.

The fuel injector used as a BMW 13537589048 piezoelectric outward-opening hollow cone injector. This injector is powered by Siemens VDO injection controller which is used to provide the necessary voltage to open the injector.

3.1.5 Water injection

Similar to the fuel injection system, the distilled water that is direct injected into the combustion chamber is first pressurized to 6 bar using a low pressure pump. Then an electronically controlled high pressure pump is used to pressurize the water to injection pressure ranging from 15-175 bar. This pressure is measured using a rail pressure transducer and is used for closed-loop control of the rail pressure.

The direct injection of water is provided through a BMW 13537589048 piezoelectric outward-opening hollow cone injector. This injector is powered using VEMAC VAPA power electronics which provide the required voltage to open the injector. It also allows for customization of the injection opening profile, however, for this work the opening profile was not adjusted.

3.1.6 Manifold air conditioning

The intake air is conditioned before it reaches the engine. Using two Roots-type superchargers powered by a variable frequency drive controlled electric motor the intake pressure can be adjusted up to 1.8 bar boost. The temperature of the intake air is also controllable using an in-line air heater to provide various intake temperatures and is controlled using the ADAPT system described later. The volume of air entering the engine is measured using an Aerzen gas flow meter which provides an overall flow rate entering the engine.

The exhaust back pressure can also be controlled using a pneumatically powered valve. For this work the back pressure in the exhaust system is regulated to 1013 mbar $\pm$ 25 mbar for all experiments.

3.1.7 Cooling water and oil supply

The engine coolant is run through a flat plate heat exchanger which is connected to the building cooling water system. This helps to remove heat from the engine while in operation. The engine coolant temperature can also be increased using a electric heater which is controlled using the ADAPT system. For all tests the coolant temperature is maintained at 90 °C ±2°C.

The oil is supplied to the engine through an external oil conditioning system which filters, heats and pressurizes the oil which is supplied to the engine. The oil temperature is regulated to 105 °C ±2°C which helps to ensure any water in the oil is evaporated. The oil pressure is set to 5.4 bar ±0.2 bar for all experiments in this work.

3.1.8 Emissions measurement

An emission measurement system is used to determine the composition of exhaust gas. The two measurement devices used are an Eco Physics CLD700REht for NO and NOx measurement and a Rosemount NGA 2000 which provides measurements of unburnt hydrocarbons, carbon monoxide, carbon dioxide, and oxygen concentration. The specifications of the emission measurement system is provided in Table 3.2.

Table 3.2: Accuracy of emissions measurement system

Gas	Maximum	Detection level	Resolution	Accuracy
NOx	10000 ppm	0.1 ppm	0.1 ppm	1% of reading
uHC	5%	0.04 ppm	0.1 ppm	1% of reading
CO (low)	2500 ppm	0.1ppm	0.1ppm	1% of reading
CO (high)	10%	0.1%	0.1%	1% of reading
CO2	18%	0.1%	0.1%	1% of reading
O2	25%	0.1%	0.1%	1% of reading

3.2 Engine control

Engine control is provided by three main systems. The first system is an A&D ADAPT system which provides control of engine operating parameters including load, speed, oil and water temperature and pressure, exhaust back pressure, and intake temperature. This system also is used for low speed data acquisition which is described in the following section.

The main engine control is provided by a dSPACE MicroAutoBox II (MABX) prototyping Engine Control Unit (ECU) which contains both microprocessor and FPGA modules. This ECU is used for the implementation of all control algorithms to provide control of the valves, ignition, water and fuel injection timing and water rail pressure. The software that is run on the MABX is complied using Matlab Simulink. This makes implementing and testing controllers easier and provides a user friendly interface. Another advantage of using the MABX is that it is connected to a computer running dSPACE ControlDesk which provides access to the variables in the control algorithms and allows for changes during engine operation. More detailed technical specifications are provided in Table 3.3.

A dSPACE DS1103 is used to provide closed-loop control of the EMVT system. The DS1103 runs an FEV created C-code based controller which uses the valve position sensors to determine the correct valve opening and closing currents based on the desired valve opening and closing times from the MABX. The DS1103 is also connected to the same computer running dSPACE ControlDesk as the MABX, this provides access to enable the starting sequence for the valves and allows for the maximum current applied to the EMVT's to be adjusted if necessary.

Table 3.3: Rapid prototyping ECU Specifications

	Parameter	Specification
Processor	dSPACE® 1401	IBM PPC-750GL
	Speed	900 MHz
	Memory	16 MB main memory
I/O Board	dSPACE® 1513	
	Analog input	24 Parallel channels
	Resolution	16 bit
	Sampling frequency	1 Msps
	Analog input	32 Multiplexed channels
	Resolution	16 bit
	Sampling frequency	200 Ksps
	Analog output	12 Channels
	Digital input	40 Channels
	Digital output	40 Channels
FPGA	dSPACE® 1514	Xilinx® Kintex-7
	Flip-flops	407600
	Lookup table	203800
	Memory lookup table	64000
	Block RAM	445
	Digital signal processing	840
	I/O	478

3.3 Data collection

Data collection for offline processing is recorded by two systems. The cyclic data is recorded using an FEV Combustion Analysis System (CAS) which records cylinder and manifold pressures along with engine angle, measured injection and ignition current, lambda, valve position, and other engine data at a 0.1 crank angle degree(CAD) resolution. The averaged data from all recorded cycles such as air flow, fuel consumption, emissions composition, and various temperatures including intake, exhaust, coolant, oil, and cylinder head temperature are recorded using the A&D ADAPT system. This data is recorded at a sampling rate of 10 Hz and averaged for the complete measurement set. The combination of the recorded data from both systems is used for the offline development of the engine gas exchange model and control described in later chapters of this thesis.

The ControlDesk computer is used to record results which were calculated on the processor and FPGA modules of the MABX. This data is used for the development and evaluation of the control applications running on the MABX. The extraction of values from the FPGA to processor in the MABX is limited to a sampling rate of 0.5ms to prevent overruns. This does not affect the operational speed of the FPGA but it does limit the data collected from the FPGA.

To ensure that the data recorded on the CAS system and MABX could be aligned the CAS was set to output a timing pulse at the start of recording which was then recorded on both the MABX and CAS systems. This timing pulse was used to align the online FPGA model with the identical CAS cycle. The same engine cycle is being compared when real-time and offline calculated results are presented throughout this thesis.

Chapter 4

Gas Exchange Model[1]

This chapter contains the development and experimental validation of a gas exchange model for HCCI engine operation with negative valve overlap. This process can be broken down into four main sections as highlighted in Figure 4.1. This figure provides a simplified overview of the conversion process and will be referenced throughout this chapter. The first step is the selection of a validated model based on physical governing equations. These equations are then used to develop a 0D physical gas exchange model created in Matlab Simulink, subsequently referred to as *offline physical model* which is used for offline calculation of the cylinder temperature, pressure and trapped mass. This offline physical model is compared to a standard commercial gas exchange model as a simple validation, this model is referred to as *reference model*. The offline physical model is used both as a reference for the real-time FPGA based model and in the development of the FPGA model, called the *FPGA offline model*. The final step is the hardware implementation and experimental validation of the *FPGA online model*.

[1]This chapter is based on [71]

1. Governing physical equations

$$u = h - \frac{pV}{m}$$

2. Offline physical model in Simulink

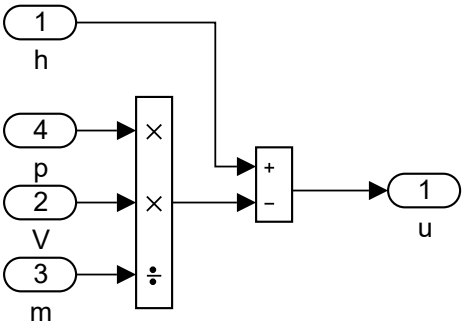

3. Offline FPGA model in Simulink XSG

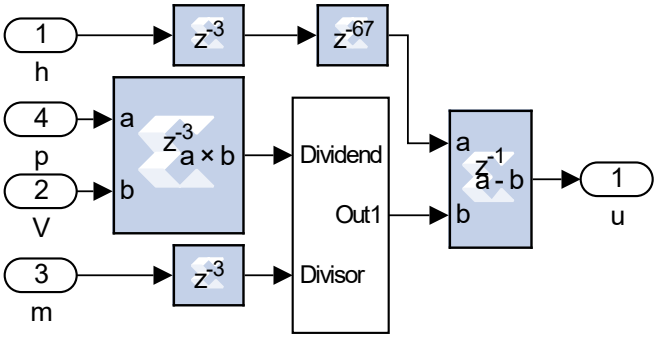

4. Online FPGA model for realtime operation

Figure 4.1: Model conversion to FPGA process overview.

4.1 Governing Physical Equations

As shown in Figure 4.1, the first step in the development of the gas exchange model is determining the relevant physical governing equations. This step is important as assumptions made at this step will affect the model performance and accuracy when it is used on the experimental engine.

The gas-exchange process is formulated in the offline physical model which is spatially lumped using the mass and energy conservation laws. This zero-dimensional approach indicates that the physical quantities are independent of location, making the process parameters only dependent on time. The change in crank angle, φ, is related to the time domain via $\mathrm{d}\varphi = \omega \mathrm{d}t$ where ω is the angular engine velocity.

4.1.1 Energy conservation for the cylinder

In-cylinder energy conservation, neglecting kinetic energy and latent heat of fuel evaporation, is:

$$\frac{\mathrm{d}U}{\mathrm{d}\varphi} + \frac{\mathrm{d}Q_b}{\mathrm{d}\varphi} = \frac{\mathrm{d}Q_w}{\mathrm{d}\varphi} - p\frac{\mathrm{d}V}{\mathrm{d}\varphi} + \sum_i h_i \frac{\mathrm{d}m_i}{\mathrm{d}\varphi} \tag{4.1}$$

in which $\mathrm{d}U/\mathrm{d}\varphi$ is the internal energy change, $\mathrm{d}Q_b/\mathrm{d}\varphi$ the fuel energy release, $\mathrm{d}Q_w/\mathrm{d}\varphi$ the wall heat transfer, $p\mathrm{d}V/\mathrm{d}\varphi$ the internal work and $h_i\mathrm{d}m_i/\mathrm{d}\varphi$ the intake and exhaust enthalpy flows.

The internal energy U of the trapped gas is defined as the product of the mass m and the specific internal energy u and through partial differentiation leads to:

$$\frac{\mathrm{d}U}{\mathrm{d}\varphi} = m\frac{\mathrm{d}u}{\mathrm{d}\varphi} + u\frac{\mathrm{d}m}{\mathrm{d}\varphi} \tag{4.2}$$

The specific internal energy, u, is dependent on the temperature T, the pressure p and the air/fuel-ratio λ. Therefore the differential equation of the specific energy can

then be expressed as:

$$\frac{\mathrm{d}u}{\mathrm{d}\varphi} = \frac{\partial u}{\partial T}\frac{\mathrm{d}T}{\mathrm{d}\varphi} + \frac{\partial u}{\partial p}\frac{\mathrm{d}p}{\mathrm{d}\varphi} + \frac{\partial u}{\partial \lambda}\frac{\mathrm{d}\lambda}{\mathrm{d}\varphi} \tag{4.3}$$

Equation 4.3 can be simplified by neglecting the impact of varying pressure on the specific internal energy ($\partial u/\partial p \approx 0$) and air/fuel-ratio ($\partial u/\partial \lambda \approx 0$) [11]. Finally, the gradient $\partial u/\partial T$ is defined as the specific isochoric heat capacity c_v, which results in:

$$\frac{\mathrm{d}u}{\mathrm{d}\varphi} = c_v\frac{\mathrm{d}T}{\mathrm{d}\varphi} \tag{4.4}$$

Using the above simplification the energy conservation equation 4.1 becomes:

$$m\left\{c_v\frac{\mathrm{d}T}{\mathrm{d}\varphi}\right\} = -\frac{\mathrm{d}Q_b}{\mathrm{d}\varphi} + \frac{\mathrm{d}Q_w}{\mathrm{d}\varphi} - p\frac{\mathrm{d}V}{\mathrm{d}\varphi} + \sum_i (h_i - u_i)\frac{\mathrm{d}m_i}{\mathrm{d}\varphi} \tag{4.5}$$

Equation 4.5 can then be rewritten to obtain an expression for the cylinder temperature gradient $\mathrm{d}T/\mathrm{d}\varphi$ given by:

$$\frac{\mathrm{d}T}{\mathrm{d}\varphi} = \frac{-\frac{\mathrm{d}Q_b}{\mathrm{d}\varphi} + \frac{\mathrm{d}Q_w}{\mathrm{d}\varphi} - p\frac{\mathrm{d}V}{\mathrm{d}\varphi} + \sum_i (h_i - u_i)\frac{\mathrm{d}m_i}{\mathrm{d}\varphi}}{mc_v} \tag{4.6}$$

The heat release based upon the measured crank angle resolved cylinder pressure $p(\varphi)$, can be determined by combining equations 4.5 with the ideal gas law ($pv = mRT$) and assuming a semi-perfect gas behavior ($R = c_p - c_v$ and $\kappa = \frac{c_p}{c_v}$) which reults in [11]:

$$\frac{\mathrm{d}Q_b}{\mathrm{d}\varphi} = -\frac{1}{\kappa - 1}V\frac{\mathrm{d}p}{\mathrm{d}\varphi} - \frac{\kappa}{\kappa - 1}p\frac{\mathrm{d}V}{\mathrm{d}\varphi} + \frac{\mathrm{d}Q_w}{\mathrm{d}\varphi} \tag{4.7}$$

It is defined that during the heat release, the transferred mass over the valves is zero. Additional simplifications are made by neglecting the blow-by mass flow, assuming ideal gas state and constant gas composition, $\mathrm{d}R/\mathrm{d}\varphi = 0$, and using the relations $R = c_p - c_v$ and $\kappa = c_p/c_v$. Now with the specific heat ratio, $\kappa(\varphi)$, the actual cylinder

volume $V(\varphi)$ and the cylinder pressure,$p(\varphi)$, all as a function of crank angle, the heat release term $\mathrm{d}Q_b/\mathrm{d}\varphi$ in equation 4.6 is modeled in equation 4.7.

The heat transfer to the walls of the combustion engine, $\mathrm{d}Q_w/\mathrm{d}\varphi$, is comprised of convection and radiation [72]. To simplify, the radiation part is incorporated into the convective heat transfer coefficient α which is a good approximation for gasoline engines [73]. The wall heat transfer can be expressed as:

$$\frac{\mathrm{d}Q_w}{\mathrm{d}\varphi} = \alpha(\varphi)\ A(\varphi)\ (T_w - T(\varphi)) \tag{4.8}$$

To calculate the heat transfer, both the spatially averaged gas temperature in the cylinder $T(\varphi)$ and wall temperature T_w are required. The wall temperature is assumed constant ($T_w = 465$ K) over an entire cycle with a dependency on engine load and speed, and the charge temperature can be obtained from the equation of state 4.1.

A widely accepted approach for the calculation of the heat transfer coefficient $\alpha(\varphi)$ in practical use for engines is from Woschni [74]. This correlation underestimates the the heat transfer coefficient at low engine loads and during operation without combustion. A revised approach uses the varying displacement volume as a characteristic length and is given by [75]:

$$\alpha(\varphi) = 130\ V^{-0.06}\ p^{0.8}\ T^{-0.4}\ (\nu_{pis} + 1.4)^{0.8} \tag{4.9}$$

which is commonly used for Diesel engines. It also approximates the high pressure gradient of HCCI combustion very well [58] so it is used in this work. The piston speed ν_{pis} in equation 4.9 is calculated as function of crank angle $\nu_{pis}(\varphi)$ and is given by:

$$\nu_{pis} = -R_{crk} * sin(\varphi) - \frac{R_{crk}^2 * cos(\varphi) * sin(\varphi)}{\sqrt{-R_{crk}^2 * sin(\varphi)^2 + L_{con}^2}} \tag{4.10}$$

Where R_{crk} is the radius of the crank shaft and L_{con} is the length of the connecting rod.

Then by using measured pressure and calculated cylinder volume and temperature the integration of the rate of heat release over the duration when combustion is occurring yields the heat release as function of the crank angle:

$$Q_b(\varphi) = \int_{\varphi_{SOC}}^{\varphi_{EOC}} dQ_b(\varphi) \tag{4.11}$$

Consideration of combustion reactions during the NVO recompression phase is an important effect to incorporate if there is a misfire in the previous cycle. The heat release during the NVO phase, $\mathrm{d}Q_{NVO}/\mathrm{d}\varphi$, has been modeled according to equation 4.7. In Figure 4.2, the effect of including the heat release $\mathrm{d}Q_{NVO}/\mathrm{d}\varphi$ on the in-cylinder pressure is visualized.

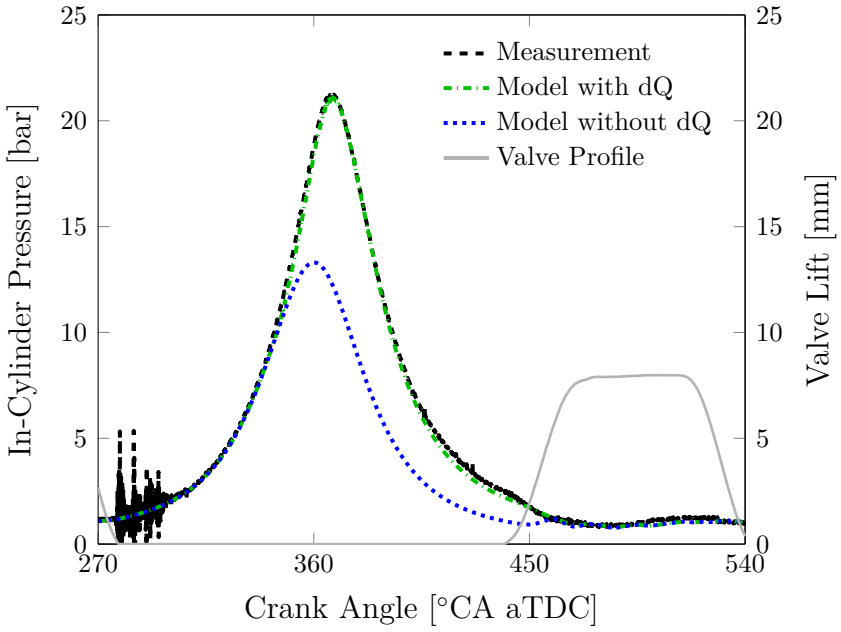

Figure 4.2: In-cylinder pressure during the NVO recompression phase. The offline physical model is able to accurately capture the heat release if combustion occurs and calculate the corresponding cylinder pressure.

As can be seen in Figure 4.2, the model without heat release simulates the lack of combustion, leading to a difference in peak pressure of 10 bar compared to the combustion case. Even though this NVO combustion shown in Figure 4.2 is an extreme scenario which occurred approximately once every 100 cycles at a very unstable operating point these are the cycles that the controller developed in the following chapter will try to eliminate so it is important to capture this combustion.

4.1.2 Gas Properties

The internal energy u of the burned gas can be obtained from multiple modeling approaches [76]. A simplified approach where the internal energy is dependent on the gas temperature and air-fuel ratio is described in [77]. This approach was then extended by [78] to also consider the pressure dependency. However, both approaches are only valid for the Diesel process and an air-fuel ratio of $\lambda \geq 1$ and where the composition of the gas is assumed constant.

The combustion chamber can also be treated as a mixture of individual species for which each of the species is considered an ideal gas [10, 79]. The model is then based on polynomial curve fits to the thermodynamic data for each species in the mixture. The specific heat $c_{p,i}$ is approximated for each species i at temperature T as:

$$\frac{c_{p,i}}{R} = a_{i,1} + a_{i,2}T + a_{i,3}T^2 + a_{i,4}T^3 + a_{i,5}T^4 \tag{4.12}$$

where the coefficients $a_{i,j}$ can be obtained from thermodynamic tables. The enthalpy h of species i is then given by:

$$\frac{h_i}{R} = a_{i,1} + \frac{a_{i,2}}{2}T + \frac{a_{i,3}}{3}T^2 + \frac{a_{i,4}}{4}T^3 + \frac{a_{i,5}}{5}T^4 + \frac{a_{i,6}}{T} \tag{4.13}$$

The specific internal energy u of species i can now be obtained by:

$$u_i = h_i - RT \tag{4.14}$$

Using the species internal energies and their mass fractions χ, the internal energy of the mixture is:

$$u_{mix} = \sum_i \chi_i \cdot u_i \tag{4.15}$$

which, as opposed to the previously mentioned modeling approaches, can be applied for any C/H-ratio and a wider range of gases.

4.1.3 Mass Conservation

The gas exchange process of the combustion chamber requires modeling of the intake and exhaust mass flows. The in-cylinder mass and composition at Intake Valve Closing (IVC) can be determined by using the mass flows and a mass balance. The theoretical (isentropic) one-dimensional stationary flow through a channel is defined as [80]:

$$\frac{\mathrm{d}m_{th}}{\mathrm{d}\varphi} = A_s \, \rho_s \sqrt{\frac{2\kappa}{\kappa - 1} RT_0 \left[1 - \left(\frac{p_1}{p_0}\right)^{\frac{\kappa-1}{\kappa}}\right]} \tag{4.16}$$

in which ρ_s and A_s are the isentropic density and flow area, and p_0 and p_1 the pressure before and after the intake and exhaust valves, respectively. Equation 4.16 is valid until the downstream pressure drops below the critical pressure, $p^\star$, or into the chocked flow regime. The critical pressure is given by:

$$\frac{p^\star}{p_0} = \left(\frac{2}{\kappa + 1}\right)^{\frac{\kappa}{\kappa-1}} \tag{4.17}$$

For the chocked flow operation equation 4.16 becomes:

$$\frac{\mathrm{d}m_{th}}{\mathrm{d}\varphi} = A_s\ \rho_s\ \sqrt{\frac{2\kappa}{\kappa-1}RT_0\Big(\frac{2}{\kappa+1}\Big)^{\frac{\kappa+1}{\kappa-1}}} \tag{4.18}$$

Since the compression in a combustion engine is not isentropic and throttling losses occur equations 4.16 and 4.18 must be adjusted using experimental data. To parameterize the model an experimental flow measurement is required to measure the thermodynamical effect of the throttle losses. These losses are quantified by the irreversible increase in entropy. To do this, the mass flow through the valve is normalized to the theoretical (isentropic) mass flow. This throttle loss is expressed as a flow coefficient α, which is defined as the relation between the effective and theoretical mass flow as:

$$\alpha = \frac{A_s}{A_{eff}} \tag{4.19}$$

The intake and exhaust mass flows are then calculated by substituting equation 4.19 into equations 4.16 and 4.18.

4.1.4 Injector Model

The injector model used to estimate the injected fuel mass m_f [58] is:

$$m_f = t_{inj}\alpha_f A\sqrt{2\rho_f\Delta p} \tag{4.20}$$

where t_{inj} is the the injection duration, Δp is the pressure difference between the fuel rail and cylinder, ρ_f the fuel density and A the orifice area. The flow coefficient α_f is a function of t_{inj} to take the non-linear opening and closing behavior of the injector into account. The injector model was calibrated on a test bench by performing multiple measurements and then fitted with a non-linear regression as shown in Figure 4.3.

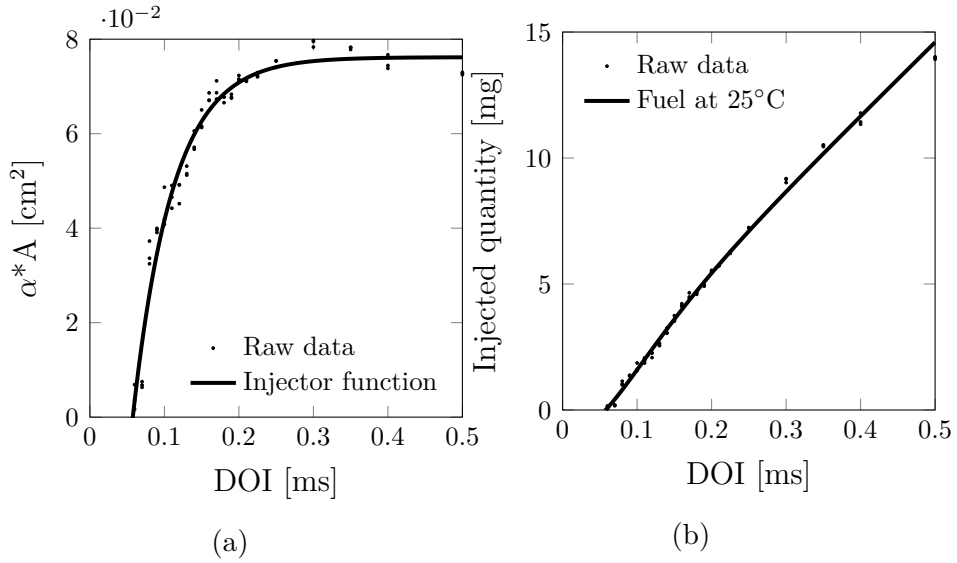

Figure 4.3: Injector test bench calibration data. A) Correlation of duration of injection DOI, flow coefficient α and injector cross section A. B) Injected fuel and water quantity as function of duration of injection DOI.

4.1.5 Real-Time Residual Fuel Mass Calculation

The calculated heat release during the main and NVO compression is used to calculate the fuel mass, m_f, present in the combustion chamber at any point throughout the cycle. The conversion of fuel during combustion and portion of unburned fuel leaving through the exhaust should be subtracted from the injected fuel mass $m_{f,inj}$:

$$m_f = m_{f,inj} - m_{f,b,main} - m_{f,ex} - m_{f,b,NVO} \tag{4.21}$$

Where $m_{f,b,main}$ and $m_{f,b,NVO}$ is the mass of fuel burned in the main and NVO compression phases. $m_{f,ex}$ is the mass of fuel that leaves the combustion chamber in the exhaust gas.

The combustion of fuel during the main combustion and NVO recompression can be obtained from there respective heat release, Q_b, and the lower heating value (LHV)

of the fuel:

$$m_{f,b} = \frac{Q_b}{LHV} \tag{4.22}$$

The unburned fuel mass leaving via the exhaust, $m_{f,ex}$, is determined by assuming the residual fuel is homogeneously distributed in the exhaust gas and can be determined by the mass fraction of exhaust gas, x_{ex}, multiplied by the residual fuel mass at EVO, $m_{f,EVO}$:

$$m_{f,ex} = \frac{m_{cyl,EVO} - m_{cyl,EVC}}{m_{cyl,EVO}} m_{f,EVO} = x_{ex}\, m_{f,EVO} \tag{4.23}$$

in which the exhaust gas fraction x_{ex} is defined as the fraction of the total in-cylinder mass leaving the combustion chamber. The implementation of fuel mass calculation yields continuous information about the current fuel mass present in the combustion chamber as shown in Figure 4.4. Residual fuel transferred from previous cycles is therefore also accounted for.

4.2 Offline Physical Gas Exchange Model Creation

To obtain crank angle resolved information on the in-cylinder state during the gas exchange process, an offline physical 0D gas exchange model was created in Matlab Simulink, shown in step 2 of Figure 4.1. This offline Simulink model is based on equations 4.6 to 4.20 with simplifications as described in the previous section. This model is extremely important in the development of the real-time FPGA model as it provides the values of intermediate calculations which can be used as validation of the final FPGA model. The offline model also allows for the FPGA gas exchange model to be tested offline to determine the error resulting from various simplifications.

The reliance of the governing equations on each other make the model creation challenging as results of one equation are used in subsequent calculations. Schemati-

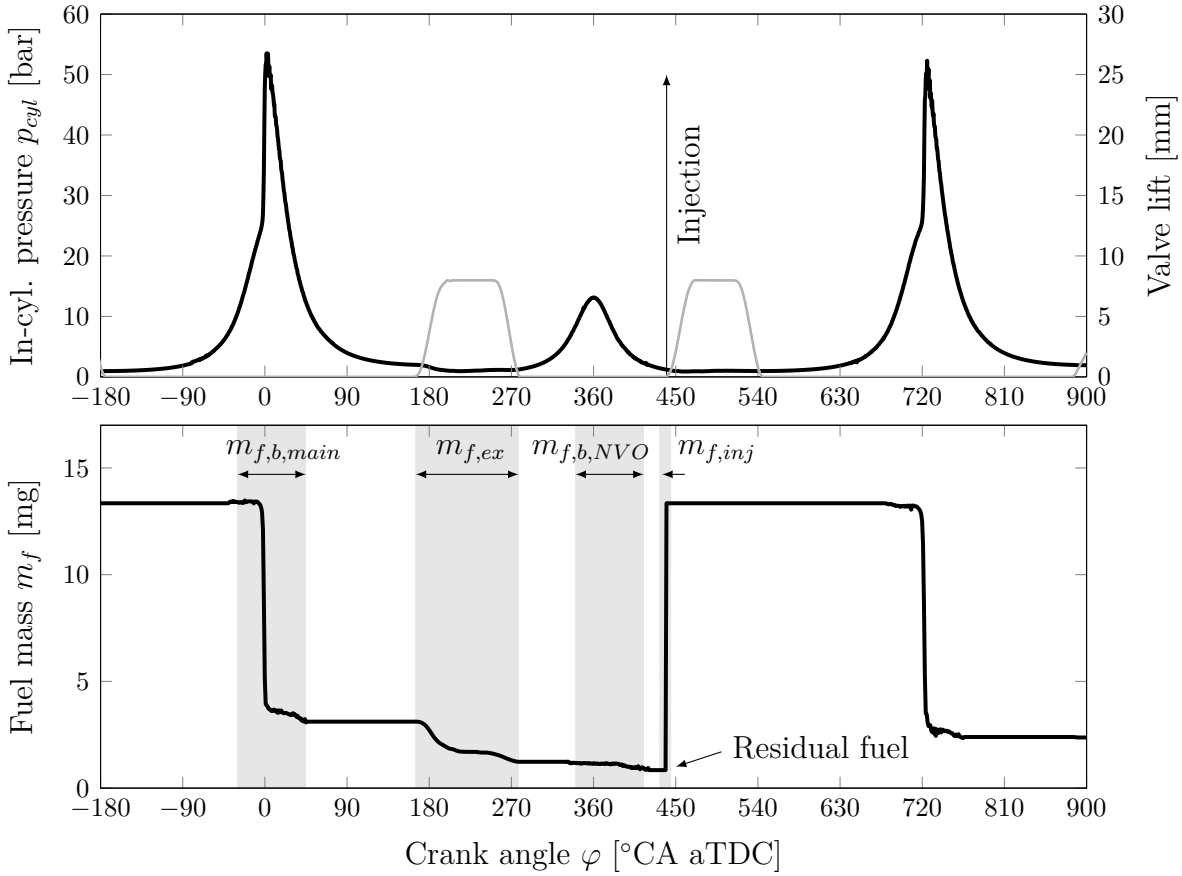

Figure 4.4: Effect of increasing model crank angle resolution on modeled cylinder mass.

cally this interdependence is shown in Figure 4.5. The model input is a set of discrete test bench data: the intake, exhaust and indicated cylinder pressure, crank angle position and intake and exhaust temperature as well as the measured valve lift.

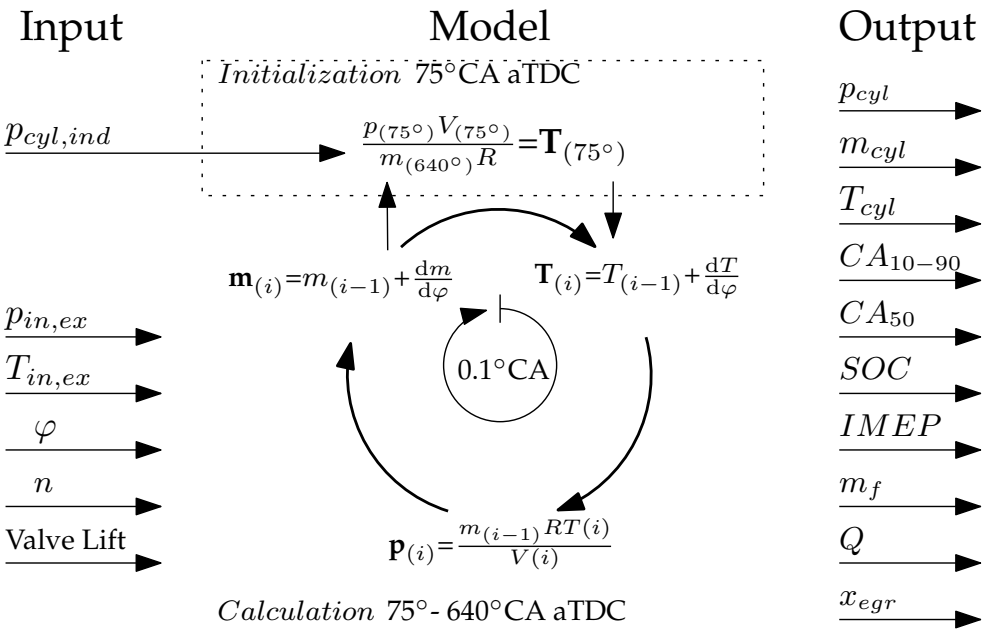

Figure 4.5: Schematic overview of the offline 0D physical gas exchange model created in Simulink.

In this calculation loop, the calculated instead of indicated cylinder pressure is used. The motivation behind that is the unavoidable sensor noise that is present in the indicated cylinder pressure, especially at valve closings. The mass flow calculation, equation 4.16, is extremely sensitive to pressure fluctuations, and shows unrealistic results when using the measured unfiltered cylinder pressure signal. Using a calculated cylinder pressure also helps to compensate for pressure sensor drift. During the combustion phase, 640-75°CA after Top Dead Center (aTDC), the calculated pressure is set equal to the measured in-cylinder pressure, since no combustion model is currently incorporated.

A calculation loop applies the temperature gradient in equation 4.6 to calculate

the current temperature (i.e. $T_i = T_{i-1} + \frac{\mathrm{d}T}{\mathrm{d}\varphi}$) and other values of interest such as EGR % and cylinder mass, m_{cyl}, during one sample period. First, the indicated cylinder pressure is referenced using a thermodynamic zero-point correction to the intake manifold pressure to determine the absolute cylinder pressure and to initialize the model. Initialization takes place only once every cycle during the expansion phase before Exhaust Valve Opening (EVO), the in-cylinder temperature is calculated using the ideal gas law.

After initialization the cylinder pressure is calculated from the cylinder temperature using the ideal gas law. This calculated cylinder pressure is combined with the measured manifold pressures to calculate cylinder mass using equation 4.16. This cylinder mass is then used in equation 4.6 to calculate the temperature gradient and subsequently the cylinder temperature. This calculation loop takes place during the gas exchange process from before EVO at 75°CA aTDC to after IVC at 640°CA aTDC at a rate of 0.1°CA.

The calculated cylinder mass is used in the internal energy $u_i \frac{\mathrm{d}m_i}{\mathrm{d}\varphi}$ term in equation 4.6, and with the remaining four terms a temperature offset $\frac{\mathrm{d}T}{\mathrm{d}\varphi}$ is obtained to update the temperature of the next calculation period. As a result, the calculated pressure, temperature and mass are delayed by one calculation period or 0.1°CA. This delay is an important benefit of the model as it makes the model causal. This eliminates the need for a prediction in favor of rapid calculation.

The resolution of the model has an effect on the convergence of the calculated parameters. In Figure 4.6, the cylinder mass has been modeled with four different resolutions. The model converges as the resolution increases from 5° to 0.1°CA which is the resolution that the data is recorded for offline analysis. Increasing the sample time past 1°CA does not change the calculation result showing that the model has converged. Therefore, a resolution of this value or less should be used with minimal impact on the model output. However, the higher resolution of 0.1°CA will be used

for the model development to utilize the full resolution of the engine encoder. For HCCI combustion analysis, 0.1°CA sampling is often used and will be used with the real-time model to provide a valid comparison. For this reason a resolution of 0.1°CA is used in the remainder of this work.

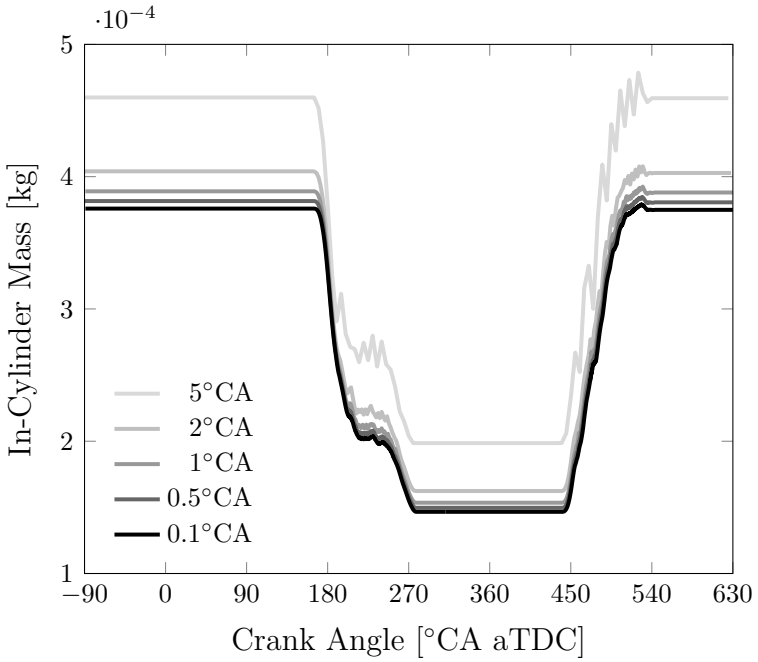

Figure 4.6: Effect of increasing model crank angle resolution on modeled cylinder mass.

4.2.1 Model Validation

Commercial software, GT-Power®, which combines a 0D combustion calculation with a 1D gas exchange calculation was used as a reference model to validate the offline physical model [81–83]. The same test bench data is used as input for both the offline physical and reference models for comparison and validation. The areas of interest for HCCI are the NVO recompression phase and intake/exhaust valve events for the mass flow calculation. The first validation step was to compare the calculated in-cylinder pressure to the reference model and measured pressure, as shown in Figure 4.7. The

calculated in-cylinder pressure of the offline model matches the reference pressure trace to within 0.08 bar.

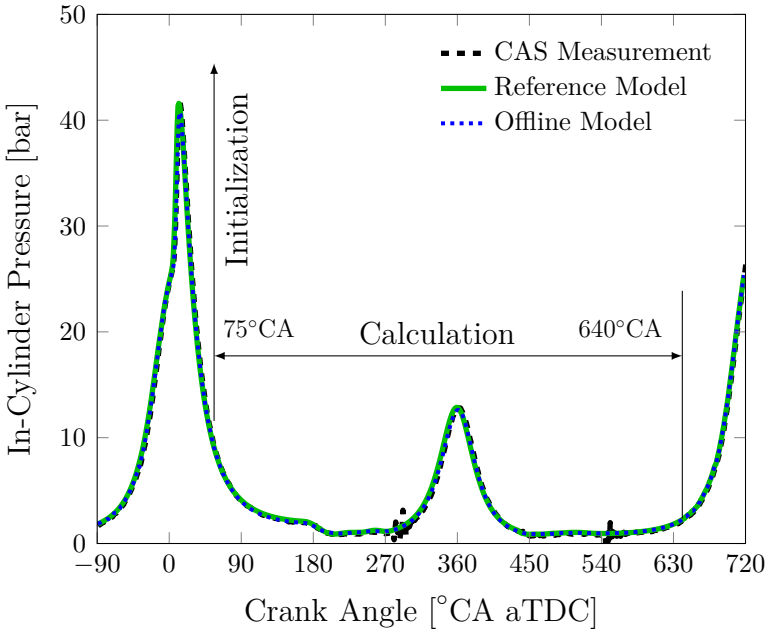

Figure 4.7: Validation of the modeled in-cylinder pressure with the reference model at 1500 rpm and 4.0 bar IMEP.

The 1D gas exchange process in the reference model incorporates gas dynamics, which include the spatial and temporal expansion of pressure waves in the intake and exhaust runner volumes, and the calculation of friction losses and wall heat transfer [84]. This inertia and spatial difference (sensor location) adds an additional phase shift effect to the pressure signals, therefore imposing a deviation in the mass flow calculation. To examine these differences, the offline model was also simulated with intake and exhaust pressure traces that include the gas dynamics, as calculated by the reference model. In Figure 4.8, the intake and exhaust pressure traces have been visualized, both without and with incorporation of gas dynamics. The gas dynamics appear to reduce the noise, as to be expected from the inertia of the exhaust and intake flow. Furthermore, the amplitude of the pressure fluctuations is increased in the offline model which considers gas dynamics. The modeled in-cylinder temperature with

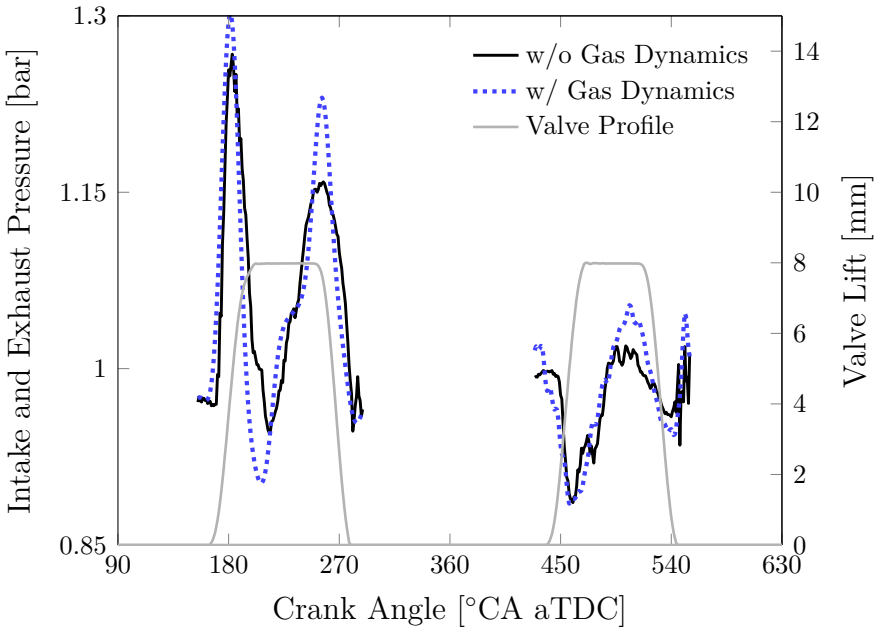

Figure 4.8: Comparison of the intake and exhaust pressure traces with and without incorporation of the gas dynamics at 1500 rpm and 4.0 bar IMEP.

and without consideration of gas dynamics, together with the reference temperature is shown in Figure 4.9. The modeled temperature matches the reference temperature, especially during the valve events where a difference of 25 K or 2.8% difference is seen. During NVO recompression the temperature difference between the model and reference increases to 40 K or 2.9%. A larger deviation of close to 80 K can be observed shortly before IVO at the start of injection. The enthalpy of evaporation has not been modeled in the offline model, causing this difference. The mass flow rate with gas dynamics included is visualized in Figure 4.10, where the offline model captures the flow trends seen in the reference model. The pulses in the exhaust mass flow rate show the same amplitude and no phase delay. The same can be observed during the intake mass flow. Both models consider the back-flow during valve events by using the properties of the cylinder mixture at cylinder or manifold conditions depending on flow direction.

Accumulation of the mass flow rates yields the cylinder mass, as shown in Figure

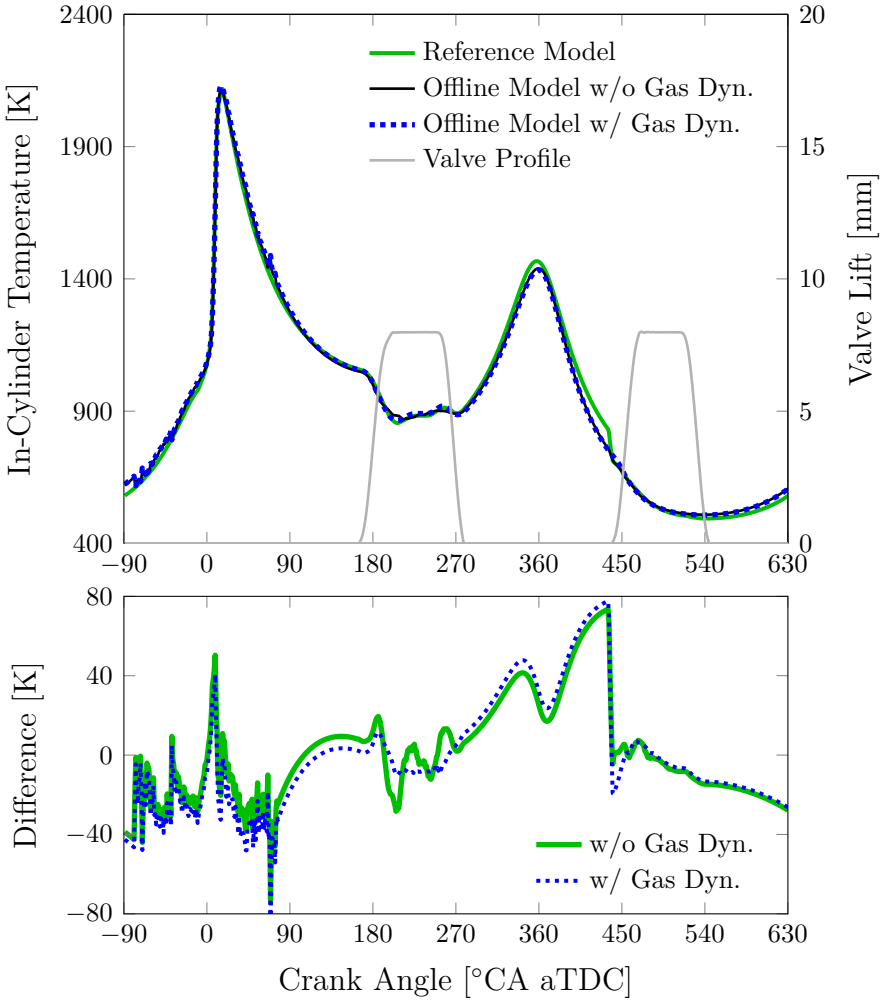

Figure 4.9: Validation of the modeled in-cylinder temperature with the reference model at 1500 rpm and 4.0 bar IMEP. Temperature difference shown.

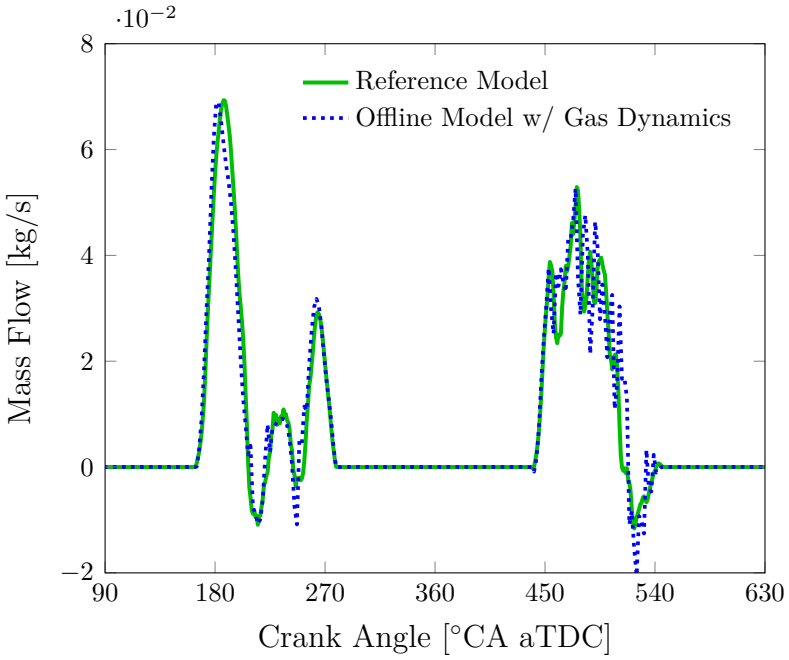

Figure 4.10: Validation of the modeled mass flow with the reference model at 1500 rpm and 4.0 bar IMEP.

4.11. The offline model without gas dynamics deviates from the reference model during the exhaust phase, and fails to simulate the re-breathing shortly before IVC. At these points, the deviation increases to 21.4 μg or 11.3% of the total mass which can be seen in the error plot in Figure 4.11. However, a slight offset during the valve events is less significant. On the other hand, the offline model with gas dynamics matches the reference model during these events. Despite the differences in the offline model due to the lack of gas dynamics, the cylinder mass tracks the reference model to within 3 μg or 0.8%, when the valves are closed. As a result, the offline model is able to calculate the in-cylinder mass sufficiently well without incorporation of gas dynamics.

An additional remark is that the mass at 90°CA aTDC and 630°CA aTDC are not identical. The cyclic- and pressure fluctuations result in imbalanced exhaust and intake mass flows. Typically any engine experiences cyclic variation and HCCI operation is no different so differences in mass flow and trapped in-cylinder mass are

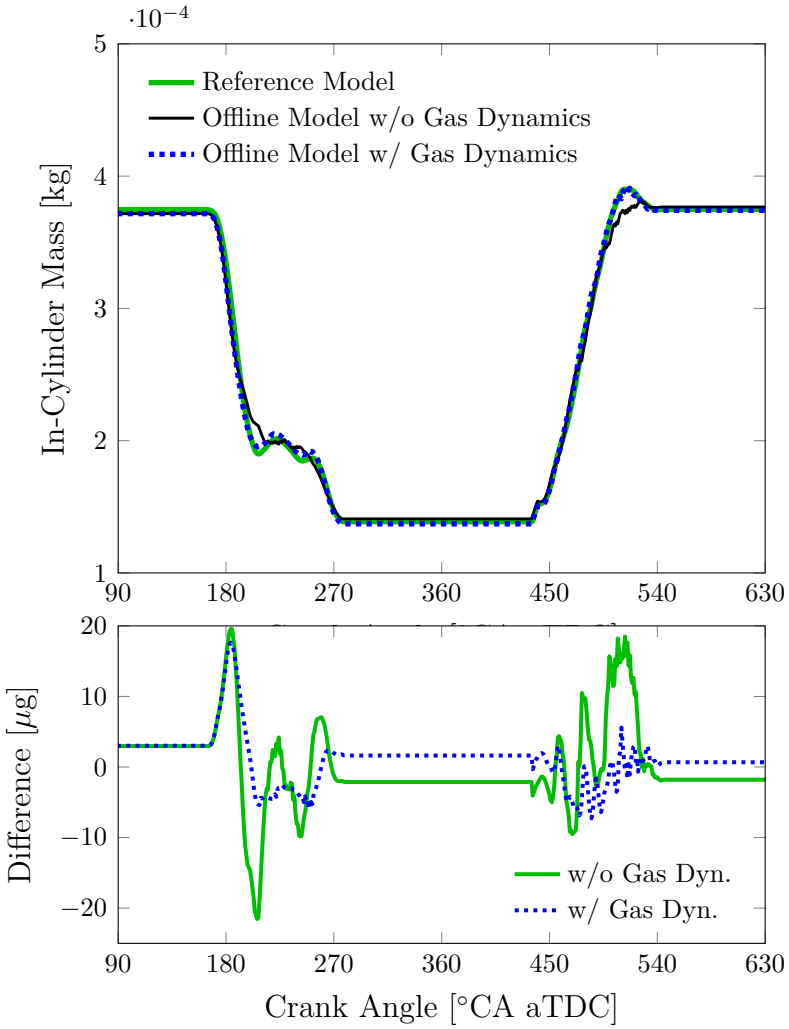

Figure 4.11: Validation of the modeled in-cylinder mass with the reference model at 1500 rpm and 4.0 bar IMEP.

expected. Some HCCI operating points are very stable cycle-by-cycle while others show significant variability. This work is considered with the high variation HCCI operating points.

In the reference model, each cycle is calculated by means of 200 iteration steps to allow the effect of initial conditions on the simulation to be removed, until steady-state is reached. The output of one iteration step serves as input for the following one. The offline physical model does converge due to it's causal nature, however, it does not incorporate this iterative process which could resulting in minor differences in cylinder mass for large cyclic fluctuations.

The calculation time for the reference model to run 200 iterations of a single combustion cycle makes it not viable as a real-time capable model as it takes 3 hours per cycle on a standard PC. By validating the developed model against widely used industry software and getting comparable results shows that the developed offline model provides a reasonable calculation of the cylinder state. We have now seen that the offline model is able to capture the cylinder state however it is not real-time capable. In the next section this model will be converted to FPGA for real-time operation.

4.3 Conversion to FPGA

For realtime application it is necessary to convert equations 4.6 to 4.9 of the offline physical Simulink model to an FPGA based model as highlighted in Figure 4.1. To allow for operation of the above Simulink-based gas exchange model on the Xilinx® FPGA hardware the model must be adapted to use Xilinx® System Generator (XSG) library blocks. These blocks are specifically designed to simplify the development of an FPGA based model. The FPGA model creation consists of individually transferring each Simulink block from the offline physical model to its XSG equivalent while

understanding the limitations of the FPGA hardware.

Generally, the basic mathematical operations of addition, subtraction, multiplication and logical comparisons are resource efficient and can be easily implemented using existing XSG blocks. However, many standard Simulink library blocks used in the offline physical model must be replaced with basic arithmetic for implementation on FPGA. In this work, the following mathematical operations needed to be recreated to allow for the fixed-point arithmetic used in the FPGA: division, windowed averaging, integration, moving average filtering and edge detection. An example of this transition from Simulink to XGS blocks can be seen in Figure 4.1 and will be further explained in the following section.

4.3.1 FPGA Hardware Limitations

As described in Section 2.2, a FPGA consists of many gate arrays connected with re-configurable routing fabric containing switch points or routing blocks between the gate arrays. The various logic blocks can be used for simple combination logic (lookup tables) or may be flip-flops which allow for sequential logic [44, 45]. Also included on the FPGA board are random access memory (RAM) blocks distributed between the logic blocks which provide an efficient method for data storage.

A limitation of using gate arrays is that fixed point arithmetic must be used. This forces the model designer to consider the binary precision at every calculation (scaling of all variables) and also limits the mathematical arithmetic that is possible. The offline physical model, discussed above, allows for estimating the range of values that will result from each operation. It is also important to consider the value or specifically the binary position, of any two values before a mathematical operation to ensure they are of similar size. This is to reduce calculation error due to a overflow or loss in precision due to truncation of the result. In the development of the gas exchange model due to the large magnitude difference in SI units for pressure, volume

and temperature this problem occurs and scaling must be used. In addition, correctly setting the binary size is important in allocating the correct amount of resources to extremely sensitive calculations while saving resources by reducing the bit size for calculations that do not require it.

Figure 4.12 shows an example of the XSG blocks used to create the FPGA model. This example is the calculation of the residual fuel mass as given in Equation 4.23 and highlights the binary precision at each calculation step. As described previously the offline model is used for the estimation of the values possible from the calculation and the result of each calculation step is truncated to the correct binary precision.

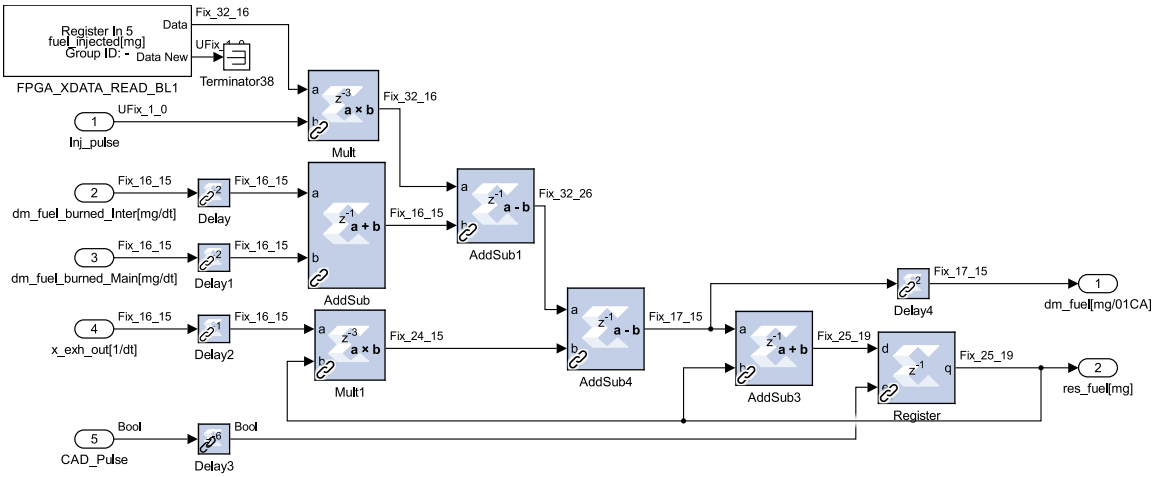

Figure 4.12: XSG block diagram for the calculation of residual fuel mass for implementation to FPGA.

Porting the model to the FPGA must take into account the limited number of gate arrays and RAM blocks. This requires that the model is kept as simple as possible to conserve available resources. A trade-off between gate array and RAM usage is often considered to determine if a complex calculation requiring many gates should be simplified to a 1D look-up table that requires more RAM. Specifically, the calculation of the piston speed, ν, required in equation 4.9, contains trigonometric functions which are difficult and resource intensive to implement using standard fixed point arithmetic. This was an example where a look-up table was used to conserve

gate array resources.

4.3.2 FPGA Delay Consideration

One major difference between a standard microprocessor based model such as the offline physical model and the model ported to the FPGA is that on the FPGA each calculation takes a fixed amount of time. As many calculations are occurring in parallel on the FPGA this can cause signals to become delayed and misaligned if the time for the signal to pass through each logic element is ignored. The amount of delay is dependent on the complexity of the calculation taking place, but at least one sample period (12.5 ns on the FPGA used in this study) occurs. This delay can be seen in the final step of Figure 4.1 where the mass signal must be delayed by three samples to match the delay caused by the multiplication of pressure and volume. This ensures that both signals being divided are correctly synchronized in time.

Figure 4.12 shows a more complex example of the XSG blocks used for the FPGA model. This example clearly shows the impact of the calculation delays and the required delays to ensure that the signals are synchronized at the end of the calculation. This example also shows a register at the end of the calculation which is used to keep the output value constant while the calculation is taking place or clocks the calculation. This ensures that the value of residual fuel mass is provided at each 0.1°CA step. This is required as the sample rate of the FPGA is higher than 0.1°CA and the measured input may change during the time step.

These examples are just two small components of the entire highly interdependent gas exchange process shown in Figure 4.5 it is possible to see the challenge of keeping track of all the calculation delays for the entire model. The delays caused by the FPGA calculation are one of the biggest changes from a processor based model. Fortunately, an offline simulation can be used to test the FPGA calculation and make sure appropriate delays have been added to the model to synchronize the calculation.

The individual delays of each operation on the FPGA can then be summed to determine the total calculation time. For the entire gas exchange process on the FPGA the calculation time is 282 samples or 3.5250 μs. Therefore, with the current FPGA model running at 0.1°CA an engine speed up to 4728 rpm is possible. If higher engine speeds are desired the calculations could be performed at a lower resolution. For example calculating at 0.2°CA would double the maximum engine speed. The impact from the reduction in resolution is small as shown in Figure 4.6.

4.3.3 Model Physics Reduction

To port the offline physical model to the FPGA capable model, simplification of a portion of the physics used in the offline model is used. The three main changes were: neglecting the gas dynamics of the air entering the cylinder, a simplification of the NASA polynomials for the gas properties and using the average piston speed.

As discussed in the offline model section, the inclusion of gas dynamics allows for a better match between the offline physical and reference models. However, the cylinder temperature and mass are very close between models and the inclusion of gas dynamics adds complexity to the FPGA model. Therefore, currently the gas dynamics are excluded from the FPGA model for simplicity and FPGA resource conservation.

The offline physical model calculates the gas properties using NASA polynomials using equation 4.12. To conserve resources and simplify the FPGA model, the gas properties were simplified to either constant values or a temperature dependent look-up table. To determine if a look-up table was necessary rather than a constant value, the values calculated in the physical model were examined. Values that have little variation over the range that they are used were set as a constant. For example, the intake and exhaust manifold temperatures do not vary significantly over a single valve event and therefore it was sufficient to leave them as constants. As the temperature in

the intake manifold remains constant so does the density, gas constant, and enthalpy of the charge entering the cylinder.

This simplification, however, can not be applied to the cylinder contents as the cylinder temperature changes over the exhaust event which changes the properties of the gas leaving the cylinder. Therefore, it was necessary to calculate the cylinder density, gas constant, and enthalpy using temperature dependent look-up tables.

The specific heat ratio, κ, is one gas property that has a significant impact on the calculated cylinder temperature. To get an acceptable value it was necessary to use the following second order polynomial [85]:

$$\kappa = 1.338 - 6.0 * 10^{-5} T_{cyl} + 1 * 10^{-8} T_{cyl}^2 \tag{4.24}$$

in which T_{cyl} is the calculated cylinder temperature. Using this equation allowed for a good approximation of the specific heat ratio without the need for a detailed look-up table and is arithmetically simpler to implement than the fourth order NASA polynomials. Equation 4.24 provides a good balance of the required accuracy and FPGA resource conservation.

The calculation of piston speed, equation 4.10, contains sinusoidal functions that are difficult and resource intensive to implement on the FPGA. To simplify the calculation by removing the complex functions the mean piston speed will be used:

$$\nu_{pis} = \frac{2 L_{stroke} n_{RPM}}{60} \tag{4.25}$$

Where L_{stroke} is the stroke length and n_{RPM} is the engine speed in revolutions per minute (RPM). This simplification introduces error especially at the point were the piston speed reaches zero around TDC and BDC as shown in Figure 4.13.

Simplifications made during the porting process for the FPGA online model are

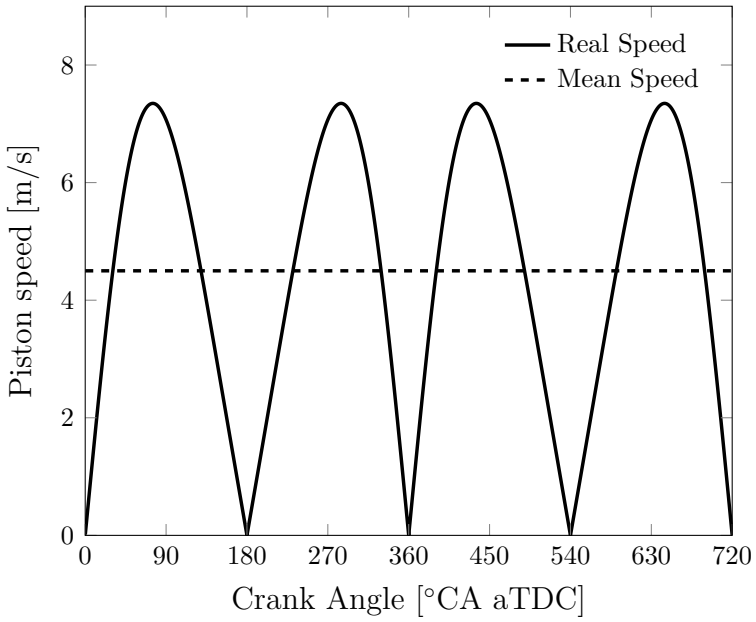

Figure 4.13: Comparison of real/mean piston speed calculation using equations 4.10/4.25.

summarized in Table 4.1.

4.3.4 FPGA Model Error Sources

The porting of the offline physical model to an FPGA capable model involves two main sources of error. They are the error resulting from switching to fixed point arithmetic over using floating point operations and the error caused by simplifying the physics in the model. Figure 4.14a shows the calculated constant volume specific heat capacity c_v at various temperatures. This figure shows the calculation using NASA polynomials and floating point arithmetic, simplified look-up table results using floating point arithmetic and finally the fixed point look-up table results. Here very little difference can be seen between the 3 calculation methods.

Figure 4.14b shows the error between the 3 calculations. Here the simple floating point model matches the NASA polynomials, however, the transition to fixed point arithmetic causes an increase in the error between calculations. Here the error between

Table 4.1: Included physical phenomenon in offline and FPGA models

Physical Process	Offline Model	FPGA Online Model
Energy conservation, eqn 4.6	Included	Included
Hohenberg wall heat model, eqn 4.9	Included	Included
Orifice flow, eqn 4.16	Included	Included
Gas dynamics	GT-Power corrected manifold pressure	Neglected
Injected fuel mass, eqn 4.20	Included	Included
Ratio of specific heats, γ	NASA polynomials	2nd order polynomial simplification [eqn 4.24]
Intake air properties	NASA polynomials	Assumed constant
Specific heat of cylinder gas	NASA polynomials	Temperature dependent look-up table
Energy of cylinder contents	NASA polynomials	Temperature dependent look-up table
Piston speed	Real speed [eqn 4.10]	Average speed [eqn 4.25]

FPGA model using the fixed point arithmetic and the NASA values used in the offline model are less than 1%. This value is acceptable as the model output changes very little for the additional resource cost of increasing binary size.

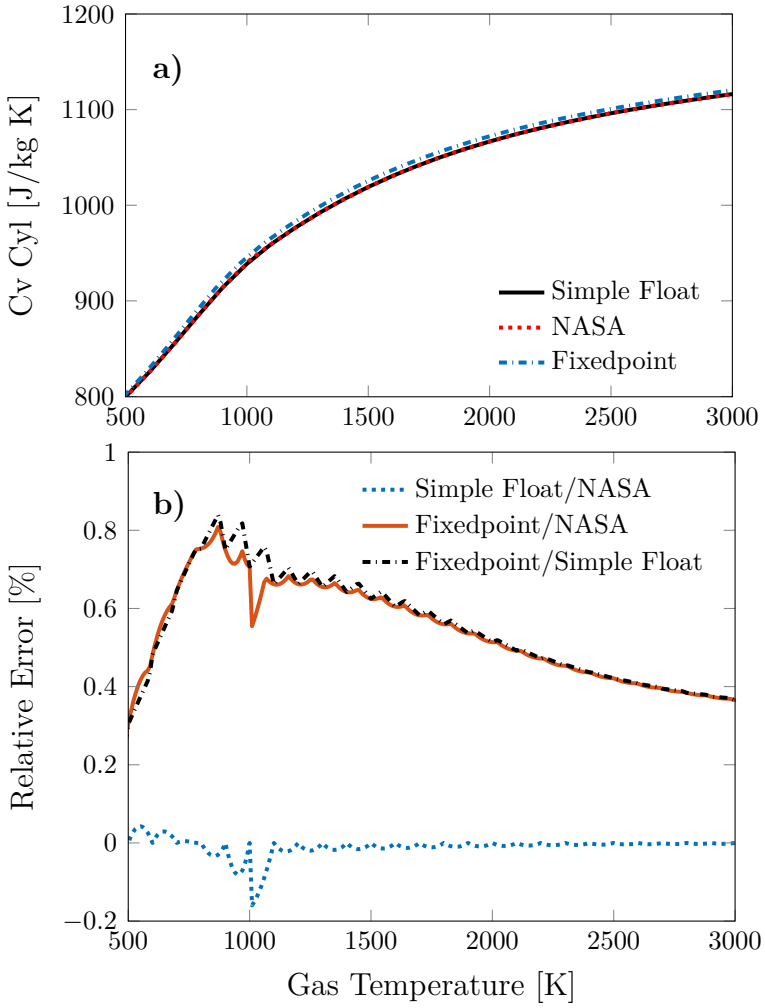

Figure 4.14: Error in constant volume specific heat capacity due to transition to FPGA capable model.

4.3.5 Offline FPGA Simulation

For offline simulation of the FPGA model, these small sections of the existing offline physical model were individually converted over to XSG blocks. Then using the offline physical model as input for offline simulation of the FPGA model, small sections

of the FPGA model can be optimized. The output of the FPGA model was then compared to the offline physical model results and adjustments to binary precision were made as necessary. Thus having a good offline physical model is essential to generate values that cannot be experimentally measured.

One challenge with running an offline FPGA simulation is the simulation time of 720° crank angle taking over 21 hours compared to under 5 seconds for the same cycle using the offline physical model (simulations are run on an Intel Core i7-6700K based PC). This means that simulations must be carefully planned and results saved at intermediate calculation steps to troubleshoot each step in the calculation after completion. The slow simulation is a consequence that each FPGA time step is simulated which is 12.5ns or 887 steps per 0.1°CA at an engine speed of 1500rpm used in this study.

After the small sections are individually tested in offline FPGA simulations they can be combined to build up the complete operation and then the complete model. As previously discussed the parallel processing of the FPGA presets a timing issue. When combining the small sections it is essential to ensure the correct accumulated delay of each model section. This is important so that values are updated at the same time and signals of different delay are not combined in future operations. After combining the smaller sections, another simulation is run and the results are compared to the offline physical model to check for errors caused by incompatible binary precision and timing problems.

4.3.6 Resource Utilization

The trade-off for the high computation speed of the FPGA is that hardware resources are limited for FPGA implementation. It is thus important to consider the resource utilization for model development. These resources are broken into six main categories as presented in Table 3.3. The similarity of calculations between the intake and

exhaust mass flows and the high calculation speed of the FPGA are combined to conserve resources. This is accomplished by switching the input values between intake and exhaust every sample (12.5 ns) and then passing that signal through the FPGA logic blocks to complete the mass flow calculation, then separating the two signals after the calculation as shown in Figure 4.15. This is only possible as the mass flow calculation on FPGA occurs much faster than the intake pressure changes at 0.1°CA. This is referred to as time division multiplexing (TDM) and allows the same hardware on the FPGA to be used for the calculation of the both mass flows.

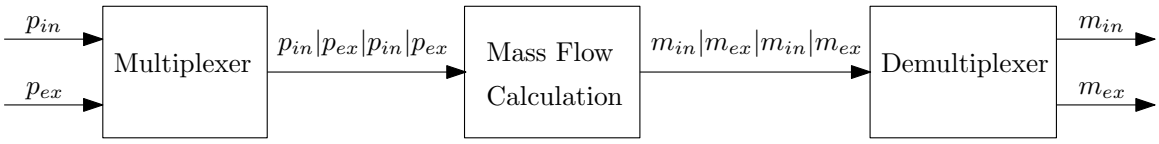

Figure 4.15: Process of time division multiplexing

The FPGA lookup tables resource usage from each of the main model sub-systems has been visualized in Figure 4.16. The resource savings made available by using TDM on the mass flow can be seen as large percentage of the total resources used in the gas exchange model. This figure is also useful in analyzing which model sub-system are utilizing resources. Here it can be seen that the gas exchange model is not using the most resources but the EMVT valve and injection controllers along with the angle calculation unit (ACU) and calculated pressure indication (CPI) utilize a significant portion of the resources. In addition, there still remains free resources that can be used for future controllers.

4.4 Results of Online FPGA Model

After verifying the offline FPGA simulation results were within 5% of the offline physical model, the FPGA model was compiled and flashed to the FPGA hardware for online testing and further tuning. The CAS system was set to output a timing

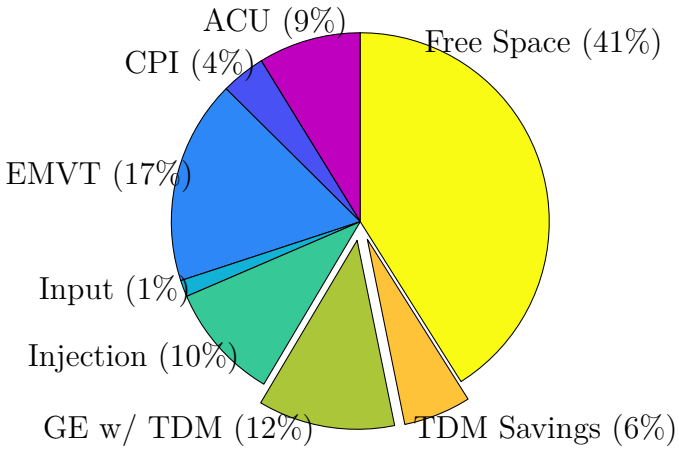

Figure 4.16: Lookup table resource utilization from current model sub-systems.

pulse at the start of recording which was then recorded on both the MABX and CAS systems. This timing pulse was used to align the online FPGA model with the identical CAS cycle. Having the CAS data cycle synchronized with the FPGA data ensures that the offline physical model calculates the same cycle to have results that capture the cyclic variability present in HCCI combustion.

The FPGA results presented in this section were calculated on the FPGA board and recorded on the processor side of the ECU. The extraction of values to the processor side was limited to a sampling rate of 0.5ms to prevent overruns. However, it should be noted that the FPGA is still calculating at 12.5ns, and this fast sampling rate can be used for FPGA based controllers.

The calculation of cylinder pressure using the online FPGA model is compared to the measured and offline physical model calculated pressures in Figure 4.17. The cylinder pressure matches well over the entire engine cycle. During the NVO recompression there is a slight difference of cylinder pressure between the models and the measured pressure. The cause of this pressure difference is attributed to blow-by due to poor sealing between the optical cylinder head and the piston sleeve. This pressure loss is not included in the model and can be seen by the over-prediction of cylinder

pressure during recompression. This error would be significantly lower for a metal cylinder head and is not seen as a deficiency with the model.

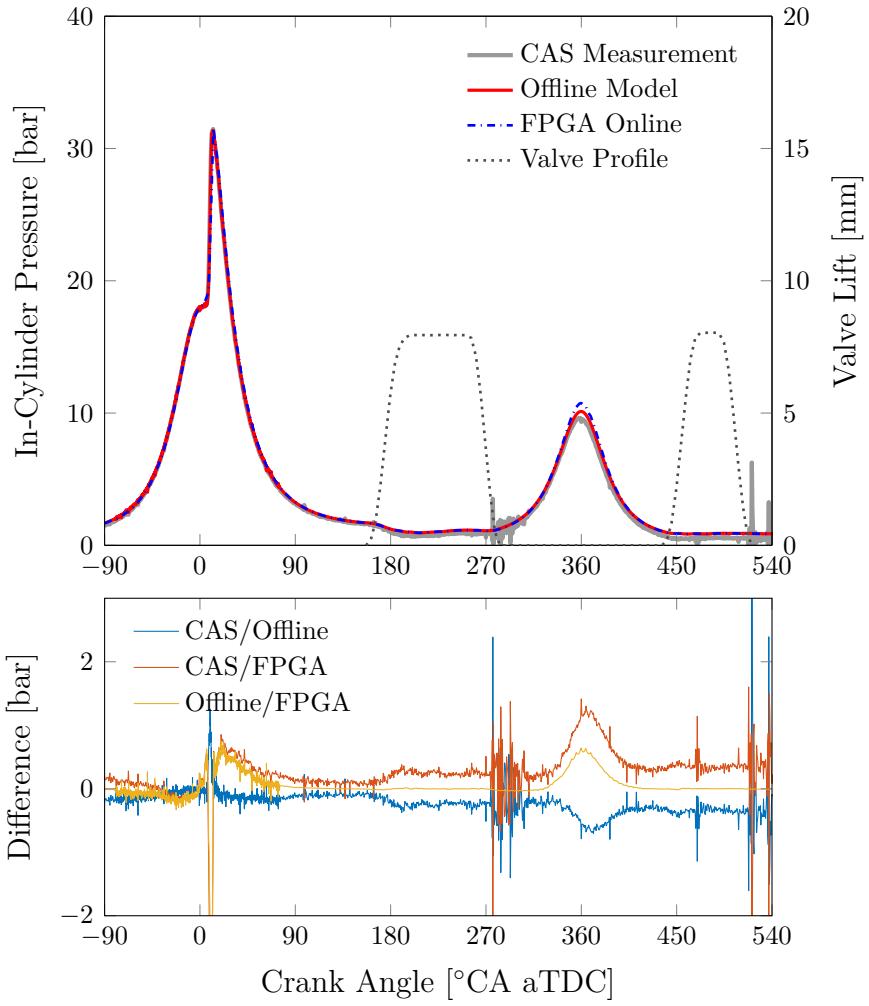

Figure 4.17: Comparison of measured in-cylinder pressure with calculated offline physical model and online FPGA models.

The calculation of the temperature gradient presented in equation 4.6 is used for the calculation of the cylinder temperature from the previous time step. Therefore, it is important that the online FPGA model matches the offline physical model. Figure 4.18 shows that both models match with only a very slight offset during NVO recompression. This offset is attributed to simplifications in the wall heat loss calculation in the FPGA model. This difference in the wall heat loss can better be

seen in Figure 4.19, where a clear difference of 0.009 $J/0.1°CA$ can be seen. This is due to the simplification of using the mean piston speed as given by equation 4.25 which does not capture the complete stop of the piston as it changes direction around TDC leading to differences in the wall heat loss around both combustion and GE TDC.

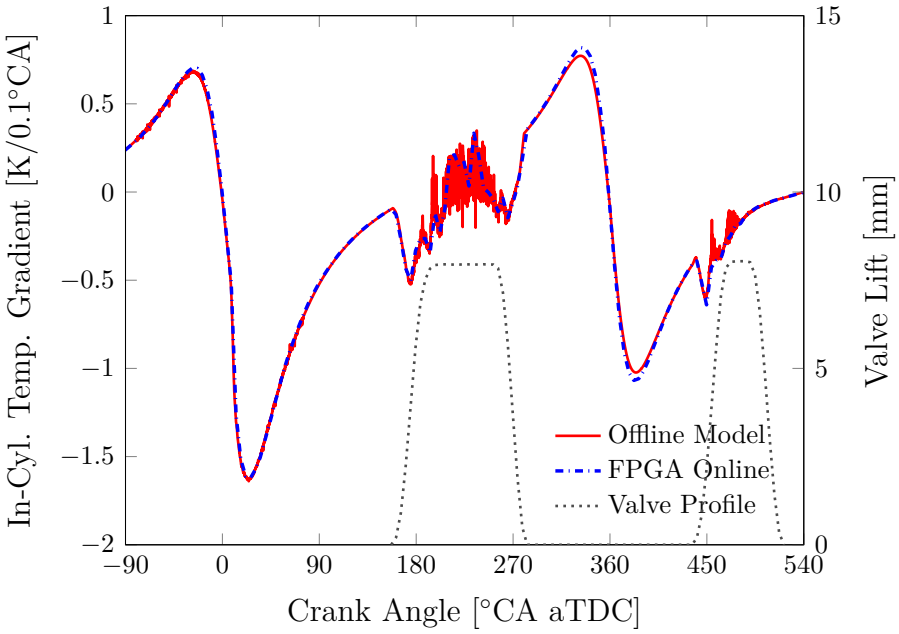

Figure 4.18: Comparison of temperature gradient calculated with offline physical model and online FPGA model.

As the temperature gradient closely matches the physical model, this leads to an accurate cylinder temperature calculation as shown in Figure 4.20. During the gas exchange process both models are very close. However, the temperatures calculated during the combustion phase show some difference. As explained above, during the combustion phase the cylinder temperature is calculated using the ideal gas law and not the first law of thermodynamics as it is during the gas exchange process. Therefore, the FPGA model only needs to calculate a temperature during combustion to use as an initialization value. The causal nature of the model means that the initialization value does not need to be exact and this opportunity was used to conserve

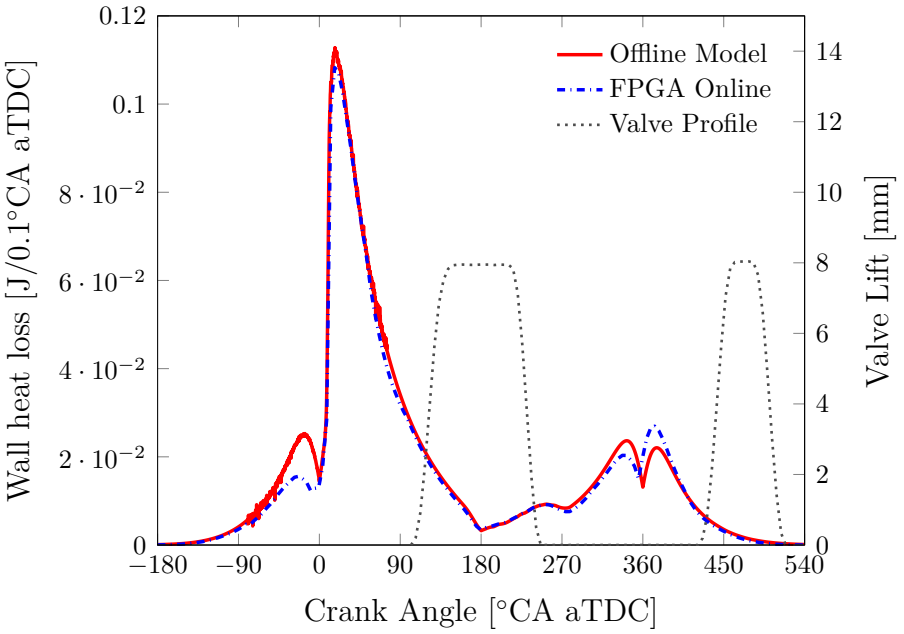

Figure 4.19: Comparison of wall heat loss calculated with offline physical model and online FPGA model.

FPGA resources. Figure 4.21 shows the air mass flow rate calculated on both models using equation 4.16. The flow rates are very similar with the main difference being that the FPGA model appearing smoother due to the limited sampling rate of the ECU processor as described above. As the mass flows of the models are very similar both models calculate a similar cylinder mass as shown in Figure 4.22.

4.4.1 Model Flexibility

A physics based model can handle a wide range of operating conditions compared to traditional simplified models for real-time application. This means that variations in engine speed, boost pressure and NVO can be handled by the model without the need to linearize the model at many operating points, i.e. engine mapping. This makes the physics based model capable of handling many operating points and also allows for disturbances to be accurately included in the calculation.

To test the models ability to handle various operating points: boost pressure,

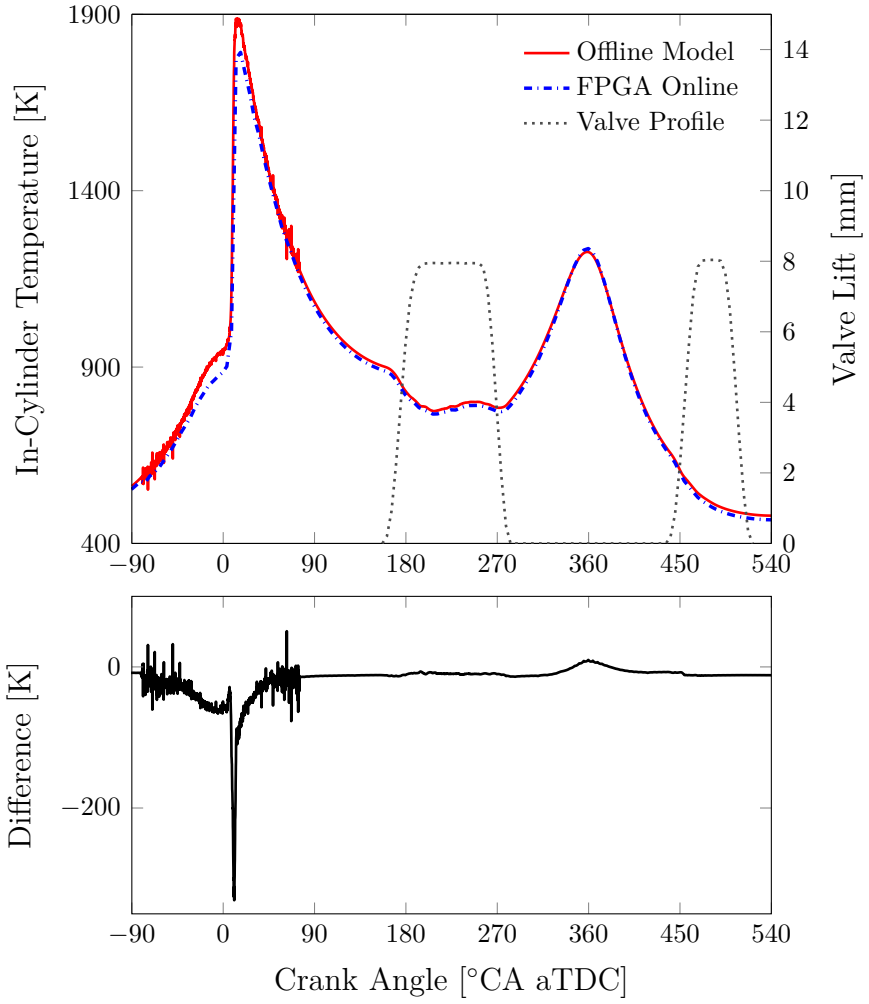

Figure 4.20: Comparison of temperature calculated with offline physical model and online FPGA model.

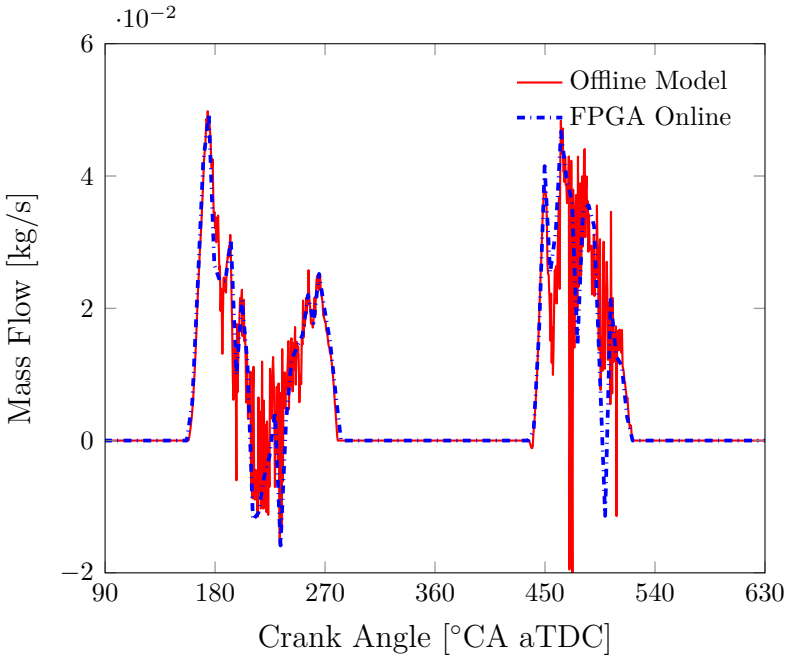

Figure 4.21: Comparison of cylinder mass flow calculated with offline physical model and online FPGA model.

NVO duration and engine speed are varied over a range of conditions. These changes represent operating condition variables for HCCI combustion timing that could be encountered in practical engine operation. Boost pressure can be used to increase the load operation range but can not be used for cycle-by-cycle control [86]. Since the SCRE is equipped with a fully variable EMVT, an NVO sweep can be achieved in various ways. In this study, the NVO was kept symmetric around the gas-exchange TDC. The EVO and IVC were fixed during this sweep while EVC and IVO were symmetrically varied, starting at the largest NVO. The third sweep was a variation of engine speed. Auto-ignition requires time for the chemical reactions to occur and increased engine speed reduces the time the cylinder contents spend at increased temperature and pressure. Variations in engine speed will occur in vehicle operation of HCCI combustion so it is important that the model is able to handle this change in conditions. The chosen operating points of these three sweeps are presented in Table 4.2.

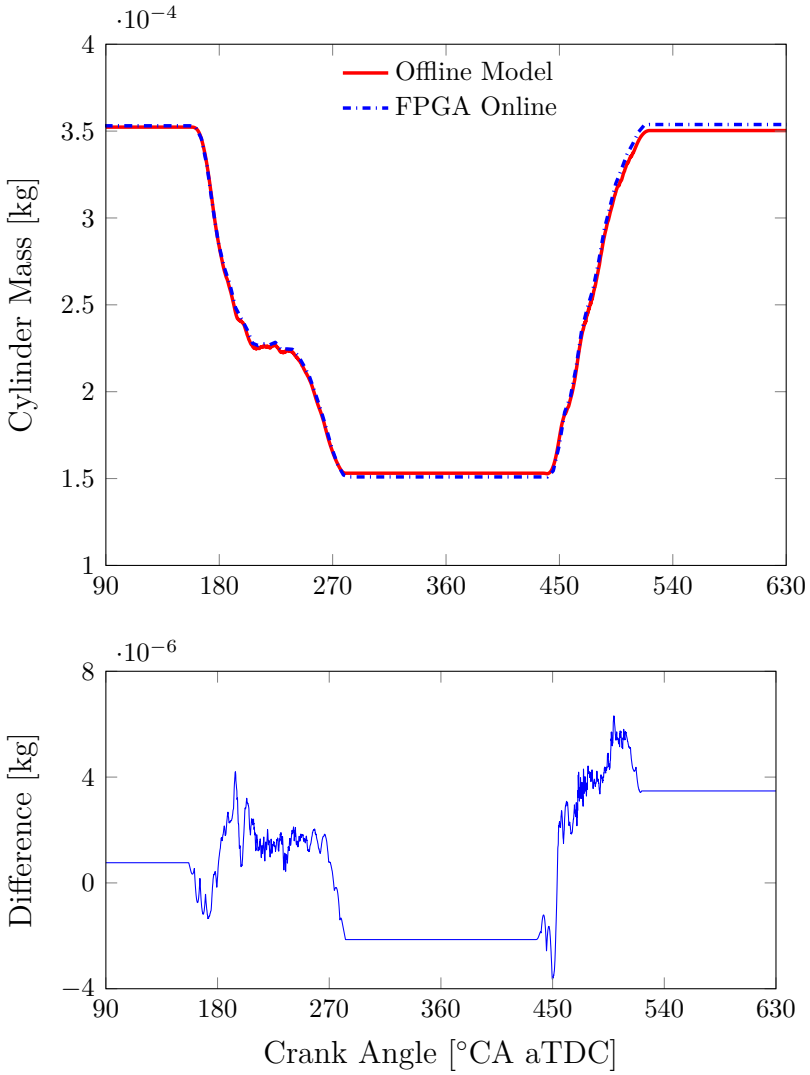

Figure 4.22: Comparison of trapped cylinder mass calculated with offline physical model and online FPGA model.

To compare the offline and FPGA model at the various operating points, the fresh air ratio was derived from the continuous mass calculation. This is the ratio of the fresh air entering the combustion chamber during the intake event to the total cylinder mass, r_{fr}, which is defined as:

$$r_{fr} = \frac{m_{fresh\ air}}{m_{total}} = \frac{m_{IVC} - m_{IVO}}{m_{IVC}} \tag{4.26}$$

The fresh air ratio for a variety of NVO durations for 50 cycles is shown in Figure 4.23. Here the FPGA model is able to follow the trend of the offline physical model capturing the cyclic variance in the fresh air ratio which has an effect on HCCI combustion timing. As both models are physics based, they both capture the change in NVO duration.

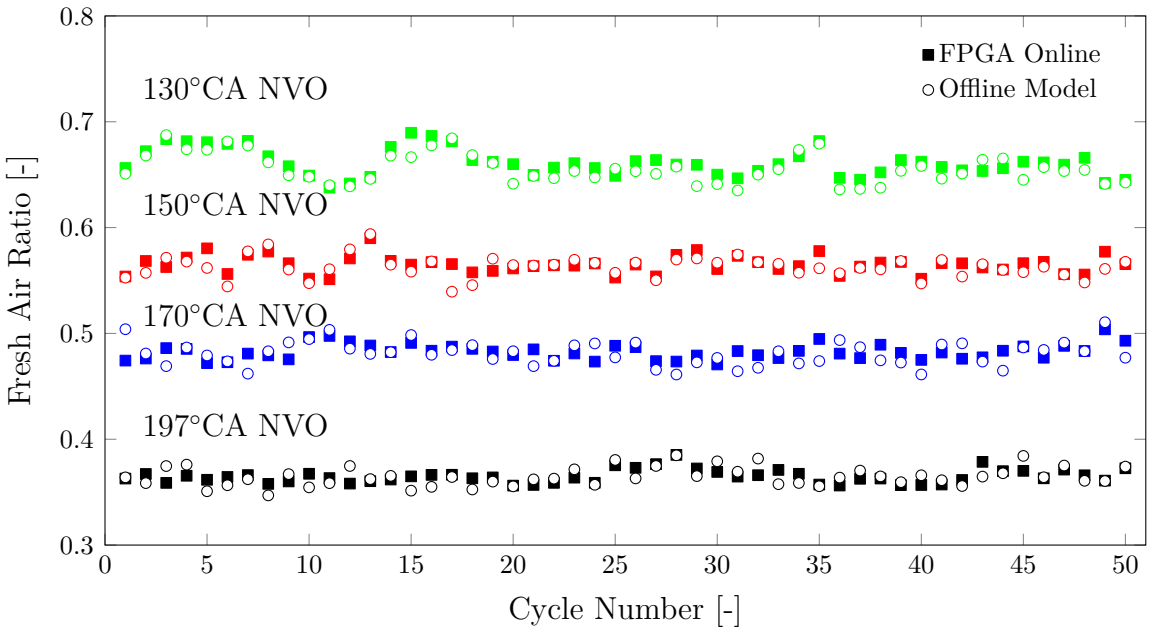

Figure 4.23: Fresh air ratio comparison for various NVO durations. Note that with increasing fresh air ratio the IMEP increases

To obtain a measure for the FPGA model accuracy, a relative error is defined as the percentual difference between FPGA and offline models of the fresh air ratio.

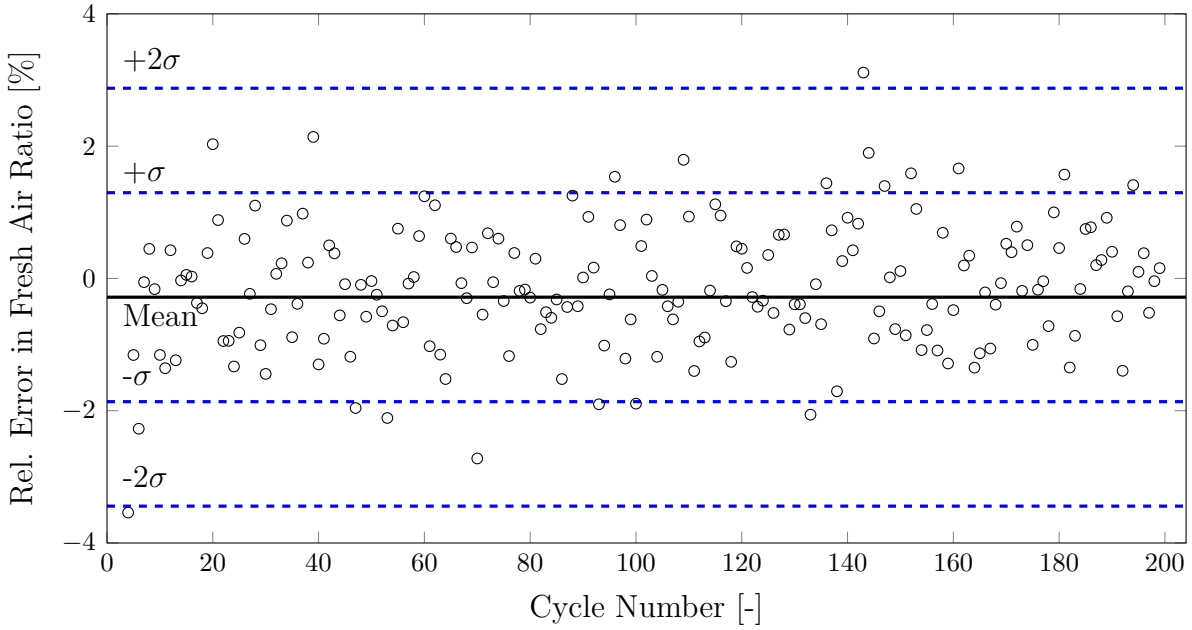

Figure 4.24: Percent difference in fresh air ratio between models for NVO duration of 170°CA

Figure 4.24 shows the relative error for each cycle as well as the mean error and standard deviation, σ, over the 200 cycles for a specific measurement point. The relative error for all 200 cycles remains below 4% in this operating point. These values along with the maximum error over all 200 cycles for all 12 measurements have been listed in Table 4.2. As can be seen, the mean error fluctuates around zero for all measurements showing that there is not a bias in the model to over or under predict the fresh air ratio when compared to the offline physical model. The standard deviation σ, which gives information on the amount of variation of the individual points in the entire measurement, reaches a maximum of 1.70% during all three sweeps. This indicates that the relative errors are close to the mean, and that the FPGA model works well over a variety of operating points. A maximum error of 4.40% over all 12 measurements indicates that the FPGA model achieves a good match to the offline physical model.

Table 4.2: Difference between FPGA and offline physical model represented by mean error and standard deviation for calculated fresh air ratio for variations in engine speed, NVO and boost variations. Note: *Italics* represent manipulated variable for each sweep

RPM [1/min]	NVO [°CA]	Boost [mbar]	IMEP [bar]	Mean Error [%]	Std σ Error [%]	Max Error [%]
1000	170	1013	2.94	-0.19	0.53	2.71
1250	170	1013	2.92	-0.22	0.59	3.13
1500	170	1013	2.64	-0.23	1.41	3.73
1700	170	1013	2.57	-0.34	1.43	2.31
1500	*197*	1013	2.04	-0.28	1.34	3.54
1500	*170*	1013	2.64	-0.23	1.41	3.73
1500	*150*	1013	2.77	-0.42	1.70	3.42
1500	*130*	1013	3.26	-0.35	1.27	2.30
1500	164	*967*	2.19	-0.20	1.24	4.05
1500	164	*1110*	2.63	-0.081	1.02	3.50
1500	164	*1200*	2.63	+0.16	1.22	4.40
1500	164	*1300*	2.79	-0.004	1.24	3.50

Chapter 5

Operating Region Variation

To begin control design it is important to understand the impact of the various control actuators on the HCCI combustion metrics (defined in Section 2.1.1). Not only to determine the ideal operating point but to also understand the limits of operation range. The HCCI operation domain is constrained by 3 main limits. First high pressure rise rates and engine knock, $dP/d\theta > 7$ bar/deg lead to engine damage if sustained. Second, extremely early combustion phasing, $CA50$, leads to inefficient combustion. Third, late $CA50$ leads to misfire and unstable combustion. To maximize the load and efficiency it is necessary to operate the engine at these boundaries. Therefore, understanding and modeling the engine at these boundary conditions is valuable.

First the effect of varying NVO duration on steady state engine operation was evaluated. This was followed by water injection sweeps including start of injection and injected water mass. Finally, the effect of water injection transferring between cycles was investigated to determine how long the actuation has an effect on the HCCI combustion or how many cycles are affected by the water injection. This test is important in determining if the controller interaction from previous cycles needs to be incorporated into the water injection controller. For these variations some parameters are kept constant to reduce the number of influencing factors on the

HCCI combustion. The parameters kept constant include engine speed at 1500 rpm, start of the fuel injection is kept at IVO, intake and exhaust pressure at 1013 mbar and coolant and oil temperatures.

5.1 NVO Variation

The NVO duration directly influences the amount of trapped residual gas in the cylinder. Increasing NVO duration results in more exhaust gas trapped in the cylinder and increasing the exhaust gas fraction. Exhaust gas fraction is also reduced as the NVO duration is decreased.

To change the amount of trapped residual gas in the cylinder the negative valve overlap was varied symmetrically. The exhaust valve opening and the intake valve closing were fixed and the exhaust valve closing and intake valve opening were varied symmetrically around gas exchange TDC. This EGR strategy has some benefits over for example intake or exhaust port recirculation. The first benefit is the pumping and heat losses of pushing the exhaust out of the cylinder and then drawing it back in are eliminated. Secondly, by keeping the valves closed around TDC would allow for smaller valve pockets as the valves would not contact the piston in a future production engines. This allows for an increased compression ratio and subsequently increased efficiency.

For all the tests reported the exhaust valve was opened at 160° CA aTDC or 20° CA before bottom dead center (BDC) to allow the cylinder pressure to equalize with exhaust manifold to prevent recompressing the exhaust gas. The intake valve closing was fixed at 545° CA aTDC or shortly after BDC to capture the momentum of the air entering the cylinder before the compression stroke called the ram-air effect. This helps maximize the amount of trapped air and subsequently the effective compression ratio of the engine.

The NVO variations were performed at four load points of 2.5, 3.0, 3.5 and 4.0 bar IMEP. During the NVO variations the fueling rate was adjusted to keep IMEP constant. The steady state engine operation is evaluated by the combustion metrics standard deviation of IMEP, pressure rise rate, lambda, CA50, burn duration, EGR, exhaust temperature, and emission levels as shown in Figures 5.1 to 5.9.

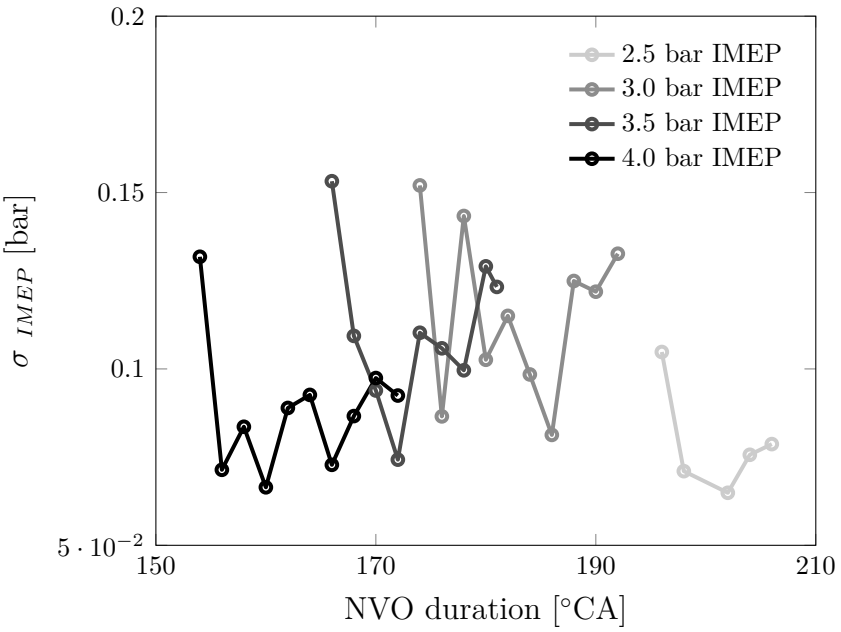

Figure 5.1: NVO variation impact on IMEP.

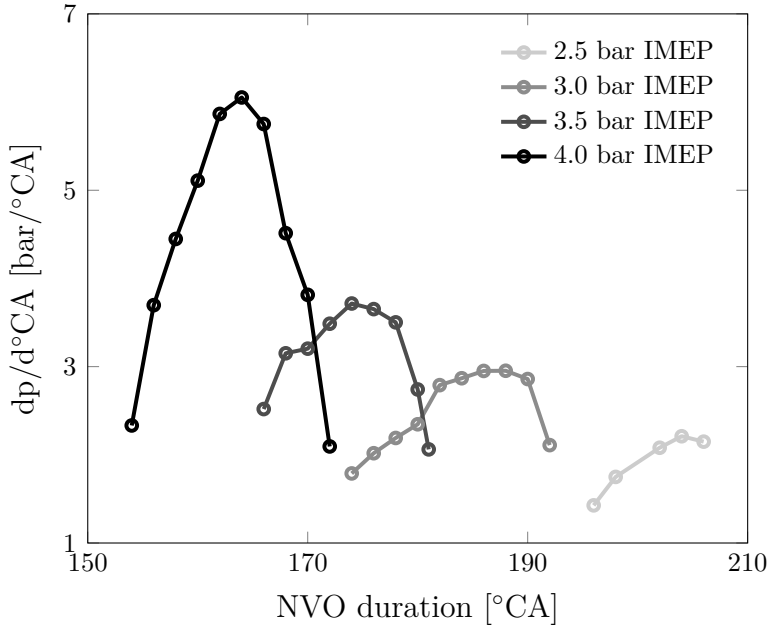

Figure 5.2: NVO variation impact on pressure rise rate.

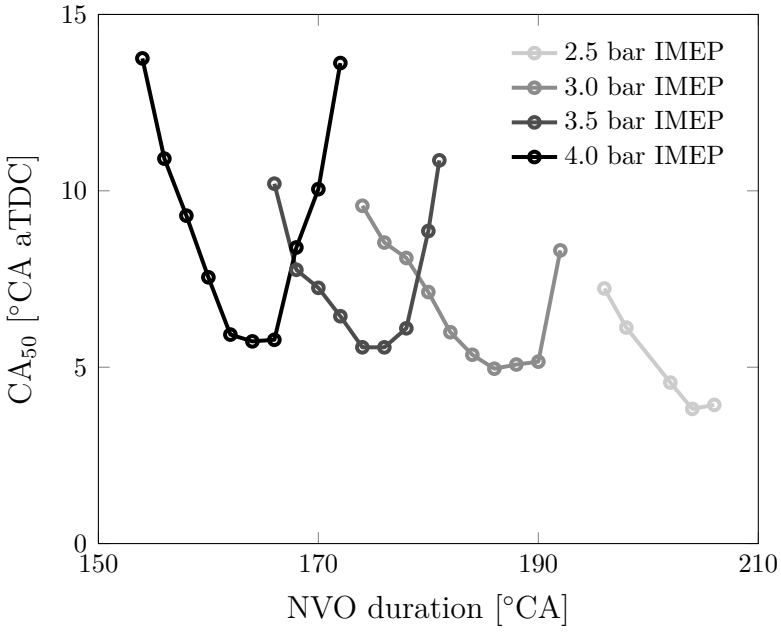

Figure 5.3: NVO variation impact on CA_{50}.

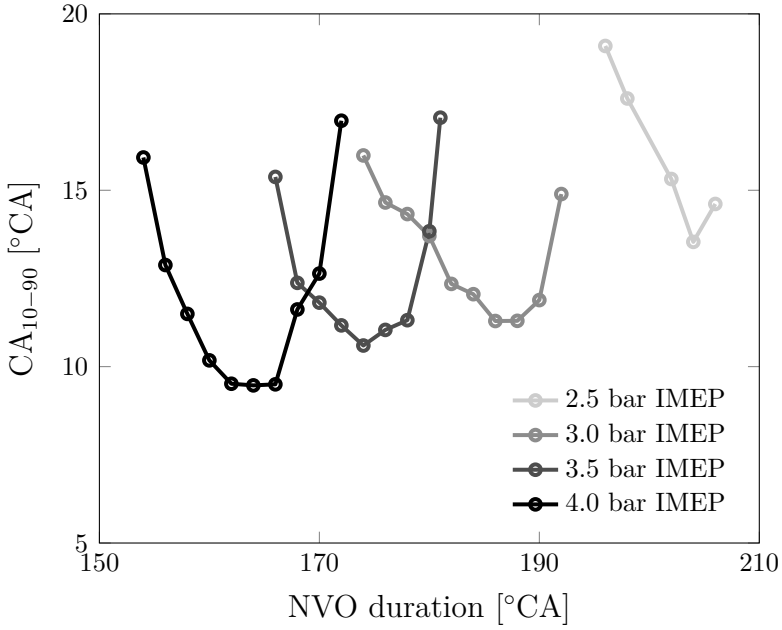

Figure 5.4: NVO variation impact on burn duration.

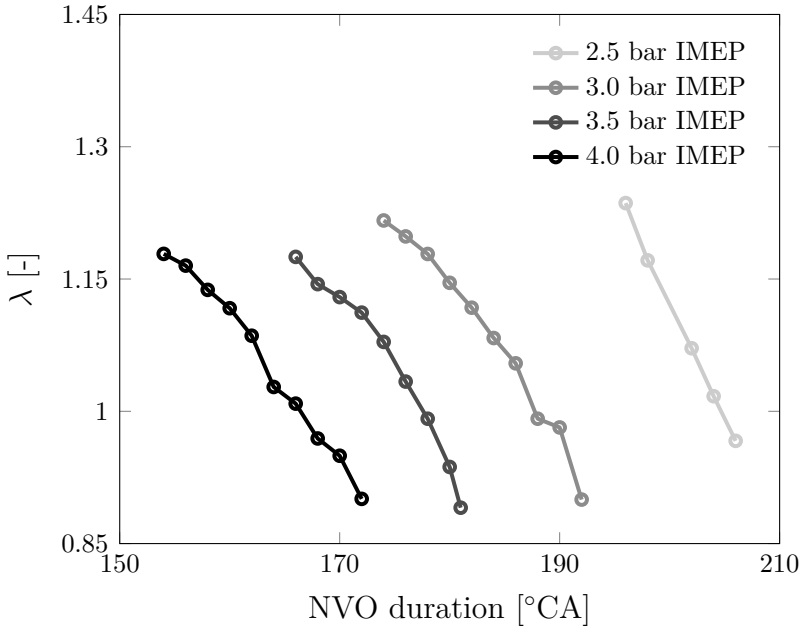

Figure 5.5: NVO variation impact on lambda.

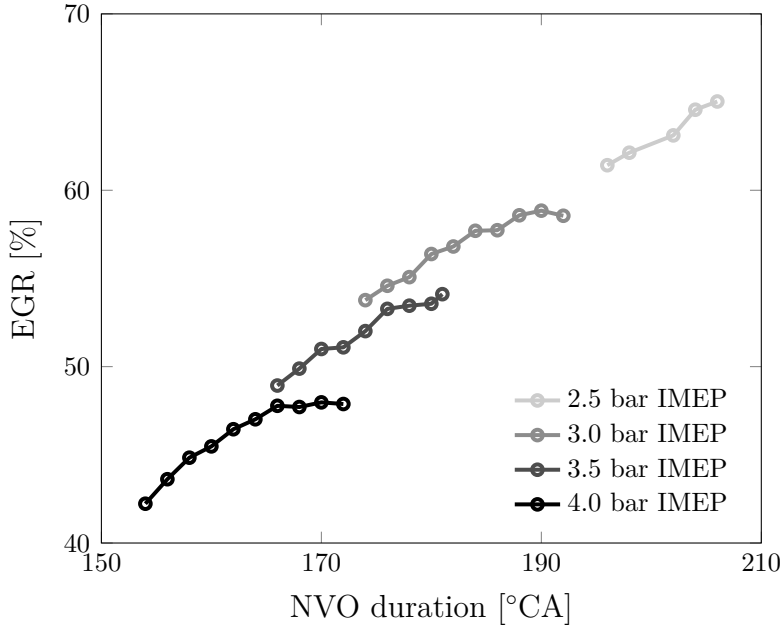

Figure 5.6: NVO variation impact on EGR rate.

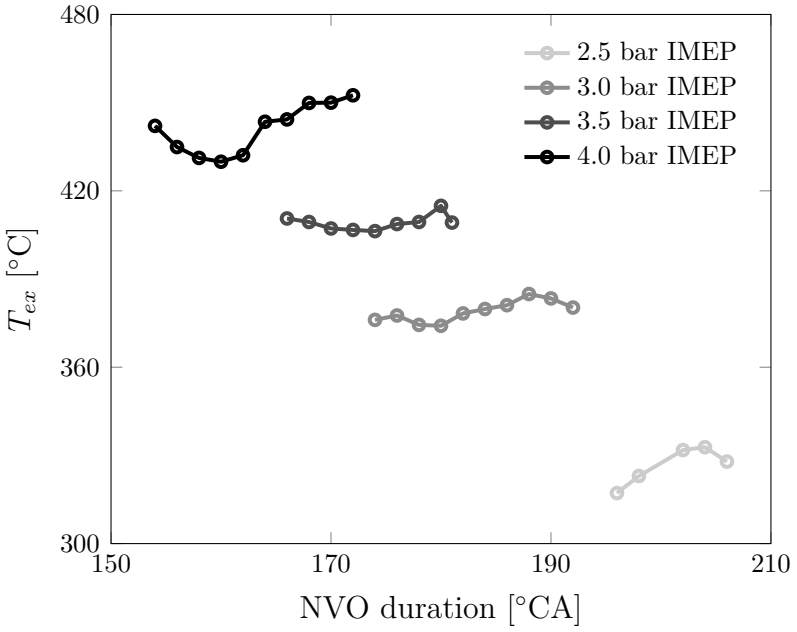

Figure 5.7: NVO variation impact on exhaust temperature.

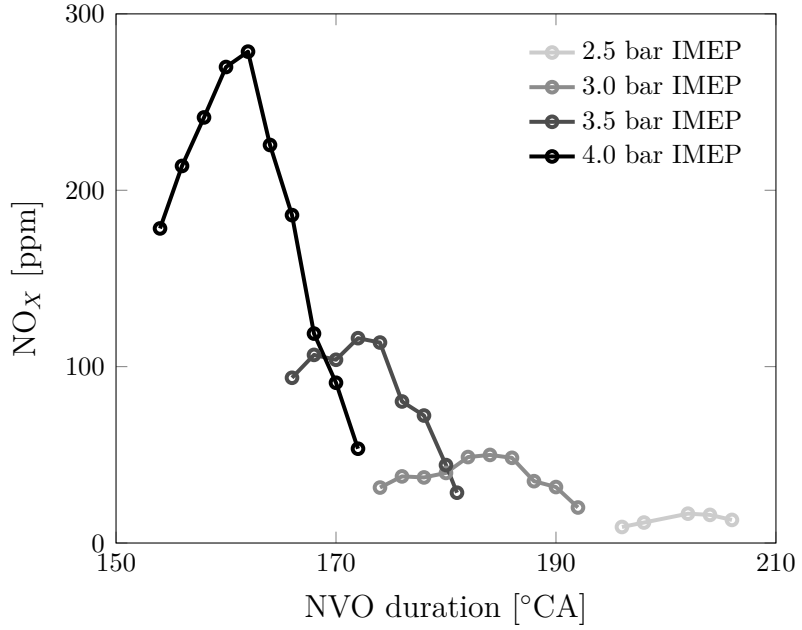

Figure 5.8: NVO variation impact on NO_X emission level.

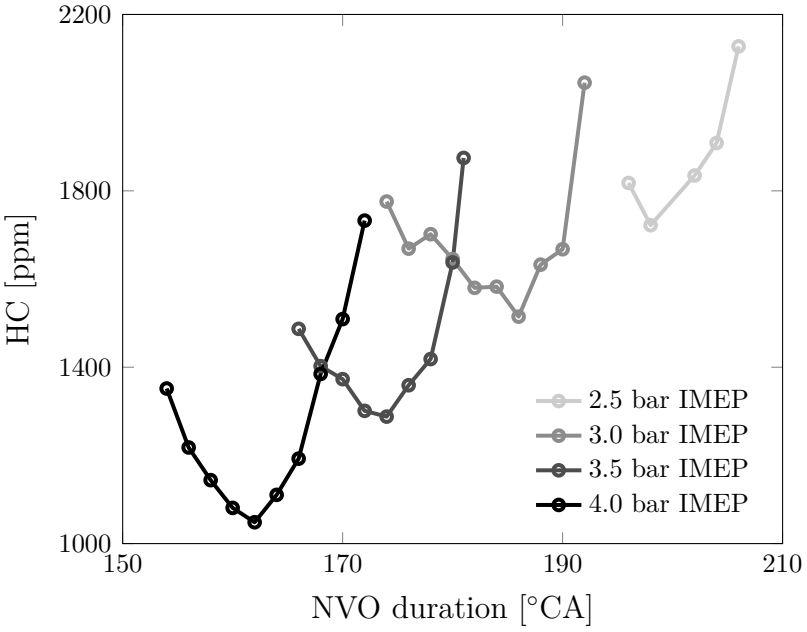

Figure 5.9: NVO variation impact on unburnt hydro-carbon emission level.

For the four loads tested a similar trend can be observed in all of the combustion metrics with just a shift in the required NVO duration. This shows that independent

of load the same combustion characteristics can be expected. At low NVO durations the amount of trapped residual gas is low and more fresh air is brought into the cylinder at a constant intake pressure. This results in highly diluted charge which reduces the cylinder temperature leading to late combustion phasing with long burn durations and low pressure rise rates. However, this also leads to an decrease in combustion stability as shown by the increase in the standard deviation of IMEP in Figure 5.1. At low NVO durations the lean engine operation leads to reduced NO_X emissions (Figure 5.8) but increased HC emissions (Figure 5.9) which is expected as the classical emissions trade-off [11].

As the NVO duration is increased towards stoichiometric operation, $\lambda = 1$, the combustion phasing is advanced leading to shorter burn durations (Figure 5.4) and higher pressure rise rates (Figure 5.2). This increase in NVO duration leads to an increase in combustion stability as more hot exhaust gas is trapped in the cylinder which helps to ensure that the cylinder temperature reaches the auto-ignition point of the fuel-air mixture. As the NVO duration is further increased the combustion becomes rich leading to a decrease in combustion phasing and pressure rise rate like lean operation. However, rich operation is undesirable as the increased fuel leads to a significant increase in HC emissions and a reduction of thermal efficiency.

To keep pressure rise rates and NO_X emissions low, lean operation with a short NVO duration is desired. Although, the decrease in combustion stability at these lean operating points is undesirable.

5.2 Steady State Water Injection

To evaluate the influence of water injection timing the start of injection (SOI) of water was varied between 270 and 720° CA aTDC. During this variation, the water injection pressure relative to the cylinder pressure at time of injection, $p_{inj} - p_{cyl}$, was

kept constant at 50 bar. By keeping the relative water pressure constant ensure that the water injection mass does not decrease as the injection timing is retarded to points where there is a higher cylinder pressure. The 50 bar pressure was chosen as it was high enough to ensure water evaporation but also low enough to keep the injected amounts low. The amount of injected water was kept constant at 2.3 mg, which represents the smallest possible injection duration capable with the tested injector. The impact of varying the start of water injection on the various combustion metrics is shown in Figures 5.10 - 5.18 and compared to a baseline operation without water injection.

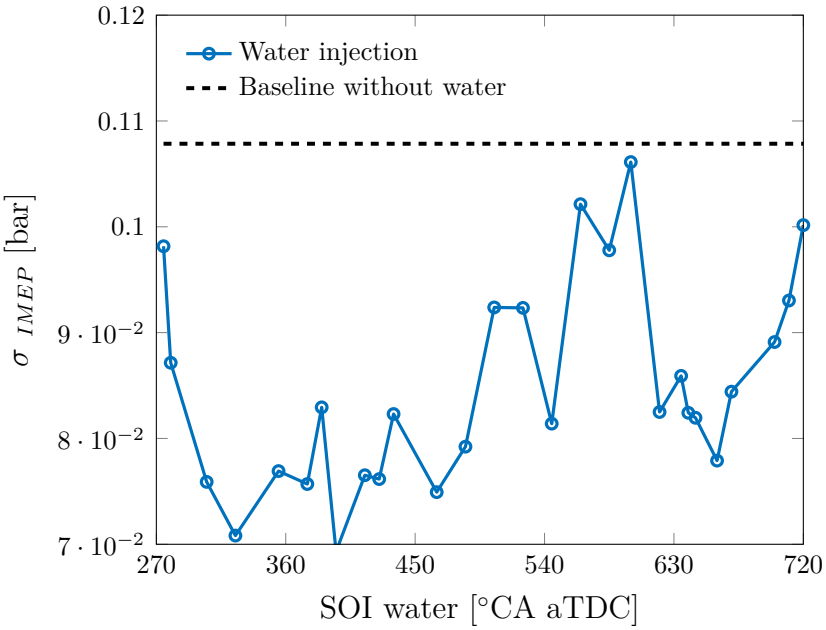

Figure 5.10: Water injection timing impact on IMEP.

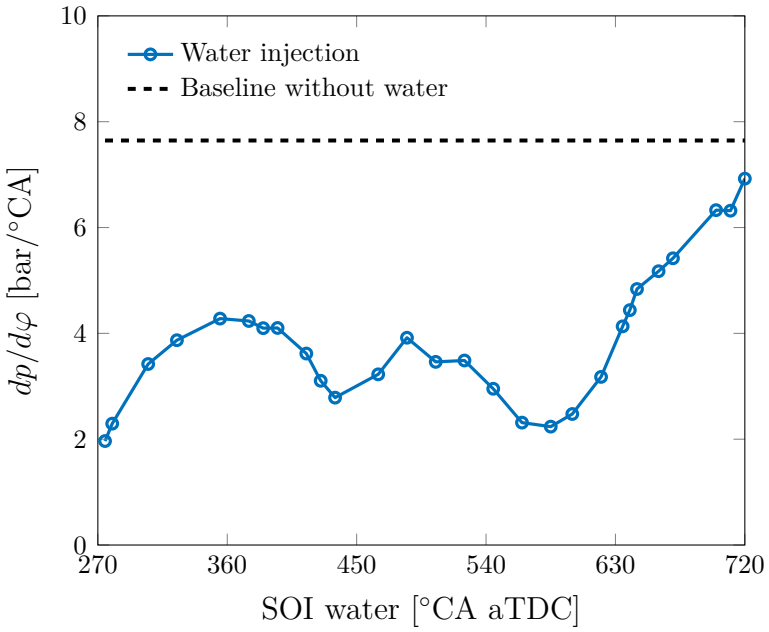

Figure 5.11: Water injection timing impact on pressure rise rate.

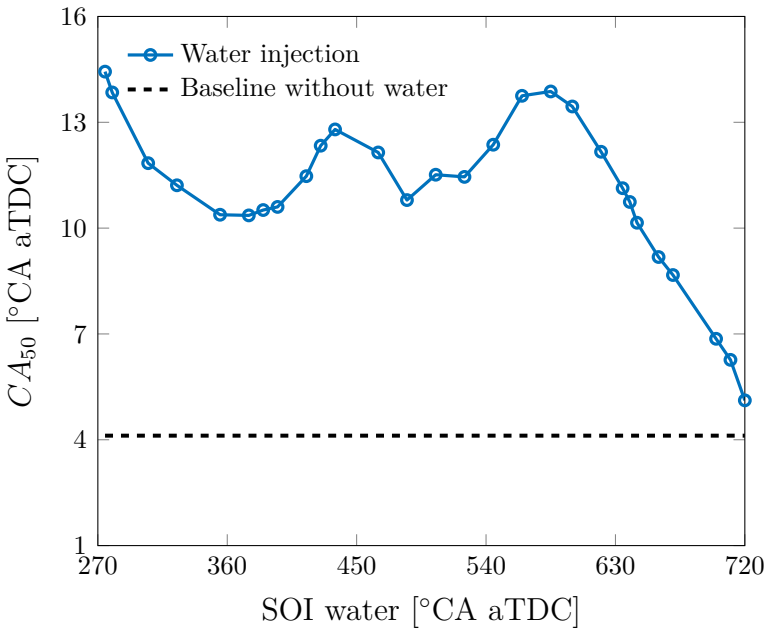

Figure 5.12: Water injection timing impact on CA_{50}.

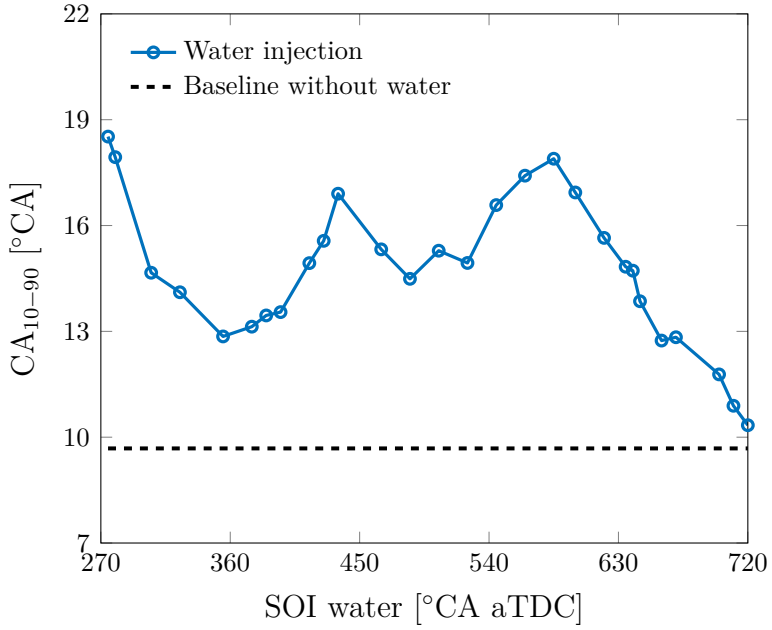

Figure 5.13: Water injection timing impact on burn duration.

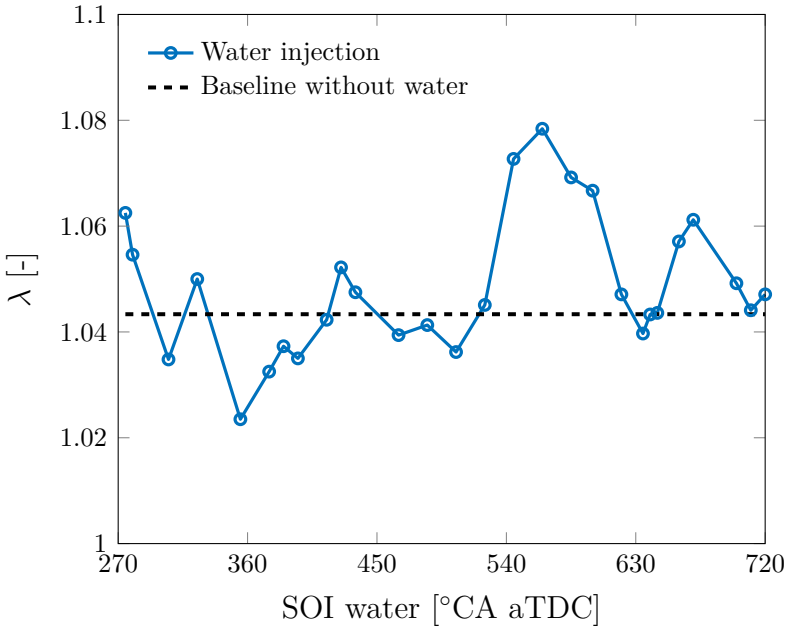

Figure 5.14: Water injection timing impact on lambda.

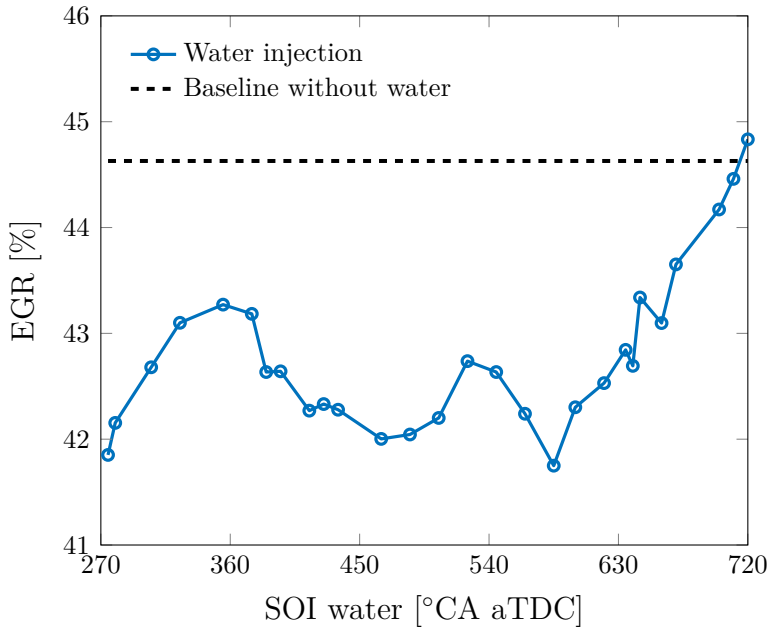

Figure 5.15: Water injection timing impact on EGR rate.

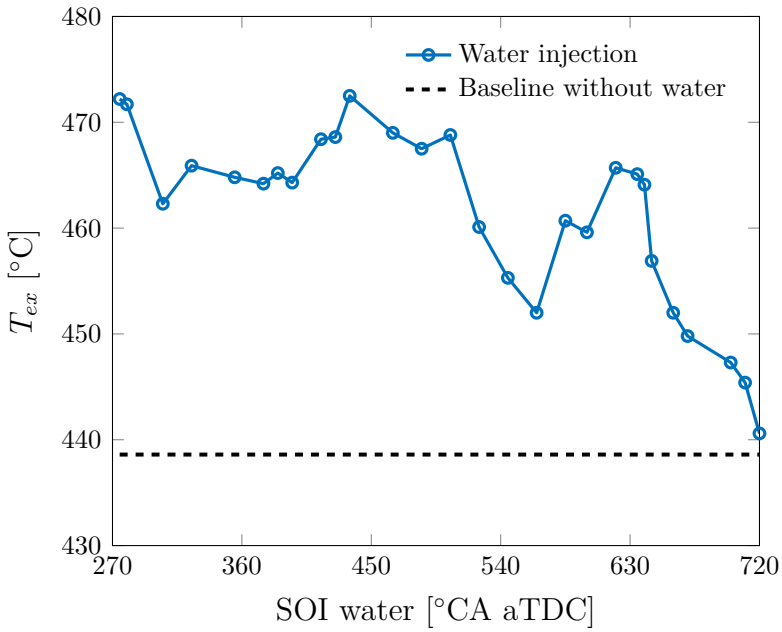

Figure 5.16: Water injection timing impact on exhaust temperature.

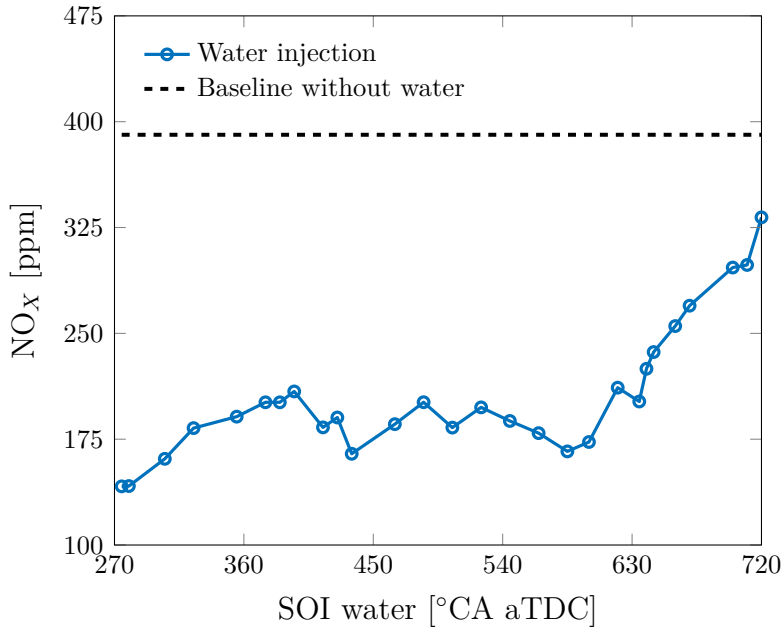

Figure 5.17: Water injection timing impact on NO_X emission level.

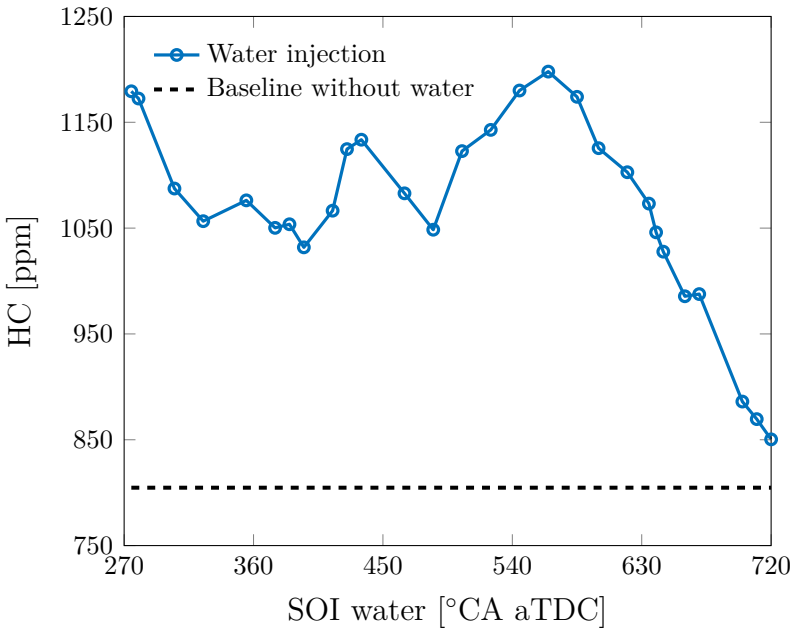

Figure 5.18: Water injection timing impact on unburnt hydro-carbon emission level.

Examining the water injection timing variation in Figures 5.10 to 5.18 some distinct trends can be seen in various ranges of the combustion cycle. When the water is

injected early in the NVO phase (270° CA aTDC) or early in the main compression phase (580° CA aTDC) a significant delay in combustion phasing from 4 ° CA aTDC without water injection to 14° CA aTDC can be seen. This retarding of the combustion phasing leads to a significant reduction in maximum pressure rise gradient from 8 bar/° CA to 2 bar/° CA which is the desired impact of direct water injection.

Figures 5.10 to 5.18 shows that as the injection timing is delayed towards both gas exchange and combustion TDC the impact of the water injection is reduced as all combustion metrics approach the engine operation without water injection. One possible reason for the decrease in the impact of the water injection is piston impingement. This is where the water injection occurs when the piston is close to the injector and the water pools on the piston instead of evaporating to cool the cylinder charge. The water does not have time to evaporate to lower the cylinder temperature before the combustion pre-reactions begin occurring and therefore does not affect the current combustion event. This effect has a smaller impact early injections during the NVO phase as the water on the piston still has time to evaporate during the main compression.

During the main compression (580 - 720° CA aTDC), as the injection timing is moved towards TDC the water does not have time to evaporate to lower the cylinder temperature before the pre-reactions begin occurring. This effect can very clearly be seen as the injection timing is moved to TDC where the combustion has already begun and therefor the water injection has very little impact on all the combustion metrics when compared with the baseline operation without water injection.

The expected relationship between combustion phasing and pressure gradient can be seen where the point with a late combustion phasing is also the point of low pressure rise gradient. For controller development, it is desired to have the injection timing that can retard the combustion phasing and lower the pressure rise rates the most while reducing the amount of water needed. There are two points that meet

this requirement and are water injection at 270° CA and 580° CA aTDC.

These two injection timings, along with a third timing later in the compression phase at 680° CA aTDC, are examined next to determine the sensitivity of combustion timing to the injected water mass. A steady state variation of duration of injection (DOI), the amount of injected water, was performed and is shown in Figures 5.19 to 5.27.

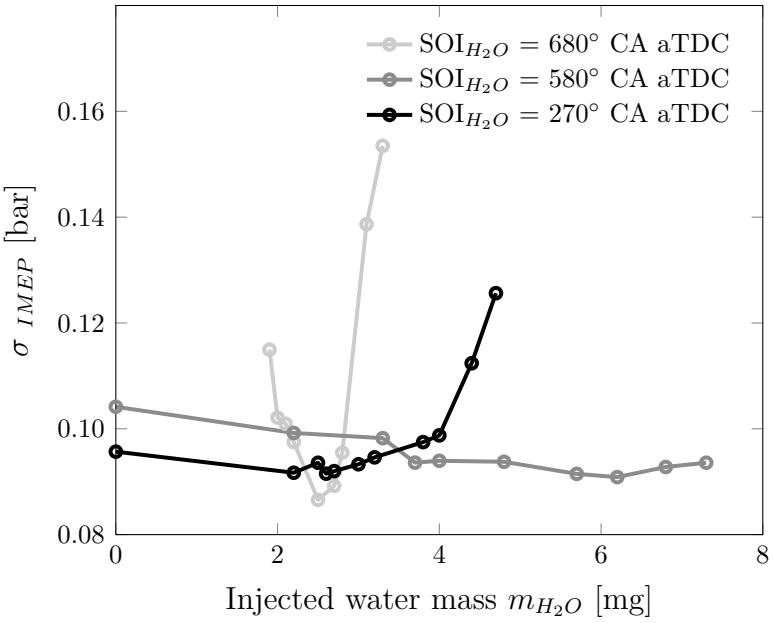

Figure 5.19: Impact of mass of injected water on IMEP.

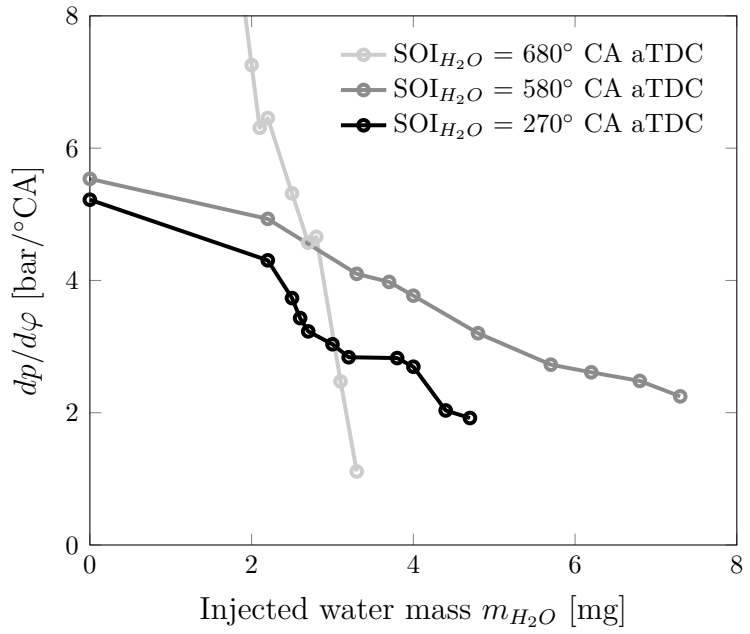

Figure 5.20: Impact of mass of injected water on pressure rise rate.

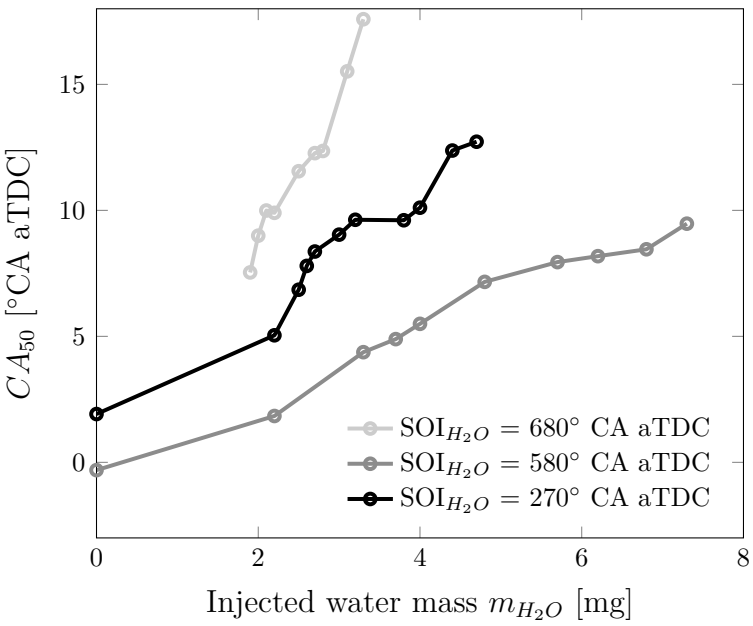

Figure 5.21: Impact of mass of injected water on CA_{50}.

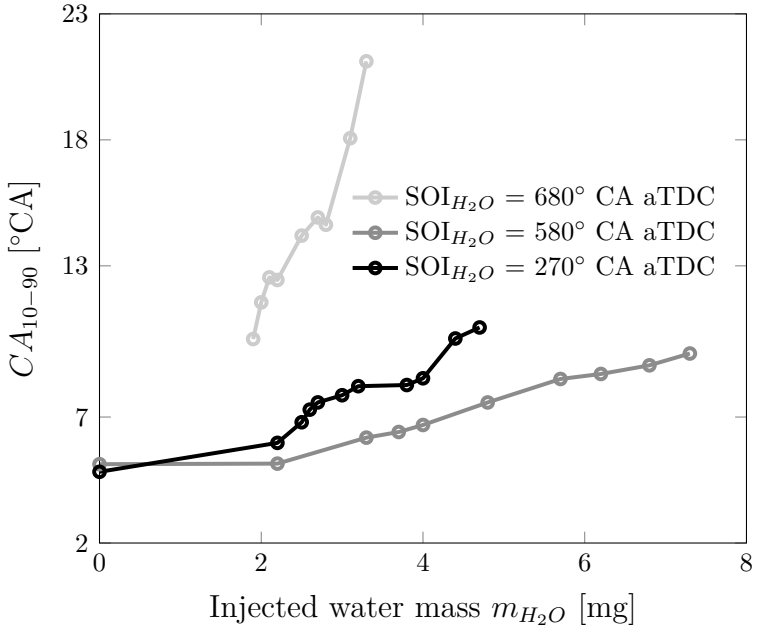

Figure 5.22: Impact of mass of injected water on burn duration.

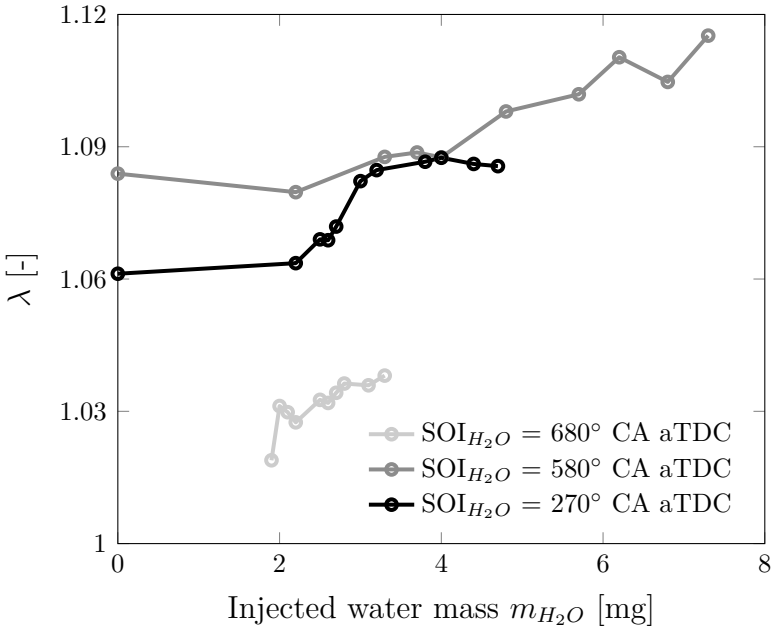

Figure 5.23: Impact of mass of injected water on lambda.

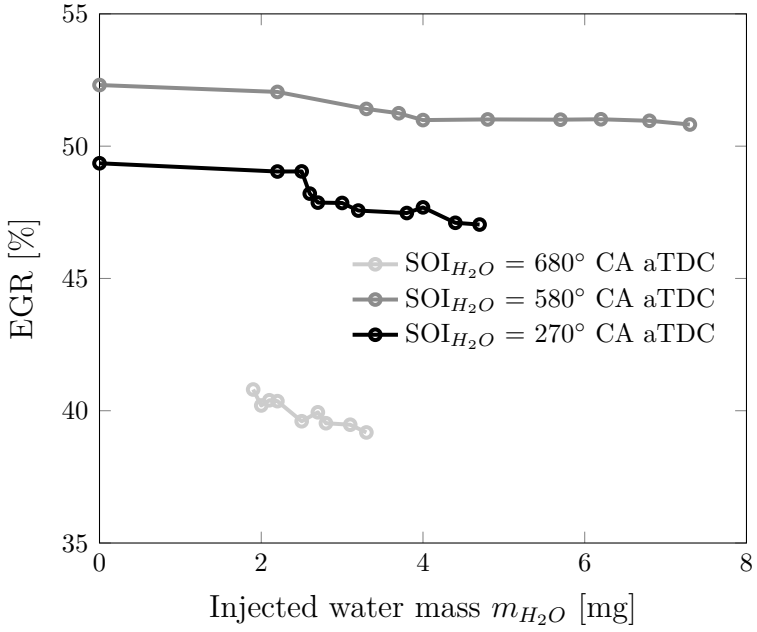

Figure 5.24: Impact of mass of injected water on EGR rate.

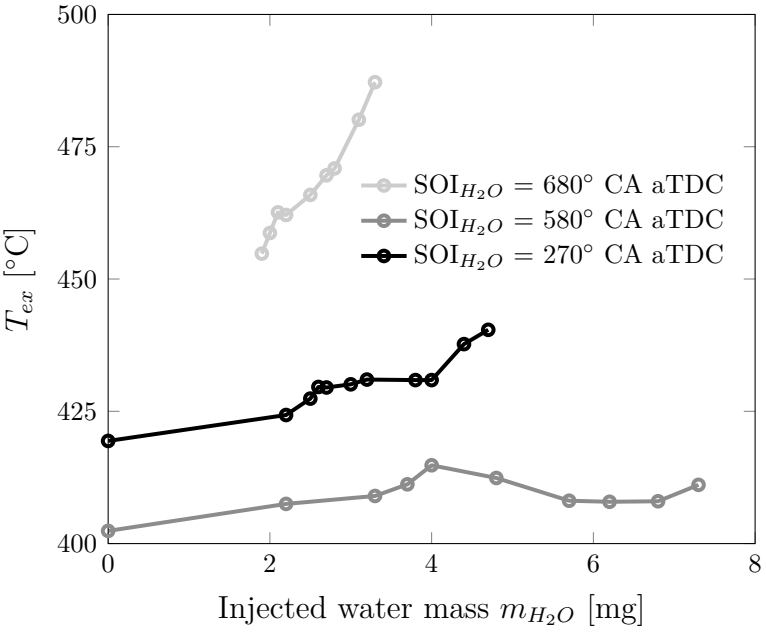

Figure 5.25: Impact of mass of injected water on exhaust temperature.

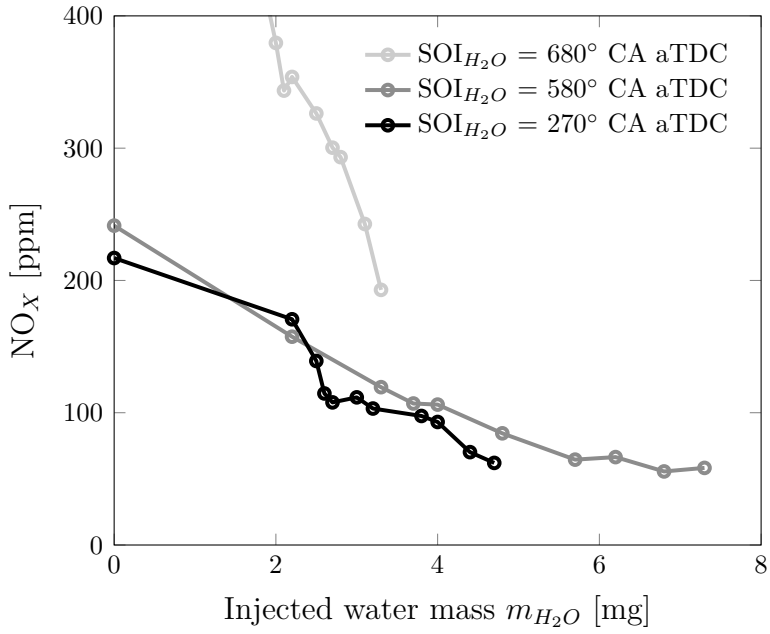

Figure 5.26: Impact of mass of injected water on NO_X emission level.

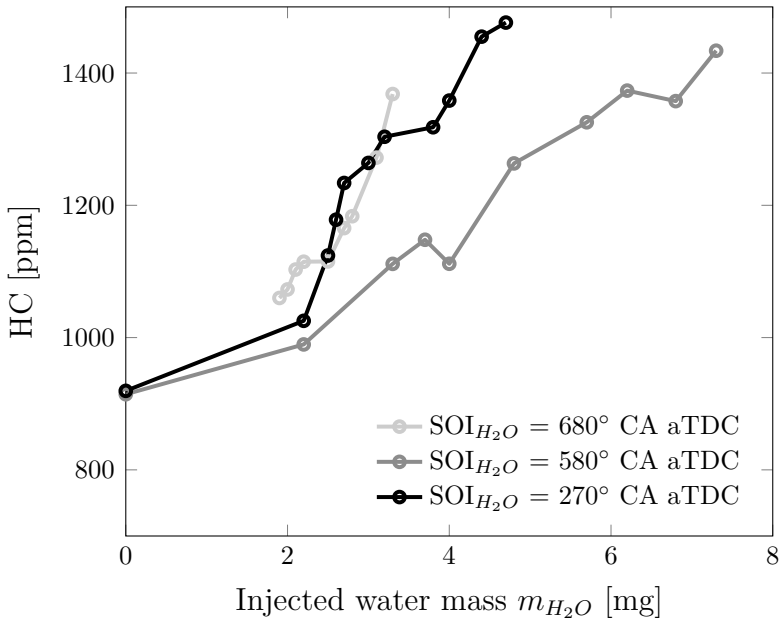

Figure 5.27: Impact of mass of injected water on unburnt hydro-carbon emission level.

This variation showed that an approximately linear relationship exists between injected water mass and the change in combustion phasing (Figure 5.21), burn duration (Figure 5.22) and pressure rise gradient (Figure 5.20). The increase in injected water

mass lowers the cylinder temperature thus reducing NO_X emissions (Figure 5.26) which increases HC emissions (Figure 5.27). Also as the amount of water is increased the delayed combustion phasing and long burn duration leads to increased exhaust temperatures (Figure 5.25). At high amount of injected water the cylinder charge is over cooled leading to a decrease in combustion stability or increase in standard deviation of IMEP (Figure 5.19).

As the injected water mass is increased the peak cylinder pressure is reduced, the combustion timing is delayed and the burn duration is increased which can be seen as the stretched appearance of the in-cylinder pressure trace in Figure 5.28.

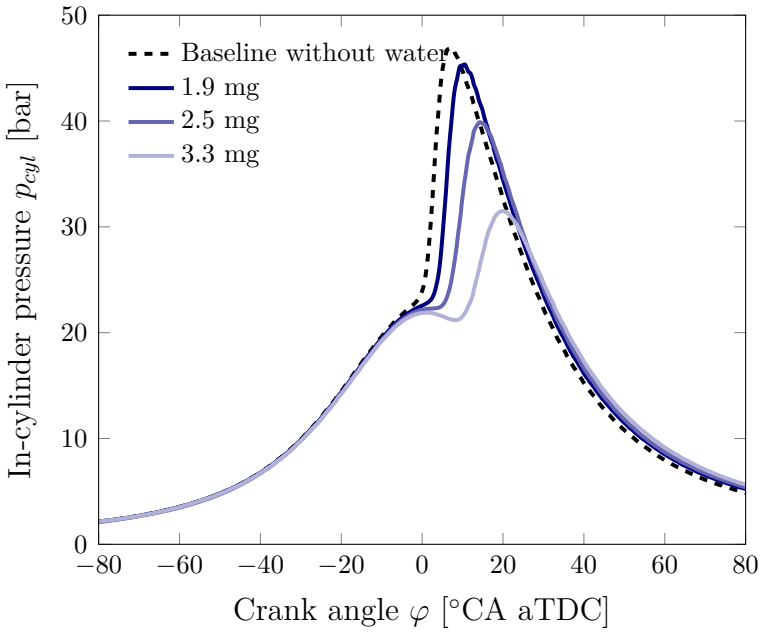

Figure 5.28: Variation of in-cylinder pressure due to changes in injected water mass. n = 1500 1/min, IMEP = 4.8 bar, p_{in}, p_{ex} = 1013 mbar, NVO = 163° CA, SOI_{H_2O} = 680° CA aTDC.

The water injection amount variation has two important results for water controller development. The first is that a linear relationship can be used to determine the amount of water to inject based on desired reduction in combustion phasing. The second, is that over-predicting the desired amount of water and then injection du-

ration can lead to a decrease in combustion stability which is opposite of what the controller should be doing.

5.3 Cyclic Water Injection

In the above sections the water injection timing and amount was investigated in steady state operation, however, to reduce cyclic variations the water injection controller will be operated on a cyclic basic so the lasting impact of the water injection on the subsequent combustion cycles must be understood. To test the impact of water injection on subsequent cycles without water injection a water injection was performed every 2nd, 3rd or 5th cycle. The cyclic effect of water injection on peak cylinder pressure, pressure rise rate, and CA_{50} can be seen in Figures 5.29 - 5.31, respectively.

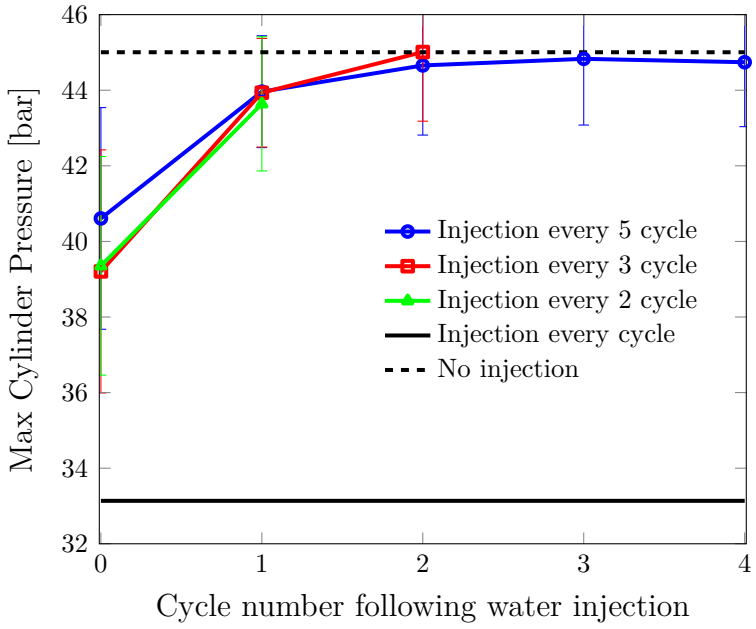

Figure 5.29: Cyclic-to-cycle effect from water injection on peak cylinder pressure.

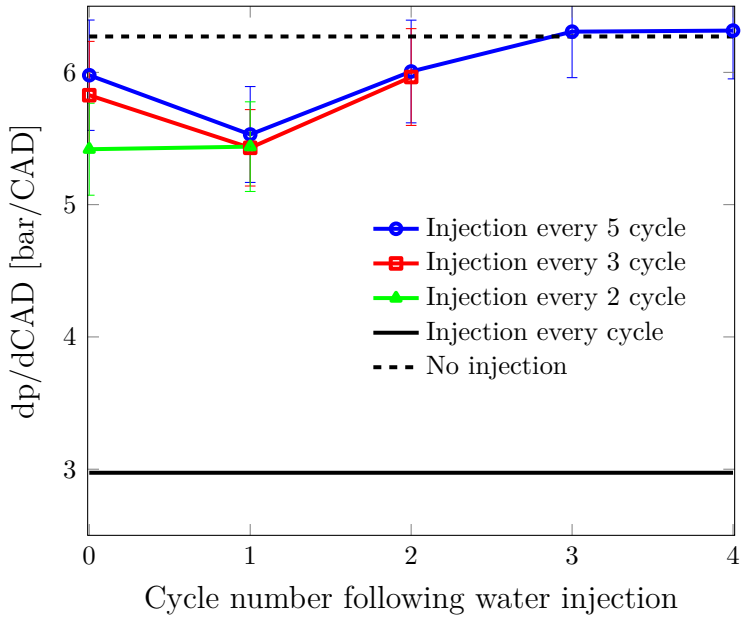

Figure 5.30: Cyclic-to-cycle effect from water injection on maximum cylinder pressure rise rate.

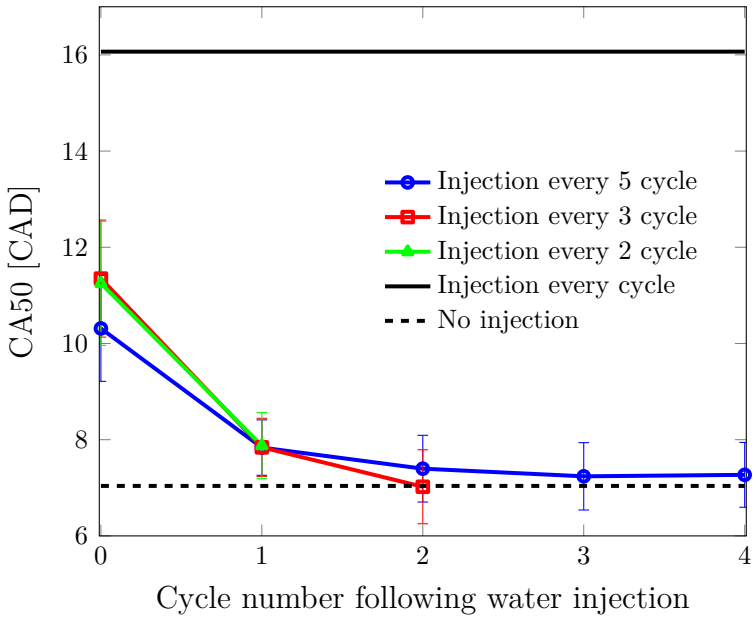

Figure 5.31: Cyclic-to-cycle effect from water injection on combustion phasing.

When examining the impact of cyclic injection every 2nd, 3rd, or 5th cycle, Figures 5.29 - 5.31 show that the number of cycles between water injections has a very small

impact on the combustion metrics presented. This effect is highly desirable as the water injection has a large effect on the cycle where the water is injected then by the 2nd cycle after water injection the combustion has returned to back to the same as when no water is used. There is a slight effect on the max cylinder pressure and CA_{50} on the cycle following the water injection however this impact is very small, 0.87 bar and 0.47° CA from the stationary operation without water injection. Therefore, if water was injected in the previous cycle less water is required to achieve the same impact. However, this amount is small and for simplicity of the controller design in this work, the impact of water injection will only be considered in the cycle where water is injected.

When comparing the cycles where water is injected every few cycles to the steady state operating condition with water injection every cycle a clear difference in all three combustion metrics can be seen. The cyclic actuated cycles with water injection have significantly less impact on the combustion phasing and cylinder pressure than the steady state water injection operation. The cause of this difference is attributed to longer term changes in combustion phasing and pressure rise rates leading to lower wall temperature which leads to delayed combustion phasing with lower cylinder pressures.

Chapter 6

Control Implementation [1]

In this work, cyclic variation will be reduced by preventing the early combustion following a late combustion by using direct water injection to cool the trapped exhaust gas to retard combustion phasing back to the desired value. The controllers developed are trying to prevent cycle 3 in Figure 2.3. This will be accomplished by considering three independent feedback variables: maximum cylinder pressure during NVO (control strategy A), heat release during NVO (control strategy B) and residual fuel mass at EVC (control strategy C) which come from the gas exchange model developed in Chapter 4. Then using correlations between these parameters and the combustion phasing of the upcoming cycle, $CA_{50}(i+1)$, a prediction can be made. This predicted combustion phasing is compared to the desired combustion phasing, $CA_{50}setpoint$, and a correlation to injected water amount is used as described in Section 5.2. The most efficient water injection timings of 270 and 580 °CA aTDC as identified in Section 5.2 will both be tested when possible. The controller structure can be visualized in Figure 6.1. This control strategy and the three feedback variables will be examined for their ability to improve HCCI combustion stability next.

[1] This chapter is based on [87], [88] and [89]

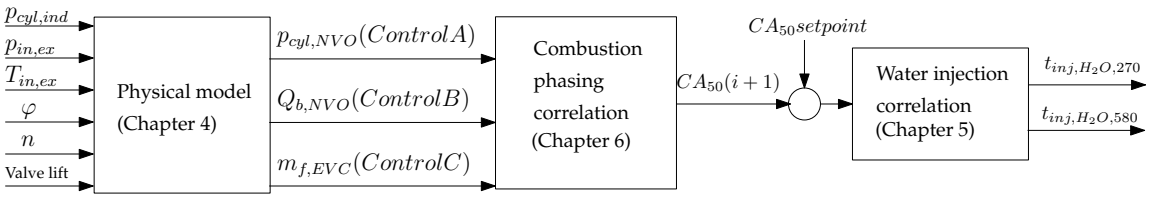

Figure 6.1: Schematic of water injection control strategy.

6.1 Maximum Cylinder Pressure during NVO based Controller

Of the three controllers tested the maximum pressure during the NVO recompression is the simplest as the cylinder pressure is a directly measured value and does not require any calculation other than pressure referencing. The increased pressure during NVO is representative of combustion occurring due to residual fuel burning during the NVO period. This burning fuel increases the temperature of the residual gas transferred to the upcoming cycle leading to an advanced combustion phasing and increased pressures. Direct water injection will then be used to help reduce the increased cylinder temperature caused by the burning fuel.

As the peak pressure of the NVO is used as controller input only one of the two possible water injection timings identified in Section 5.2 can be tested. Therefore, water injection occurs at 580° CA aTDC for all tests in this section.

The relationship between peak in-cylinder pressure during NVO and the combustion phasing of the upcoming cycle is shown in Figure 6.2. This correlation shows a distinct relationship between peak pressure and early combustion phasing. This is the expected trend as previously described. There is a large variation of the combustion phasing when the cylinder pressure is between 12 and 14 bar, therefore only the early cycles are selected and separated from the main point cloud as shown by the black points. These selected cycles are fitted with a linear regression, shown in red, to produce a prediction of the upcoming CA_{50} based on the NVO pressure.

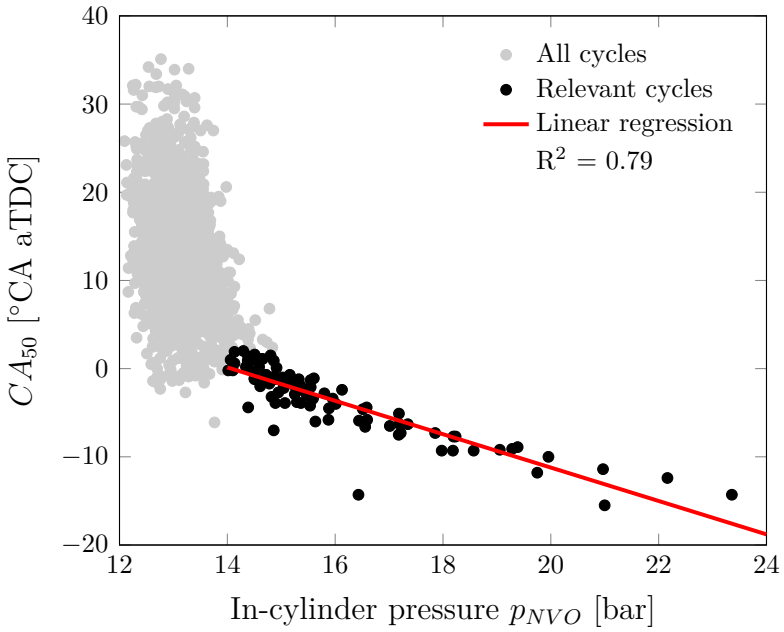

Figure 6.2: Linear regression of combustion phasing CA_{50} based on max cylinder pressure during NVO recompression, P_{NVO}.

6.1.1 Controller Results

The proposed control strategy is then tested on the SCRE, where 1000 consecutive cycles are collected and the water injection controller is activated after the first 500 cycles. The impact of the controller on IMEP can be seen in Figure 6.3. The water injection controller is able to effectively prevent the overshoot in IMEP caused by the early rapid combustion after an incomplete combustion. The lower IMEP cycles still remain as they are not the targeted cycles of this control strategy.

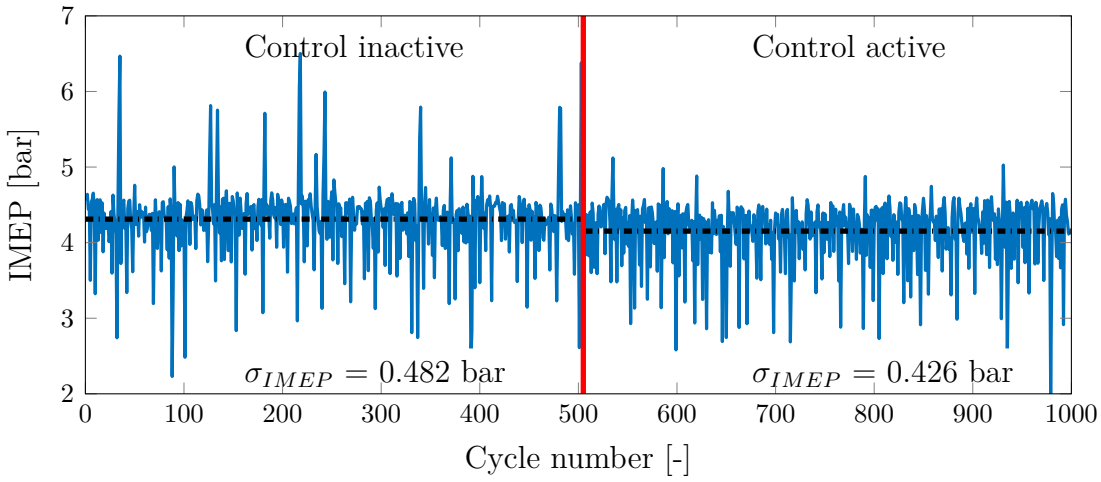

Figure 6.3: Control strategy A - IMEP combustion stability change due to in-cycle control. Controller is activated after 505 cycles.

Along with the improvement in IMEP shown a similar improvement could also be seen in pressure rise rate. Here the average pressure rise rate is reduced by 4.9%. The reduction in average pressure rise rate is desirable as operating at a lower pressure rise rate leads to reduced engine noise and wear. All improvements in combustion metrics due to controller A are presented in Table 6.1.

Table 6.1: Combustion stability improvement due to control strategy A.

SOI_{H_2O} [°CA]	IMEP [bar]		CA_{50} [°CA]		$\Delta\sigma_{IMEP}$ [%]	$\Delta\sigma$ CA_{50} [%]	$\Delta\overline{dp/d\varphi}$ [%]	Control Interactions [cycles]
Controller	Off	On	Off	On				
A-580	4.16	4.31	15.5	16.1	-2.7	4.42	-6.26	77/500

There are still some cycles that can be identified as having an IMEP above the average in Figure 6.3. These cycles could not be detected by the controller as there was no combustion in the NVO recompression, however, there was a late combustion in the previous cycle that lead to hotter exhaust gasses being trapped and transferred to the subsequent cycle. Another possibility is that combustion is late in the NVO

period leading to a pressure rise that was countered by the increasing cylinder volume. This is a limitation of only taking the peak pressure during the NVO recompression as more data is required to completely capture the in-cylinder state. Therefore the next controller strategies developed consider more variables of the in-cylinder state.

6.2 Heat Release based Controller

The heat release based controller can be broken down into two separate control interactions. The first is using the heat release of the previous cycle to predict any heat release during the NVO recompression and inject water to prevent the heat release, control strategy B-270. Secondly, it is possible to calculate the heat release during NVO recompression and inject water during the main compression to reduce the temperature equivalent to the heat release, control strategy B-580. These two strategies are in line with the two optimal water injection timings identified in Section 5.2.

The basic idea of this control strategy is that the heat absorbed by the injected water, Q_w, must compensate for the heat released during NVO recompression given by Equation 4.11. The heat required to heat the water, its evaporation and superheating of the gaseous water can be calculated using equation 2.8).

Then by equating equation 2.8 with the heat released during NVO recompression and using the injector function given in equation 4.20 the injection time for the corresponding water mass can be calculated.

6.2.1 Heat Release - Combustion to NVO

For the prediction of the heat release during the NVO recompression a correlation analysis of the heat release of the previous cycle, $Q_{comb(i-1)}$, is performed as shown in Figure 6.4. Here there are two distinct arms that extend out of the central point of the return map. These arms are formed by the cycles with an incomplete combustion,

these cycles are defined as having a heat release less than 450 J in the previous combustion event. The upper arm (red dots) are the cycles that we are interested in for the prediction of heat release in the NVO recompression and the lower arm (blue dots) are the cycles where a low heat release in the main combustion does not lead to a heat release in the NVO recompression.

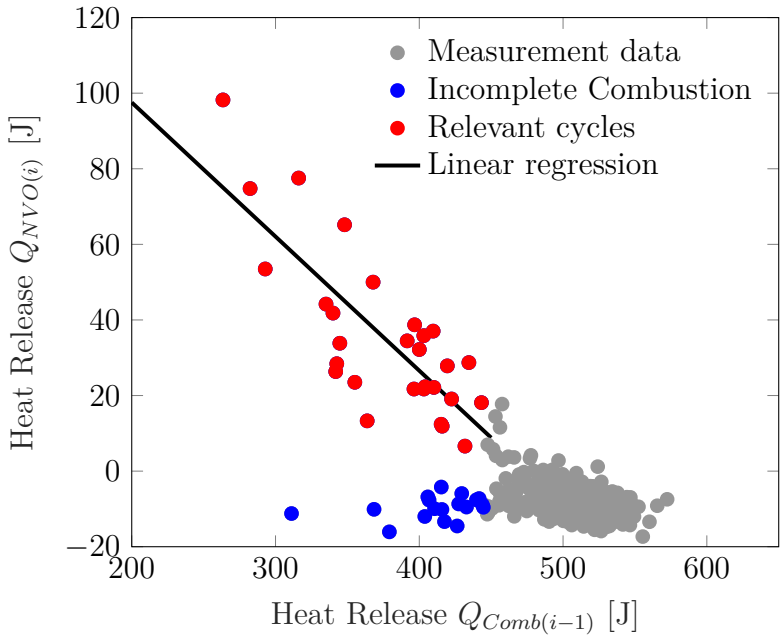

Figure 6.4: Correlation analysis of heat released in NVO recompression based on previous main combustion heat release at 1500 rpm and 4.2 bar IMEP.

As both of these arms are caused by a lower heat release than average during the main combustion it is necessary to investigate another variable to separate the two arms to be able to accurately predict a combustion event in the NVO period. The combustion phasing of the previous combustion, $CA50_{Comb(i-1)}$ can be used to separate the two arms as shown in Figure 6.5. Here the cycles (blue dots) with an early combustion phasing in the main combustion lead to no heat release in the NVO recompression. These early incomplete combustion cycles do not lead to heat release in the NVO recompression as the early combustion phasing allows enough time for the cylinder charge to cool. The cycles with incomplete combustion and a late

combustion phasing (red dots) are the cycles that correspond with the heat release in the NVO recompression. In these cycles the hot gas does not have time to cool and is transferred through EGR to the NVO recompression providing enough energy to ignite the remaining fuel from the incomplete combustion. Therefore it is necessary to consider both the heat release and combustion phasing of the previous combustion to predict any heat release in the upcoming NVO recompression.

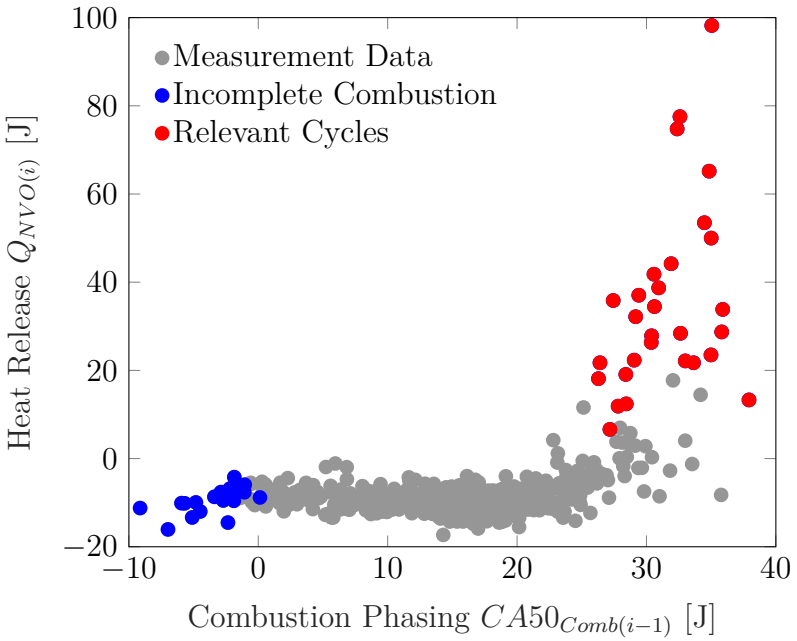

Figure 6.5: Correlation analysis of heat released in NVO recompression based on combustion phasing of the previous cycle at 1500 rpm and 4.2 bar IMEP.

Then using the results from Figures 6.4 and 6.5 the following equation can be used to predict the combustion for the upcoming NVO recompression.

$$Q_{NVO(i)} = a + b \cdot Q_{Comb(i-1)}, \text{ For } CA50_{Comb(i-1)} \geq 25°CA \tag{6.1}$$

Where a and b are coefficients defining the linear regression shown in Figure 6.4, which for this load point are 171 and -0.363, respectively.

The proposed controller is tested on the SCRE where 1000 consecutive cycles are

recorded and the controller is enabled after 500 cycles. Figure 6.6 clearly shows the controller's impact on the combustion phasing. This figure shows that the controller is successful at preventing the early combustion cycles. The average combustion phasing is retarded slightly due to the water injection controller preventing the very early combustion cycles, while the standard deviation of the combustion phasing is reduced by 1.57° CA showing a stability improvement.

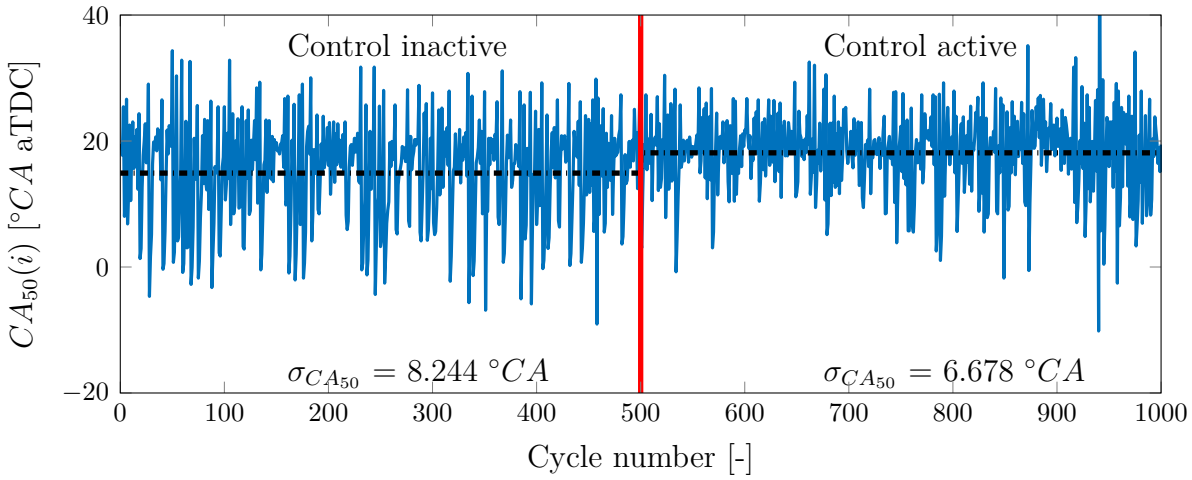

Figure 6.6: Combustion phasing, CA_{50}, stability improvement with control strategy B-270. Controller is activated after 500 cycles. NVO = 150 ° CA, IMEP = 4.2 bar, SOI_{H_2O} = 270° CA.

A similar trend can be seen in Figure 6.7 when analyzing the controller impact on the pressure rise rate. The controller is able to reduce the average pressure rise rate by 0.87bar/° CA but the significant improvement is the reduction of the maximum pressure rise rate of all 500 cycles from 8.5 to 6.7 bar/° CA. This reduction is important to reduce engine noise and wear.

The stability improvement of combustion phasing can be better seen in the change to the combustion phasing return map given in Figure 6.8 where the controller is successfully able to reduce the number of data points in the right arm of the plot. The controller is able is better prevent the very early cycles while it only has a small impact on the cycles that are only slightly early. This is a challenge of predicting the

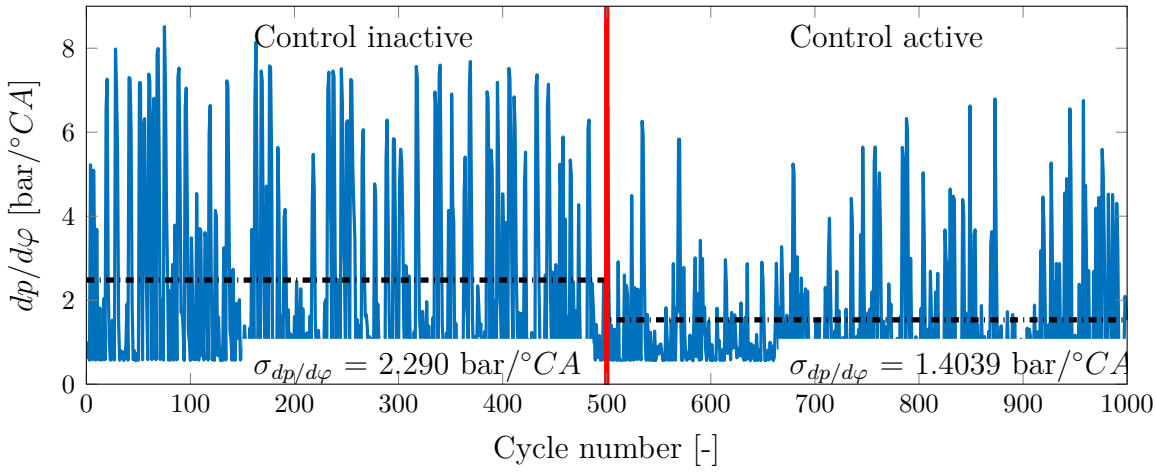

Figure 6.7: Maximum pressure rise rate, $dp/d\varphi$, stability improvement with control strategy B-270. Controller is activated after 500 cycles. NVO = 150 ° CA, IMEP = 4.2 bar, SOI_{H_2O} = 270° CA.

upcoming heat release. Generally, an increased amount of injected water would help to further retard the combustion phasing, however, during cycle 941 the controller injects water as it predicts a combustion in the upcoming NVO. This water prevents combustion in the recompression phase but also over cooled the trapped EGR which leads to a misfire in the subsequent cycle.

As the prediction of the heat release in the NVO period is not perfect and the water injection has a similar effect if the timing is moved to early into the compression phase as described in Section 5.2. It could be beneficial to remove the prediction and just react to any heat added during the NVO recompression phase. This alternate heat release controller will be described in the following section.

6.2.2 Heat Release - NVO to Combustion

Instead of using a predicted heat release during the NVO recompression the second heat release based control strategies uses the calculated heat release and injects water to reduce the temperature in the cylinder equal to the heat released to keep the combustion timing constant. Figure 6.9 shows the correlation between the heat release

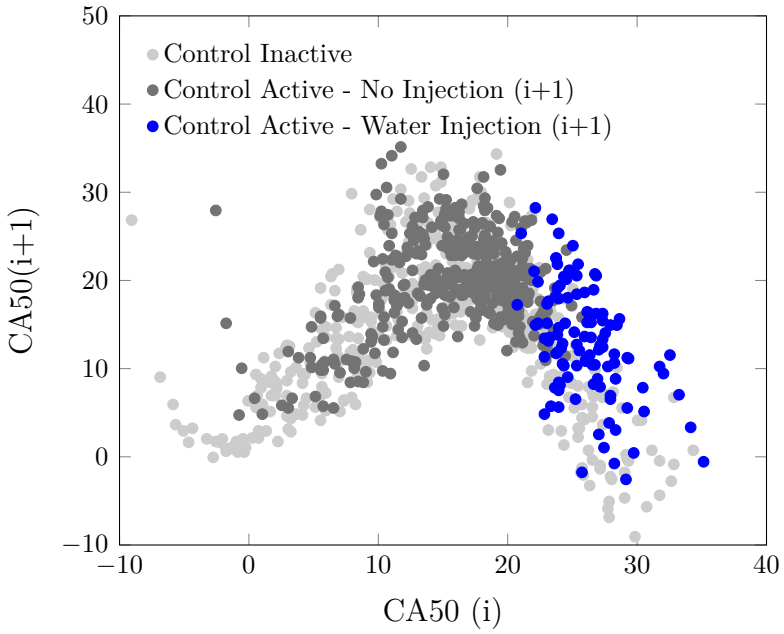

Figure 6.8: Combustion phasing return map showing stability improvement with control strategy B-270. NVO = 150 ° CA, IMEP = 4.2 bar, SOI_{H_2O} = 270° CA.

in the NVO recompression, Q_{NVO}, and the combustion phasing of the upcoming cycle, CA_{50}. Here a heat release over 25 J during the NVO period leads to an early combustion phasing. This is the expected result as the NVO combustion increases the temperature of the exhaust gas leading to an advanced combustion phasing of the upcoming combustion.

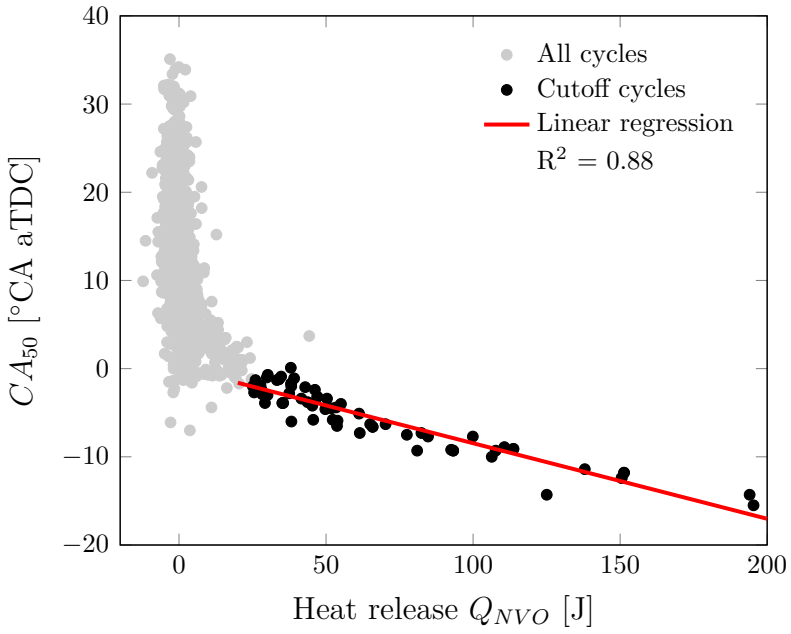

Figure 6.9: Linear regression of combustion phasing CA_{50} based on heat release during NVO recompression.

Figure 6.9 shows a clear leg extending out from the main cluster. Here cutoffs of above 25 J of heat release and 2° CA are used as cutoffs to select the relevant data point to provide a prediction of the upcoming combustion phasing. A linear regression is used for the prediction and as the R squared value is 0.88 this simple fit is able to capture the trend in the data quite well. The following equation can be used to predict the upcoming combustion phasing, $CA50_{pred(i)}$:

$$CA50_{pred(i)} = c + d \cdot Q_{NVO(i)} \tag{6.2}$$

Where c and d are coefficients defining the linear regression shown in Figure 6.9, they are 4.42 and -0.152 for the given load.

The water injection controller described above is tested on the SCRE and 1000 cycles are recorded. During the first 500 cycles the controller is inactive and at cycle 501 the controller is enabled. Figures 6.10 and 6.11 show the stability improvement

in the combustion phasing and the peak cylinder pressure, respectively. A significant improvement can be seen in both where the standard deviation of CA_{50} is reduced by 23.9% and the average pressure rise gradient is reduced from 1.24 to 1.05 bar/° CA.

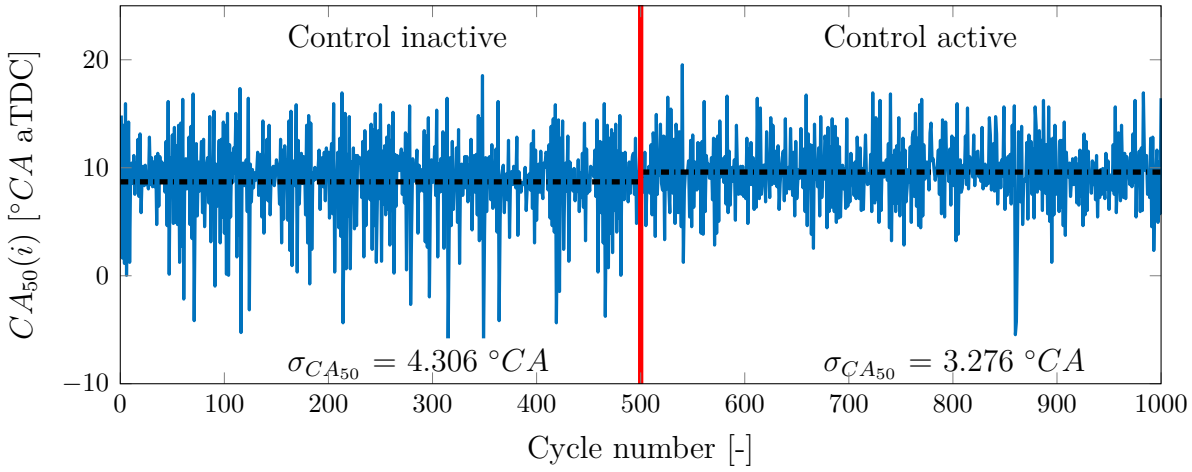

Figure 6.10: Combustion phasing, CA_{50}, stability improvement with control strategy B-580. Controller is activated after 500 cycles. NVO = 176 ° CA, IMEP = 2.4 bar, SOI_{H_2O} = 580° CA.

The stability improvement of the NVO to combustion heat release based controller can be seen clearly in Figure 6.12 where the controller is successfully able to shift the right arm of the return plot upwards. The controller successfully interrupts the "V-shaped" characteristic combustion phasing return pattern of HCCI combustion and therefore also reduced the number of data points in the left arm of the return map. However, as the controller is causal and requires a heat release in the NVO compression, it is unable to prevent the late combustion in the previous cycle but is able to retard the combustion phasing in the following cycle.

Even though the controller has shown an improvement in both the combustion phasing and maximum pressure rise gradient there is one cycle, cycle 860 where the controller is unable to prevent the early combustion phasing (-6.2° CA aTDC) and high pressure rise gradient (4.7 bar/° CA). This cycle does not exhibit any heat release in the NVO recompression phase and therefore the controller does not predict an early

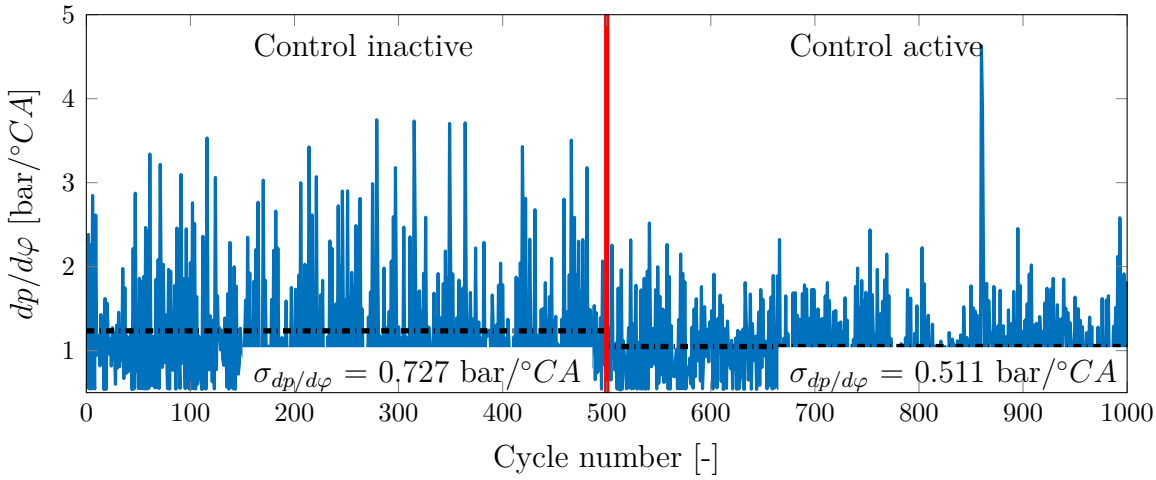

Figure 6.11: Maximum pressure rise rate, $dp/d\varphi$, stability improvement with control strategy B-580. Controller is activated after 500 cycles. NVO = 176 ° CA, IMEP = 2.4 bar, SOI_{H_2O} = 580° CA.

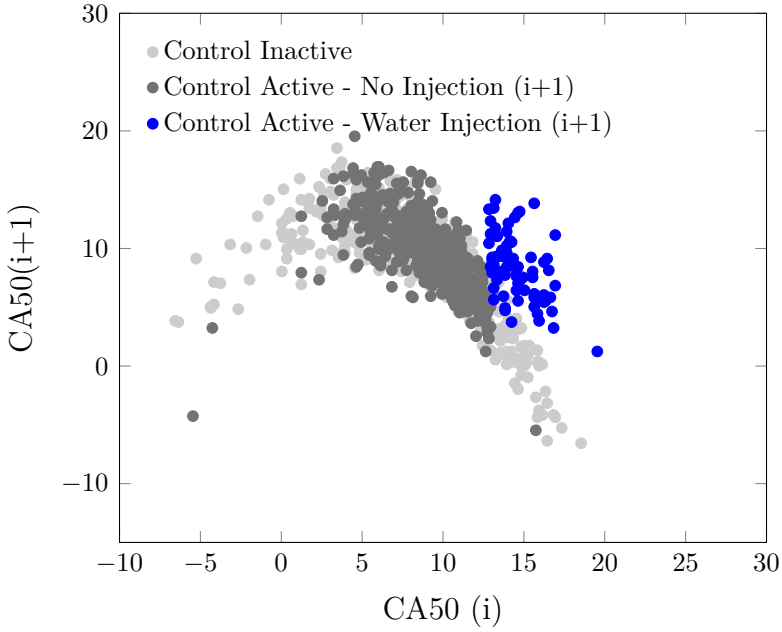

Figure 6.12: Combustion phasing return map showing stability improvement with control strategy B-580. NVO = 176 ° CA, IMEP = 2.4 bar, SOI_{H_2O} = 580° CA.

combustion phasing. This is a problem as this one cycle has the highest pressure rise gradient and one of the earliest combustion phasings of the 1000 measured cycles. This cycle shows that there is more to accurately predicting the upcoming combustion phasing than just the heat release in the NVO recompression.

In the previous cycle (859) there was an incomplete combustion leading to high residual fuel transferred through EGR to the next cycle. However, there was not enough thermal energy for the fuel to ignite during the NVO period (no heat release was detected by the controller) but the pre-reactions of combustion lead to a very early combustion phasing in the next cycle. This cycle can also be seen in Figure 6.12 as the one dark gray data point in the lower right corner.

The heat release based controller was able to improve the combustion stability, however, there is still room for improvement. To better predict the early combustion phasing a more detailed control variable is needed such as the residual fuel mass which will be explored in the following section.

6.2.3 Heat Release Controller Summary

Each of the two heat release based controllers were run at two load points of 2 and 4 bar representing a low and high load operating point, respectively. The improvement on the combustion metrics by the proposed controllers at these these load points have been summarized in Table 6.2. Here both control strategies at both load points are successful in reducing the standard deviation in both pressure rise rate and combustion phasing, however, the amount of improvement varies between controllers.

The overall effect of the controller on reducing the variation in IMEP is not as clear, with the B-580 controller at the high load having a significant improvement and the high load B-270 controller reducing the IMEP stability. Both low load operating points showed only a slight improvement in the standard deviation of IMEP.

The B-580 controller shows a more consistent improvement in the stability of both

Table 6.2: Combustion stability improvement due to control strategy B.

SOI_{H_2O} [°CA]	IMEP [bar]		CA_{50} [°CA]		$\Delta\sigma_{IMEP}$ [%]	$\Delta\sigma$ CA_{50} [%]	$\Delta\overline{dp/d\varphi}$ [%]	Control Interactions [cycles]
Controller	Off	On	Off	On				
B-580	4.22	4.30	15.1	15.4	-17.8	-12.9	-30.2	19/500
B-270	4.18	4.12	14.9	18.1	4.9	-19.0	-38.7	111/500
B-580	2.37	2.36	8.6	9.5	-8.3	-23.4	-32.9	73/500
B-270	2.21	2.22	8.3	8.3	-4.2	-13.6	-12.8	11/500

combustion phasing and pressure rise rate. As there is no prediction of the upcoming heat release and rather a reaction to any heat released the B-580 controller is the more robust controller of the two heat release based controllers presented. However, both controllers experience single cycles where an incorrect calculation of the amount of water to inject can lead to cycles with extremely early combustion phasing and high pressure rise rates. Generally, the controllers improve the stability of HCCI combustion although alternate controller inputs may be better suited to fully capture the incylinder state.

6.3 Residual Fuel Mass based Controller

It is expected that there is a strong relationship between a high residual fuel mass and an early combustion phasing which can be seen in Figure 6.13. Here the cycle with an early phasing can be seen as a leg extending out of the main point cloud. The relevant cycles were chosen by selecting a combustion phasing cut off of 2° CA and a residual fuel mass of 5 mg. These limits where manually tuned to capture the cycles with a clear trend from the main point cloud. With these chosen cycles a linear regression is performed to provide a relationship between combustion phasing

and residual fuel mass. By using the residual fuel mass as the control variable the model is physically based and is better able to handle changes in valve timings and boost pressures and have increased disturbance rejection.

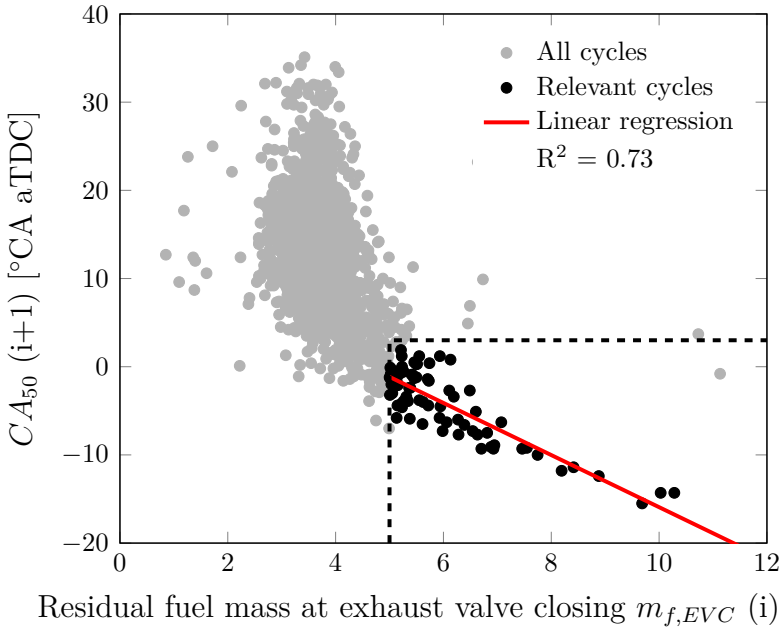

Figure 6.13: Linear regression of combustion phasing CA_{50} based on residual fuel mass at EVC. n = 1500 1/min, IMEP = 4.5 bar, single fuel injection at IVO, $m_{f,injected}$ = 16.1 mg.

When the correlation between residual fuel mass and combustion phasing and the previously discussed relationship between injected water mass and CA_{50} reduction (from section 5.2) a feed-forward controller can be implemented to regulate the combustion phasing of the cycle following a late combustion using water injection called control strategy C.

6.3.1 Multiple injection restriction

One assumption with a water injection controller based on residual fuel mass is that there will be an early combustion in the cycle following a misfire or late combustion phasing or when there is a high residual fuel amount. This is the case when there is

no water injection as shown in Figure 6.13, however, when water is added there is the risk that the added water will completely extinguish the combustion.

When using the residual fuel mass controller there are two possible outcomes. The first, which is the desired one, is that the high residual fuel can lead to combustion which is delayed by the added water back to the desired combustion phasing. The second outcome is the high injected water amount leads to over-cooling of the combustion chamber to the point where not enough thermal energy remains for the fuel to auto-ignite. Then the base controller design would continually increase the injected water amount proportional to the growing residual fuel in the cylinder as is the case in Figure 6.14. This leads to complete extinction of the HCCI combustion which then needs to be reignited by returning to spark ignition mode. This outcome leads to large amounts of water being injected into the cylinder and a large decrease in combustion stability and increased emissions.

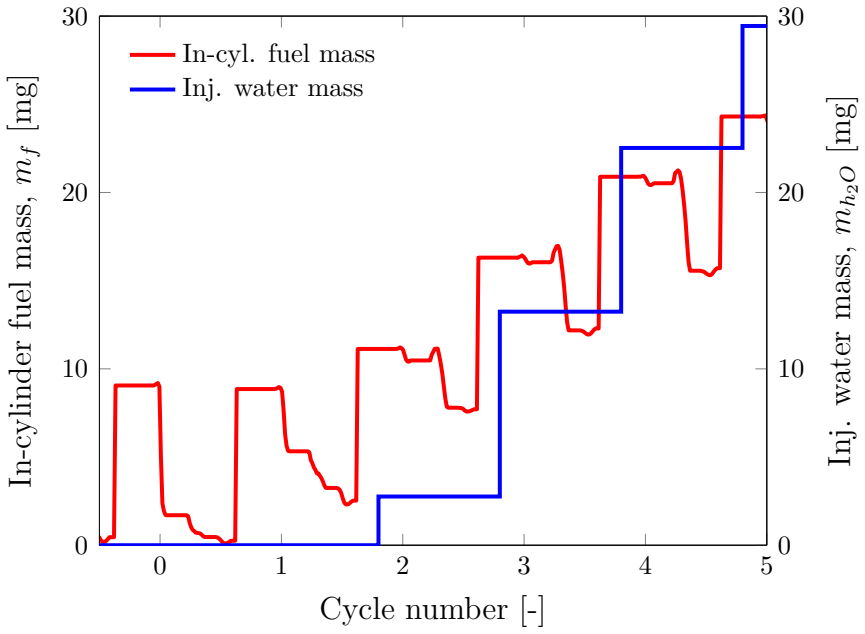

Figure 6.14: Growth of water injection amount resulting in complete HCCI extinction.

To prevent the complete extinction of the HCCI combustion the controller will not allow three consecutive water injections. This restriction can also decrease the

combustion stability as some cycles which are very early may require water injection in subsequent cycles, however, this added restriction helps to ensure that enough thermal energy will remain in the cycle following water injection to enable auto-ignition.

6.3.2 Experimental Controller Testing

The feed-forward controllers were tested for both water injection timings (C-270 and C-580) on the SCRE with the primary goal of reducing the cyclic variation shown in Figure 2.3. For each measurement point, 1000 consecutive cycles were recorded and the controller was activated after the first 500 cycles. This was used to examine the performance of the controller on increasing combustion stability.

The left side of Figure 6.15 shows five cycles where the controller is not activated. Here the cyclic variation that is characteristic for HCCI operation at the lean boundary can be seen. Cycle 194 and 195 are stable cycles that are followed by a late combustion in cycle 196. This late inefficient combustion leads to a high residual fuel mass which is transferred to the subsequent cycle as shown in the calculation of residual fuel mass. Then due to the high fuel mass and hot exhaust gas transferred to cycle 197 this leads to a rapid and early combustion. This increases the heat transfer to the cylinder wall and wall temperature as the high pressure rise rates blow away the thermal boundary layer which in turn advances the combustion phasing of the following cycle 198 [90].

The right side of Figure 6.15 shows the controller activated. Again cycle 719 and 720 are stable cycles followed by a late combustion in cycle 721. Now the FPGA model calculates the increased residual fuel mass in the cylinder and is able to predict an early combustion phasing leading to a control interaction with a water injection during the main compression to reduce the cylinder temperature. Here the control interaction is effective in lowering the cylinder temperature which retards combustion phasing and lowers the pressure rise rate to desired levels for cycles 722 and 723. The

same pattern can also be seen when the injection takes place shortly after EVC as the controller is also able to predict the early combustion following a late combustion.

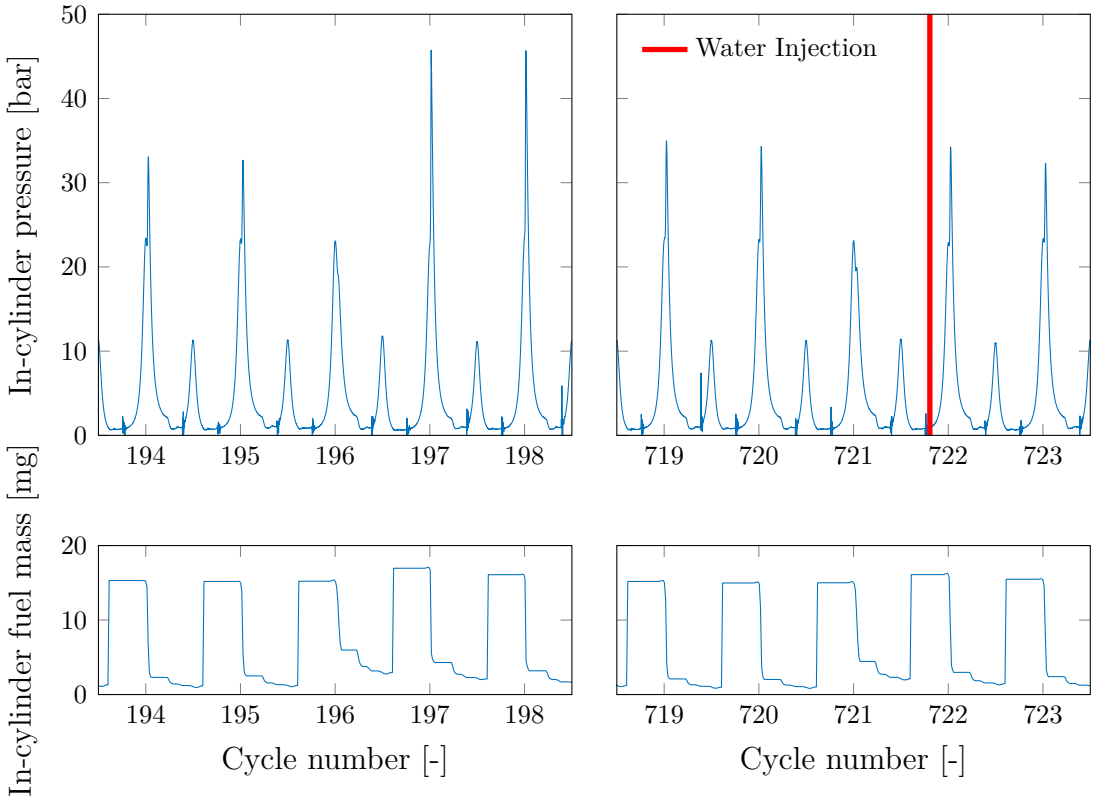

Figure 6.15: Control strategy C intervention. Left: In-cylinder pressure showing misfire after two stable cycles, followed by early rapid combustion when controller is not activated. Right: Same pattern as left figure, however, control intervention of water injection prevents the early rapid pressure and restores the combustion phasing to desired value. In-cylinder fuel mass traces are also shown.

The performance of the controller at stabilizing the combustion phasing over 500 cycles can be seen in Figure 6.16. Here the variation in combustion phasing is reduced for both injection timings after the controller is enabled at cycle 500. For the water injection at 580°CA aTDC, the standard deviation in combustion phasing is reduced from 7.64 to 6.0 °CA aTDC or a reduction of 21.4% when the controller is enabled. The average CA_{50} is slightly retarded from 15.9 to 17.9°CA aTDC but most of the cycles with a very early combustion phasing have been prevented, which helps to

stabilize the combustion overall as the number of very late combustion events have also been reduced. The same effect can also be seen when the water injection takes place at 270°CA aTDC, as the standard deviation in combustion phasing is reduced from 5.11 to 3.63°CA or a reduction of 29.0 %.

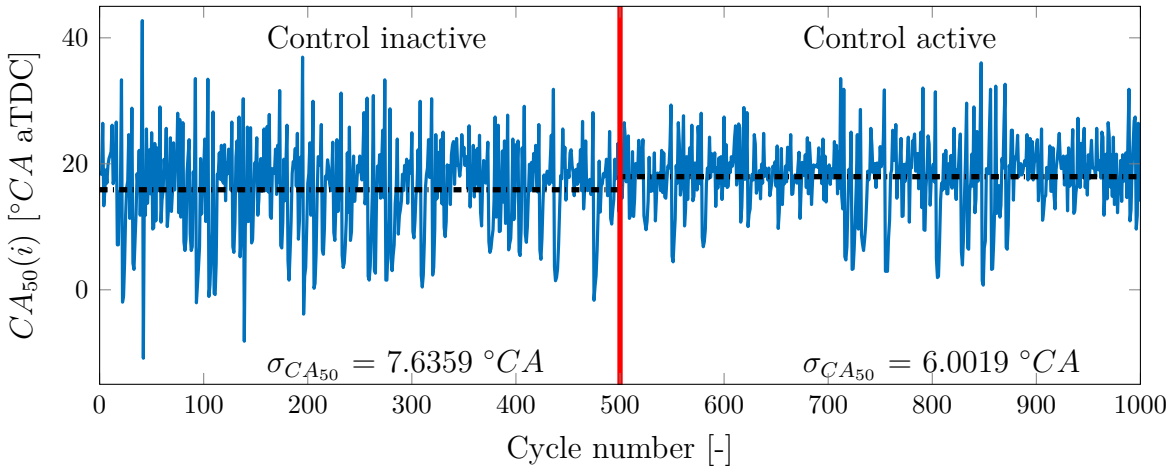

Figure 6.16: Combustion phasing, CA_{50}, stability improvement with control strategy C-580. Controller is activated after 500 cycles. n = 1500 1/min, NVO = 150 °CA, IMEP = 4.2 bar, (p_{inj}-p_{cyl}) = 50 bar, SOI_{H_2O} = 580°CA.

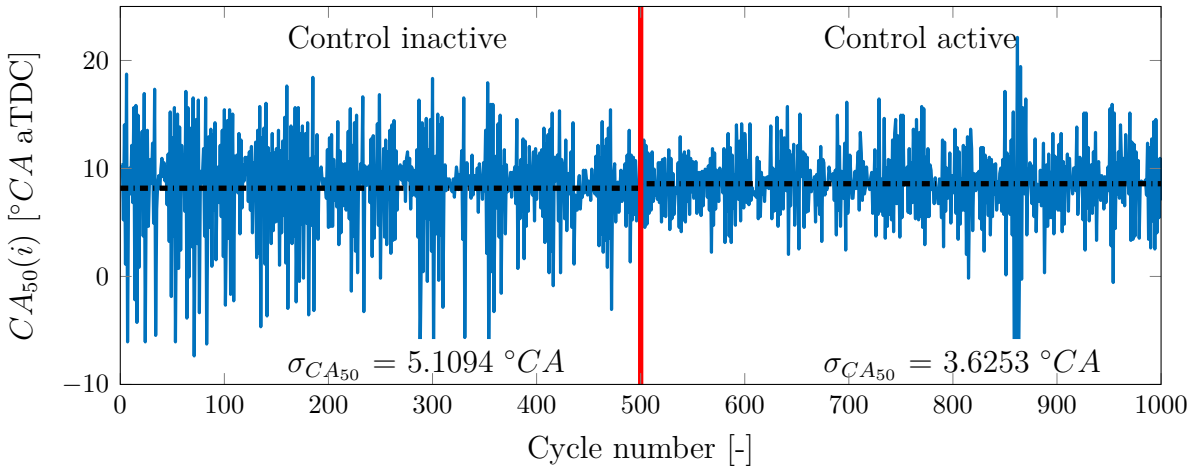

Figure 6.17: Combustion phasing, CA_{50}, stability improvement with C-270. Controller is activated after 500 cycles. n = 1500 1/min, NVO = 185°CA, IMEP = 2.4 bar, (p_{inj}-p_{cyl}) = 50 bar, SOI_{H_2O} = 270°CA.

Similar improvements can be seen when the peak pressure rise gradient of the

same 1000 cycles is shown in Figure 6.18. Once again after the controller is activated, the number of cycles with a high pressure rise gradient is significantly reduced for both injection timings. This can be seen by the reduction in average pressure rise gradient from 2.02 bar/°CA to 1.72 bar/°CA after the controller is enabled for the test with water injection at 580°CA. Similarly, when the water is injected at 270°CA the average pressure rise gradient decreases from 1.30 bar/°CA to 1.13 bar/°CA when the controller is activated. This is a significant improvement that is important to reduce combustion noise and engine wear.

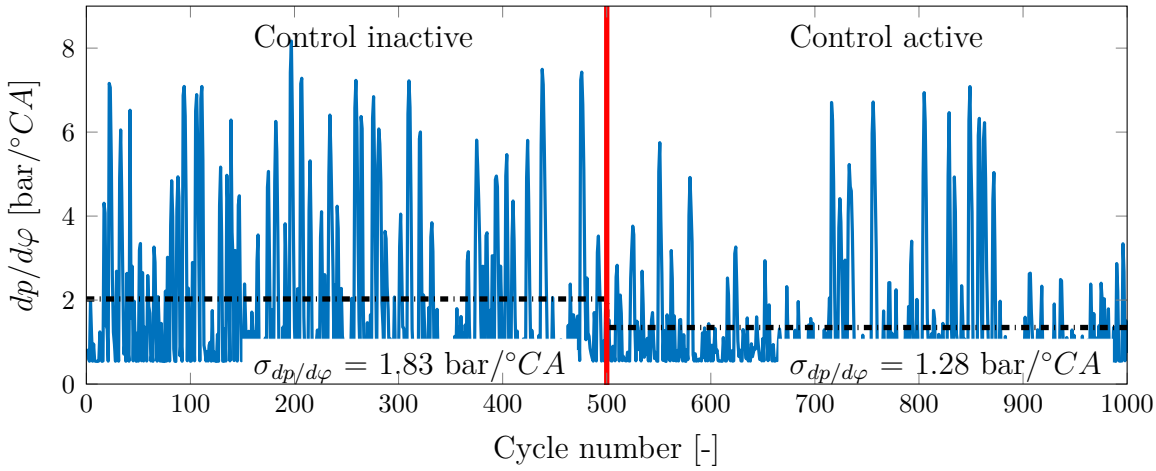

Figure 6.18: Maximum pressure rise rate, $dp/d\varphi$, stability improvement with C-580. Controller is activated after 500 cycles. n = 1500 1/min, NVO = 150 °CA, IMEP = 4.2 bar, (p_{inj}-p_{cyl}) = 50 bar, SOI_{H_2O} = 580°CA aTDC.

Figure 6.20 shows the improvement in the combustion stability from the use of the residual fuel mass based water injection controller for both water injection timings. The stability improvement can be seen as the reduction of cycles located in the right leg of the CA_{50} return map. Not only are the extreme cycles completely eliminated but the number of cycles outside the main point cloud are greatly reduced.

The blue colored points are the ones that are directly influenced by the water injection controller in cycle i+1. The combustion phasing in the current cycle is not affected, however, the combustion phasing in the following cycle is retarded by water

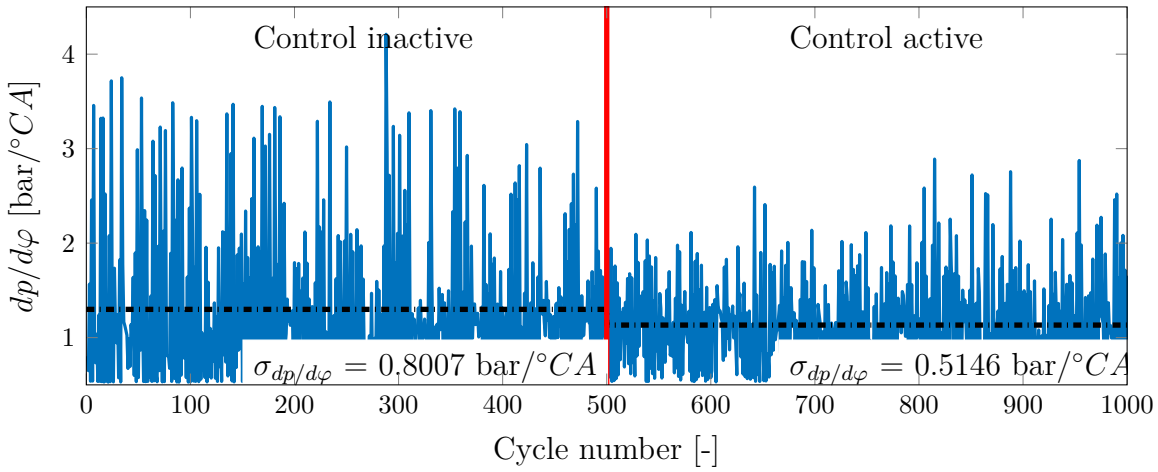

Figure 6.19: Maximum pressure rise rate, $dp/d\varphi$, stability improvement with C-270. Controller is activated after 500 cycles. n = 1500 1/min, NVO = 185 °CA, IMEP = 2.4 bar, (p_{inj}-p_{cyl}) = 50 bar, SOI_{H_2O} = 270°CA aTDC.

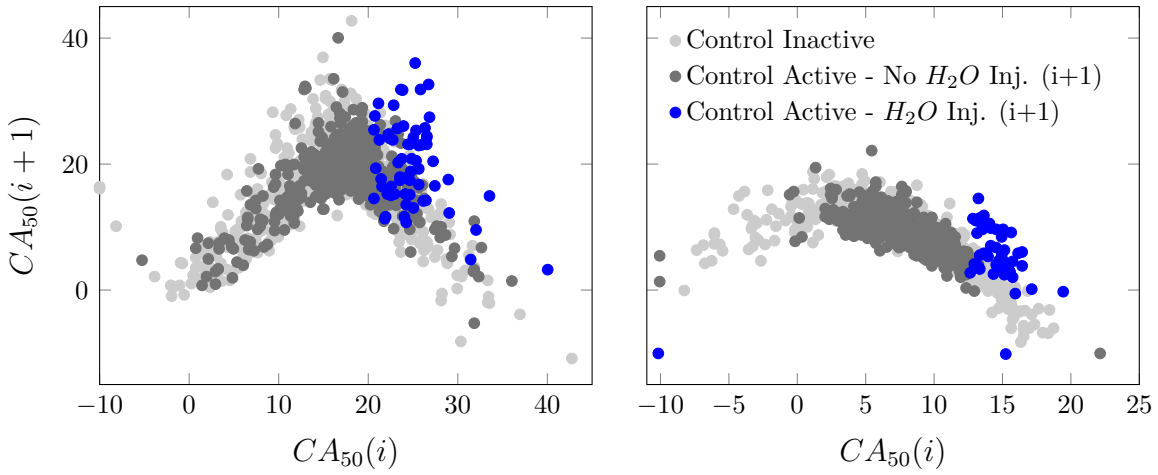

Figure 6.20: CA50 return map showing the improvement in combustion stability using control strategy C at n = 1500 1/min, (p_{inj}-p_{cyl}) = 50 bar and: **Left**: NVO = 150 °CA, IMEP = 4.2 bar, SOI_{H_2O} = 580° CA aTDC, **Right**: NVO = 185 °CA, IMEP = 2.4 bar, SOI_{H_2O} = 270°CA aTDC.

injection seen as a upward vertical shift in the figure. This removes the right leg of the return map. The reduction in the left leg is due to the prevention of an early combustion following an early combustion in the previous cycle. This can be seen in Figure 2.3 as the controller would prevent cycle 99 which would also prevent cycle 100 by shifting the combustion phasing back into the central area. Overall, a reduction in the spread of the CA_{50} return map shows improvement in combustion stability when the controller is activated.

The presence of some cycles remaining outside the central point cloud on the CA_{50} return map shows that the model based controller does not capture all the physics completely so there is a model plant mismatch. This effect can also be seen in Figures 6.16-6.19 where a band of a large variation in CA_{50} and pressure rise rate can be seen even when the controller is active. The early cycles with a high pressure gradient are due to the controller not accurately predicting an early combustion and therefore not adding water (the dark gray cycles in the right leg of Figure 6.20) or too little water mass added to the cycles (the blue points that remain in lower right side of the return maps). There are also cases where too much water has been injected resulting in a late combustion phasing and extremely low pressure rise rates (the blue points that appear in the upper right side of the return map). This over actuation of water could also cause a misfire and result in a high transfer of fuel to the next cycle resulting in an early very rapid combustion which is what the controller is trying to prevent.

Those cycle with a very early combustion phasing and additional misfire cycles that are caused by the water injection are one challenge with the proposed controller. An example where the controller added additional misfire cycles followed by a very early strong combustion can be seen in Figure 6.21.

Here an incomplete combustion in cycle 857 leads to an increase in residual fuel mass leading to the injection of water. This water causes a misfire in the subsequent cycle (858) leading to a further increase in residual fuel. As previously discussed, this

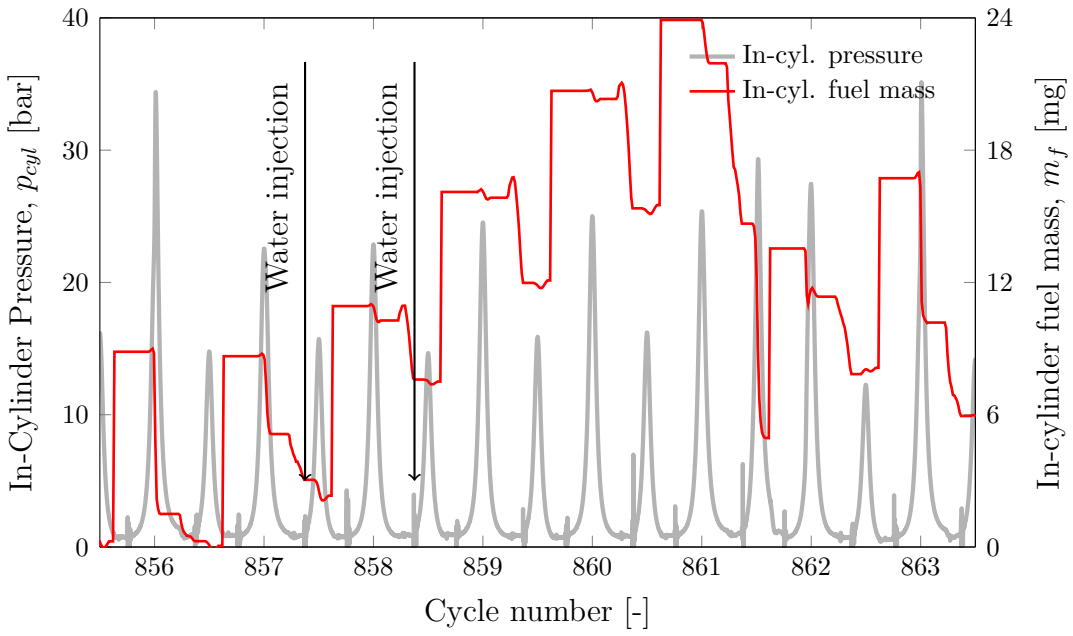

Figure 6.21: Additional cyclic instability due to control interaction at NVO = 185 ° CA, IMEP = 4.2 bar, SOI_{H_2O} = 270° CA aTDC.

is a known problem with a controller strictly based on the residual fuel mass and to combat this the controller no longer injects water in cycle 859. However, three more misfire cycles (859-861) occur leading to a very high in-cylinder fuel mass. This fuel then ignites during the NVO recompression of cycle 861 which leads to the early combustion phasing in cycle 863.

Only allowing 2 consecutive water injection events helps to reduce the number of occurrences of this pattern, however, as can be seen it does not eliminate it. To further improve the controller and prevent this extinction of HCCI combustion it is necessary to couple the second consecutive water injection with a spark to ensure there is combustion. This spark could have a late timing but is needed in order to prevent multiple cycles without a combustion event.

To improve the amount of water injection the relationship between residual fuel mass and water injection amount may need to be adapted with a non-linear relationship or a physical water evaporation model. This will help to consider non-linearity

of the injector at small injection durations. However, overall both injection timings using the real-time calculated fuel mass shows significant stability improvements for various measurement points as summarized in Table 6.3.

Table 6.3: Combustion stability improvement due to control strategy C.

SOI_{H_2O} [°CA]	IMEP [bar]		CA_{50} [°CA]		$\Delta\sigma_{IMEP}$ [%]	$\Delta\sigma$ CA_{50} [%]	$\Delta\overline{dp/d\varphi}$ [%]	Control Interactions [cycles]
Controller	Off	On	Off	On				
C-580	4.28	4.32	15.9	18.0	-11.2	-21.4	-33.5	63/500
C-580	2.39	2.41	8.6	8.9	-10.0	-14.6	-14.3	33/500
C-580	4.23	4.24	15.2	17.2	-9.3	-22.2	-28.5	34/500
C-580	2.38	2.38	8.6	9.1	-0.2	-20.6	-32.0	47/500
C-270	2.40	2.45	8.2	8.6	-22.0	-29.1	-12.7	49/500
C-270	2.80	2.96	8.3	9.9	-27.3	-33.5	-20.0	14/500
C-270	2.38	2.29	8.2	9.5	8.4	-10.1	-16.1	125/500
C-270	3.30	3.41	10.9	12.2	-13.5	-22.3	-17.2	69/500

The various operating points chosen show that the controller works over a range of operating conditions while showing a decrease in the standard deviation of combustion phasing and power output. The controller was also successful in reducing average pressure rise rates with control interventions in approximately 10% of the cycles. The water injection at 270° CA aTDC was more effective at reducing cyclic variations while the later water injection timing of 580° CA aTDC has a larger impact on the average pressure rise rate. Overall, the residual fuel mass feedforward controller using either injection timings performed well with only slight differences.

Chapter 7

Conclusions

7.1 FPGA Based Gas Exchange Model

The real time physics based gas exchange model was successfully implemented on the FPGA hardware. The model was validated offline to an industry standard model which showed very comparable results despite the lack of a gas dynamic model for the intake and exhaust manifolds. The model was also tested at various resolutions which showed that a calculation rate of under 1°CA is required to minimize the error between models. This calculation rate is difficult to achieve using standard microprocessor based ECU's leading to the requirement to use FPGA based controllers.

The FPGA model was then experimentally tested and compared to offline calculated results where the modeled in-cylinder state matched very well. The conversion to a real-time model introduced sources of error: fixed point calculation error, and physics simplification errors. Of these two error sources, the error introduced from using fixed point arithmetic was more significant and for example introduced an error of approximately 1% to the calculation of constant volume specific heat capacity. This error source can be minimized by careful selection of the necessary binary precision.

The developed FPGA gas exchange model was tested at various operating conditions and compared to offline calculated values of the fresh air ratio. The online

model was able to accurately calculate the in-cylinder state at the wide operating range with a maximum error of under 4.5% for all the variations tested. Therefore, the FPGA based model which is capable of accurately calculating the current cylinder state within 0.1°CA which is highly valuable for in-cycle control strategies and will be extremely useful for various future controllers.

7.2 Impact of Direct Water Injection on HCCI

Steady state water injection tests showed that two injection timings where the injected water mass has the largest effect on the combustion phasing are present. These timings are 270 and 580 °CA aTDC which are early in the NVO and main compression phase. These timings show that the water needs time to fully evaporate to cool the cylinder charge and delay the combustion pre-reactions. Both of these timings produced similar effects on the combustion phasing and pressure rise rates, allowing either timing to be used for possible control strategies.

Steady state variation of the injected water mass showed that combustion phasing is retarded proportionally to the injected water mass. This result allows the use of a linear regression to estimate the amount of water to inject based of the required delay of the combustion phasing.

A cyclic water injection test then showed that the injected water has a large effect on the current cycle but only a small impact on the next cycle following an injection and the effects where almost completely negligible after the second cycle. Therefore, for simplicity and controller implementation it is possible to consider each cycle individually without respect to previous water injections while only introducing a small amount of error.

7.3 Feed-Forward Water Injection Controller

The feed-forward water injection controller was experimentally tested in an attempt to improve the combustion stability of HCCI. The controllers used the current in-cylinder state from the developed gas exchange model including pressure, heat released during main combustion and NVO periods as well as residual fuel mass. Each of the tested controllers had their advantages and disadvantages, however, each controller showed an improvement in the standard deviation of combustion phasing and IMEP, along with a reduction in the peak pressure rise rate.

Of the controllers tested, the residual fuel mass based controller was better able to reduce the standard deviation of IMEP while providing a reduction in the standard deviation of combustion phasing. The average pressure rise rate was also reduced, similar to the heat released based controller. The residual fuel mass based controller has the most detailed in-cylinder state calculation. The calculation of residual fuel considers residual fuel passed from previous cycles and considers the fuel leaving through exhaust flows in combination with the fuel that is burnt during the main and NVO heat release periods. As such, it was expected to be the most robust to disturbances in the system which was validated during experimental testing.

Although the controller improves the stability of HCCI combustion it is not perfect and cycles still remain where there is an early combustion phasing that can not be prevented or cycles which have a very late combustion phasing due to the injected water. These cycles are attributed to an incorrect calculation of: injected water mass, calculation of the controller input variable of heat release, or residual fuel mass.

7.4 Future Work

Possible future work to extend this work include:

- The injector used for water injection should be replaced with an injector that

is capable of smaller injection amounts. This would help to capture more cycles that are early but do not require the current minimum water injection amount. This new injector would also allow a high water injection pressure to be used allowing the water to evaporate more quickly helping to improve its effectiveness.

- Currently linear correlations are used to predict the combustion phasing of the upcoming cycle, therefore, it is suggested to add a combustion model to the FPGA gas exchange model to allow a more accurate prediction of the upcoming combustion. This will help to improve the accuracy of the controller.

- Chapter 5 showed that water injection has a slight impact on the following cycle, this could be accounted for in the water controllers to prevent an over injection of water.

- The feedforward controller could be replaced with an iterative learning controller which could actively adapt the relation between the injected water mass and change in combustion phasing over time.

- A Computational Fluid Dynamics (CFD) simulation including water injection could help to understand the physics of the water mixing in the cylinder and how it affects the temperature gradients within the cylinder.

References

[1] M. Williams and R. Minjares, "A technical summary of Euro 6/VI vehicle emission standards," *International Council for Clean Transportation (ICCT), Washington, DC, accessed July*, vol. 10, p. 2017, 2016.

[2] E. Parliament and the Council of the European Union, "Regulation (EC) No 715/2007 of the European Parliament and of the Council of 20 June 2007 on type approval of motor vehicles with respect to emissions from light passenger and commercial vehicles (Euro 5 and Euro 6) and on access to vehicle repair and maintenance information.," *Official Journal of the European Union L Series.*, vol. 171, 2007.

[3] M. Weiss, P. Bonnel, J. Kühlwein, A. Provenza, U. Lambrecht, S. Alessandrini, M. Carriero, R. Colombo, F. Forni, G. Lanappe, *et al.*, "Will Euro 6 reduce the nox emissions of new diesel cars?–insights from on-road tests with portable emissions measurement systems (PEMS)," *Atmospheric Environment*, vol. 62, pp. 657–665, 2012.

[4] Q. Schiermeier, "The science behind the Volkswagen emissions scandal," *Nature News*, 2015.

[5] R. H. Stanglmaier and C. E. Roberts, "Homogeneous charge compression ignition (HCCI): benefits, compromises, and future engine applications," tech. rep., SAE Technical Paper, 1999.

[6] M. Yao, Z. Zheng, and H. Liu, "Progress and recent trends in homogeneous charge compression ignition (HCCI) engines," *Progress in Energy and Combustion Science*, vol. 35, no. 5, pp. 398 – 437, 2009.

[7] M. Shahbakhti and C. Koch, "Characterizing the cyclic variability of ignition timing in a homogeneous charge compression ignition engine fuelled with n-heptane/iso-octane blend fuels," *International Journal of Engine Research*, vol. 9, no. 5, pp. 361–397, 2008.

[8] S. Onishi, S. H. Jo, K. Shoda, P. Do Jo, and S. Kato, "Active thermo-atmosphere combustion (ATAC)-a new combustion process for internal combustion engines," tech. rep., SAE Technical Paper, 1979.

[9] R. K. Maurya and A. K. Agarwal, "Experimental study of combustion and emission characteristics of ethanol fuelled port injected homogeneous charge compression ignition (HCCI) combustion engine," *Applied Energy*, vol. 88, no. 4, pp. 1169 – 1180, 2011.

[10] J. B. Heywood *et al.*, *Internal combustion engine fundamentals*, vol. 930. Mcgraw-hill New York, 1988.

[11] R. Stone, *Introduction to internal combustion engines*. Palgrave Macmillan, 2012.

[12] Z. Wang, H. Liu, and R. D. Reitz, "Knocking combustion in spark-ignition engines," *Progress in Energy and Combustion Science*, vol. 61, pp. 78 – 112, 2017.

[13] S. Saxena and I. D. Bedoya, "Fundamental phenomena affecting low temperature combustion and HCCI engines, high load limits and strategies for extending these limits," *Progress in Energy and Combustion Science*, vol. 39, no. 5, pp. 457–488, 2013.

[14] E. Hellstrom, J. Larimore, S. Jade, A. G. Stefanopoulou, and L. Jiang, "Reducing cyclic variability while regulating combustion phasing in a four-cylinder HCCI engine," *IEEE Transactions on Control Systems Technology*, vol. 22, no. 3, pp. 1190–1197, 2014.

[15] J. Larimore, E. Hellström, J. Sterniak, L. Jiang, and A. G. Stefanopoulou, "Experiments and analysis of high cyclic variability at the operational limits of spark-assisted HCCI combustion," in *2012 American Control Conference (ACC)*, pp. 2072–2077, June 2012.

[16] B. Lehrheuer, S. Pischinger, M. Wick, J. Andert, D. Berneck, D. Ritter, T. Albin, and M. Thewes, "A study on in-cycle combustion control for gasoline controlled autoignition," in *SAE Technical Paper*, SAE International, 04 2016.

[17] E. Nuss, D. Ritter, M. Wick, J. Andert, D. Abel, and T. Albin, "Reduced order modeling for multi-scale control of low temperature combustion engines," in *Active Flow and Combustion Control 2018*, pp. 167–181, Springer, 2019.

[18] A. Ghazimirsaied and C. R. Koch, "Controlling cyclic combustion timing variations using a symbol-statistics predictive approach in an HCCI engine," *Applied energy*, vol. 92, pp. 133–146, 2012.

[19] A. Vaughan and S. V. Bohac, "A cycle-to-cycle method to predict HCCI combustion phasing," in *ASME 2013 Internal Combustion Engine Division Fall Technical Conference*, pp. V001T03A026–V001T03A026, American Society of Mechanical Engineers, 2013.

[20] J. A. Eng, "Characterization of pressure waves in HCCI combustion," in *SAE Powertrain & Fluid Systems Conference & Exhibition*, SAE International, oct 2002.

[21] R. K. Maurya, *Characteristics and control of low temperature combustion engines: employing gasoline, ethanol and methanol*. Springer, 2017.

[22] E. Hellström, A. Stefanopoulou, J. Vavra, A. Babajimopoulos, D. N. Assanis, L. Jiang, and H. Yilmaz, "Understanding the dynamic evolution of cyclic variability at the operating limits of HCCI engines with negative valve overlap," *SAE International Journal of Engines*, vol. 5, pp. 995–1008, apr 2012.

[23] V. Rapp, N. Killingsworth, P. Therkelsen, and R. Evans, "Lean-burn internal combustion engines," in *Lean Combustion (Second Edition)*, pp. 111 – 146, Boston: Academic Press, second edition ed., 2016.

[24] L. Shi, Y. Cui, K. Deng, H. Peng, and Y. Chen, "Study of low emission homogeneous charge compression ignition (HCCI) engine using combined internal and external exhaust gas recirculation (EGR)," *Energy*, vol. 31, no. 14, pp. 2665 – 2676, 2006.

[25] L. Manofsky, J. Vavra, D. Assanis, and A. Babajimopoulos, "Bridging the gap between HCCI and SI: Spark-assisted compression ignition," *SAE Technical Papers 2011-01-1179*, 2011.

[26] K. Stapf, D. Seebach, F. Fricke, S. Pischinger, K. Hoffmann, and D. Abel, "CAI-Engines: modern combustion system to face future challenges," in *SIA Int. Conference—The Spark Ignition Engine of the Future, Strasbourg*, 2007.

[27] D. Cleary and G. Silvas, "Unthrottled engine operation with variable intake valve lift, duration, and timing," in *SAE World Congress & Exhibition*, SAE International, apr 2007.

[28] K. Ebrahimi, C. Koch, and A. Schramm, "A control oriented model with variable

valve timing for HCCI combustion timing control," in *SAE Technical Paper*, SAE International, 04 2013.

[29] G. Haraldsson, P. Tunestål, B. Johansson, and J. Hyvönen, "HCCI combustion phasing with closed-loop combustion control using variable compression ratio in a multi cylinder engine," *SAE Technical Papers 2003-01-1830*, 2003.

[30] R. V. Klikach, "Investigation and analysis of RCCI using NVO on a converted spark ignition engine," Master's thesis, University of Alberta, 2018.

[31] C. E. Slepicka, "Iterative learning control for fuel robust HCCI," Master's thesis, University of Alberta, 2016.

[32] S. L. Kokjohn, R. M. Hanson, D. A. Splitter, and R. D. Reitz, "Experiments and modeling of dual-fuel HCCI and PCCI combustion using in-cylinder fuel blending," *SAE International Journal of Engines*, vol. 2, pp. 24–39, nov 2009.

[33] J. Benajes, S. Molina, A. García, E. Belarte, and M. Vanvolsem, "An investigation on RCCI combustion in a heavy duty diesel engine using in-cylinder blending of diesel and gasoline fuels," *Applied Thermal Engineering*, vol. 63, no. 1, pp. 66 – 76, 2014.

[34] M. Thewes, H. Baumgarten, J. Scharf, G. Birmes, A. Balazs, B. Lehrheuer, and F. Hoppe, "Water injection-high power and high efficiency combined," in *25th Aachen Colloquium Automobile*, pp. 345–380, 2016.

[35] J. E. Dec, "Advanced compression-ignition engines—understanding the in-cylinder processes," *Proceedings of the Combustion Institute*, vol. 32, no. 2, pp. 2727 – 2742, 2009.

[36] R. Maurya and A. Agarwal, "Experimental investigations of performance, combustion and emission characteristics of ethanol and methanol fueled HCCI engine," *Fuel Processing Technology*, vol. 126, pp. 38–48, 2014.

[37] A. Tsolakis, A. Megaritis, and D. Yap, "Application of exhaust gas fuel reforming in diesel and homogeneous charge compression ignition (HCCI) engines fuelled with biofuels," *Energy*, vol. 33, no. 3, pp. 462–470, 2008.

[38] Y. Yang, J. Dec, N. Dronniou, and B. Simmons, "Characteristics of isopentanol as a fuel for HCCI engines," *SAE International Journal of Fuels and Lubricants*, vol. 3, no. 2, pp. 725–741, 2010.

[39] B. Rajesh Kumar and S. Saravanan, "Partially premixed low temperature combustion using dimethyl carbonate (DMC) in a di diesel engine for favorable smoke/NOx emissions," *Fuel*, vol. 180, pp. 396–406, 2016.

[40] J. Mack, D. Schuler, R. Butt, and R. Dibble, "Experimental investigation of butanol isomer combustion in homogeneous charge compression ignition (HCCI) engines," *Applied Energy*, vol. 165, pp. 612–626, 2016.

[41] J. H. Mack, S. M. Aceves, and R. W. Dibble, "Demonstrating direct use of wet ethanol in a homogeneous charge compression ignition (HCCI) engine," *Energy*, vol. 34, no. 6, pp. 782 – 787, 2009.

[42] T. Todman, G. Constantinides, S. Wilton, O. Mencer, W. Luk, and P. Cheung, "Reconfigurable computing: Architectures and design methods," in *Reconfigurable computing*, vol. 152, pp. 193–207, 2005.

[43] K. Parnell and R. Bryner, "Comparing and contrasting FPGA and microprocessor system design and development," *White Paper, XILINX Corporation*, 2004.

[44] S. Hauck and A. DeHon, *Reconfigurable computing: the theory and practice of FPGA-based computation*, vol. 1. Morgan Kaufmann, 2010.

[45] C. Wilhelmsson, P. Tunestål, and B. Johansson, "FPGA based engine feedback control algorithms," in *FISITA 2006 World Automotive Congress*, JSAE, 2006.

[46] E. Monmasson, L. Idkhajine, M. N. Cirstea, I. Bahri, A. Tisan, and M. W. Naouar, "FPGAs in industrial control applications," *IEEE Transactions on Industrial informatics*, vol. 7, no. 2, pp. 224–243, 2011.

[47] K. Ebrahimi, *Model Based Control of Combustion Timing and Load in HCCI Engines*. Dissertation, University of Alberta, 2016.

[48] K. Ebrahimi, A. Schramm, and C. R. Koch, "Feedforward/feedback control of HCCI combustion timing," in *2014 American Control Conference*, pp. 831–836, June 2014.

[49] K. Ebrahimi and C. Koch, "Model predictive control for combustion timing and load control in HCCI engines," in *SAE Technical Paper 2015-01-0822*, SAE International, 04 2015.

[50] S. M. Erlien, A. F. Jungkunz, and J. C. Gerdes, "Multi-cylinder HCCI control with cam phaser variable valve actuation using model predictive control," in *Proceedings of the 2012 ASME Dynamic Systems and Control Conference*, vol. 2, pp. 823–832, 2013.

[51] N. Ravi, H.-H. Liao, A. F. Jungkunz, A. Widd, and J. C. Gerdes, "Model predictive control of HCCI using variable valve actuation and fuel injection," *Control Engineering Practice*, vol. 20, no. 4, pp. 421–430, 2012.

[52] D. Ritter, J. Andert, D. Abel, and T. Albin, "Model-based control of gasoline-controlled auto-ignition," *International Journal of Engine Research*, vol. 19, no. 2, pp. 189–201, 2018.

[53] S. Choi, M. Ki, and K. Min, "Development of an on-line model to predict the in-cylinder residual gas fraction by using the measured intake/exhaust and cylinder pressures," *International Journal of Automotive Technology*, vol. 11, no. 6, pp. 773–781, 2010.

[54] J. Andert, M. Wick, B. Lehrheuer, C. Sohn, T. Albin, and S. Pischinger, "Autoregressive modeling of cycle-to-cycle correlations in homogeneous charge compression ignition combustion," *International Journal of Engine Research*, vol. 19, no. 7, pp. 790–802, 2018.

[55] U. Koehler and M. Bargende, "A model for a fast prediction of the in-cylinder residual gas mass," *SAE Technical Papers 2004-01-3053*, 2004.

[56] S. Trajkovic, A. Milosavljevic, P. Tunestål, and B. Johansson, "FPGA controlled pneumatic variable valve actuation," in *SAE 2006 World Congress & Exhibition*, SAE International, apr 2006.

[57] J. Pfluger, J. Andert, H. Ross, and F. Mertens, "Rapid control prototyping for cylinder pressure indication," *MTZ Worldwide*, vol. 73, no. 11, pp. 38–42, 2012.

[58] M. Wick, B. Lehrheuer, T. Albin, J. Andert, and S. Pischinger, "Decoupling of consecutive gasoline controlled auto-ignition combustion cycles by field programmable gate array based real-time cylinder pressure analysis," *International Journal of Engine Research*, vol. 19, no. 2, pp. 153–167, 2018.

[59] J. K. Arora and M. Shahbakhti, "Real-time closed-loop control of a light-duty

RCCI engine during transient operations," in *SAE Technical Paper*, SAE International, 03 2017.

[60] A. Boretti, "Water injection in directly injected turbocharged spark ignition engines," *Applied Thermal Engineering*, vol. 52, no. 1, pp. 62–68, 2013.

[61] F. Bedford, C. Rutland, P. Dittrich, A. Raab, and F. Wirbeleit, "Effects of direct water injection on di diesel engine combustion," tech. rep., SAE Technical Paper, 2000.

[62] N. Kaneko, H. Ando, H. Ogawa, and N. Miyamoto, "Expansion of the operating range with in-cylinder water injection in a premixed charge compression ignition engine," tech. rep., SAE Technical Paper, 2002.

[63] S. Kohketsu, K. Mori, K. Sakai, and H. Nakagawa, "Reduction of exhaust emission with new water injection system in a diesel engine," *SAE transactions*, pp. 74–81, 1996.

[64] W. S. Binion, "Cylinder water injection engine," Aug. 17 1999. US Patent 5,937,799.

[65] S. Nakayama, K. Mori, T. Hakozaki, and A. Suzuki, "Water injection amount control system for fuel and water injection engine," Sept. 5 2000. US Patent 6,112,705.

[66] Y. Tosa and Y. Nagae, "Water injection diesel engine," Dec. 29 1992. US Patent 5,174,247.

[67] B. L. Slagle, "Water injection system for diesel engine," Jan. 19 1982. US Patent 4,311,118.

[68] F. Pischinger and P. Kreuter, "Arrangement for electromagnetically operated actuators," May 7 1985. US Patent 4,515,343.

[69] F. Pischinger *et al.*, "Electromechanical variable valve timing," *Automotive Engineering International*, 1999.

[70] FEV Motorentechnik, *Operation of the Electromechanical Variable Valve Train - EMVT Closed Loop Engine*, July 2002.

[71] D. Gordon, C. Wouters, M. Wick, F. Xia, B. Lehrheuer, J. Andert, C. R. Koch, and S. Pischinger, "Development and experimental validation of a real-time capable FPGA based gas-exchange model for negative valve overlap," *International Journal of Engine Research*, 2018.

[72] G. P. Merker, C. Schwarz, and R. Teichmann, "Grundlagen Verbrennungsmotoren," *Simulation der Gemischbildung, Verbrennung, Schadstoffbildung und Aufladung*, vol. 4, 2009.

[73] R. Pischinger, M. Klell, and T. Sams, *Thermodynamik der Verbrennungskraftmaschine*. Springer-Verlag, 2009.

[74] G. Woschni, "A universally applicable equation for the instantaneous heat transfer coefficient in the internal combustion engine," tech. rep., SAE Technical paper 670931, 1967.

[75] G. Hohenberg, *Experimentelle Erfassung der Wandwärme von Kolbenmotoren*. PhD thesis, Universität Graz, 1980.

[76] P. D. I. G. Wachtmeister, *Motordynamik und Brennverfahren*. 2012.

[77] E. Justi, "Die Dissoziation," in *Spezifische Wärme Enthalpie, Entropie und Dissoziation technischer Gase*, pp. 123–141, Springer, 1938.

[78] F. Zacharias, *Analytische Darstellung der thermodynamischen Eigenschaften von Verbrennungsgasen*. 1966.

[79] P. Kirchen, M. Shahbakhti, and C. R. Koch, "A skeletal kinetic mechanism for PRF combustion in HCCI engines," *Combustion science and technology*, vol. 179, no. 6, pp. 1059–1083, 2007.

[80] R. Van Basshuysen and F. Schäfer, *Handbuch Verbrennungsmotor: Grundlagen, Komponenten, Systeme, Perspektiven*. Springer-Verlag, 2014.

[81] D. Seebach, *Untersuchung der kontrollierten Selbstzündung an einem direkteinspritzenden Ottomotor und Modellierung des transienten Verhaltens*. Dissertation, RWTH Aachen University, Aachen, 22.10.2010.

[82] B. Morcinkowski, *Simulative Analyse von zyklischen Schwankungen der kontrollierten ottomotorischen Selbstzündung*. Dissertation, RWTH Aachen University, Aachen, 2015.

[83] A. Brassat, *Betriebsstrategien der kontrollierten Selbstzündung am aufgeladenen direkteinspritzenden Ottomotor*. Dissertation, RWTH Aachen University, Aachen, 07.10.2013.

[84] A. Kronich, *Methodik zur Entwicklung eines vollvariablen Ventiltriebes*. PhD thesis, Technische Universität Kaiserslautern, 2006.

[85] D. Jung and D. Assanis, "Multi-zone DI diesel spray combustion model for cycle simulation studies of engine performance and emissions," *SAE Technical Papers*, 2001.

[86] B. Lehrheuer, B. Morcinkowski, S. Pischinger, and M. Nijs, "Low temperature gasoline combustion – potential, challenges, process modeling and control," in *Active Flow and Combustion Control 2014* (R. King, ed.), vol. 127 of *Notes on numerical fluid mechanics and multidisciplinary design*, pp. 163–179, Cham: Springer, 2015.

[87] D. Gordon, C. Wouters, M. Wick, B. Lehrheuer, J. Andert, C. R. Koch, and S. Pischinger, "Development and experimental validation of an FPGA based in-cycle direct water injection control strategy for HCCI combustion stability," in *Symposium for Combustion Control*, pp. 195–206, 2018.

[88] D. Gordon, C. Wouters, M. Wick, B. Lehrheuer, J. Andert, C. R. Koch, and S. Pischinger, "Development and experimental validation of an fpga based in-cycle direct water injection control strategy for hcci combustion stability," *International Journal of Engine Research*, 2018. Submitted October 31, 2018 (Submission ID: IJER-18-0240).

[89] M. Wick, D. Gordon, J. Bedei, C. Wouters, E. Nuss, B. Lehrheuer, J. Andert, and C. R. Koch, "In-cycle control for stabilization of HCCI combustion using direct water injection," *Applied Energy*, 2018. Submitted on October 1, 2018 (APEN-D-18-09617).

[90] T. Tsurushima, E. Kunishima, Y. Asaumi, Y. Aoyagi, and Y. Enomoto, "The effect of knock on heat loss in homogeneous charge compression ignition engines," in *SAE 2002 World Congress & Exhibition*, SAE International, mar 2002.